

# Solar Neutrinos and Reconstruction of the SNO+ Experiment

Jie Hu

A Dissertation

Presented to the Faculty  
of University of Alberta  
in Candidacy for the Degree  
of Doctor of Philosophy

Recommended for Acceptance  
by the Department of  
Department of Physics

January, 2020

© Copyright 2020 by Jie Hu.

All rights reserved.

# **Abstract**

## **0.1 Abstract**

A neutrino is one of the elementary particles we currently know and is included in the Standard Model (SM). However, some properties of neutrinos can not be described by the SM, which shows clues of the new physics beyond the Standard Model.

SNO+ experiment is planned to explore one of the unknown properties of neutrinos: whether the neutrinos are Majorana particles or Dirac particles.

# Acknowledgements

# Contents

<b>Abstract</b>	<b>iii</b>
0.1 Abstract . . . . .	iii
<b>Acknowledgements</b>	<b>iv</b>
<b>Contents</b>	<b>v</b>
<b>List of Figures</b>	<b>ix</b>
<b>List of Tables</b>	<b>xvi</b>
<b>1 Introduction</b>	<b>1</b>
<b>2 Neutrino physics</b>	<b>5</b>
2.1 Discovery of Neutrino . . . . .	5
2.2 Basic Properties . . . . .	6
2.3 Neutrino Flavor Transformation . . . . .	6
2.3.1 Vacuum Oscillation . . . . .	7
2.3.2 Matter Effect . . . . .	11
2.3.3 Status of the Neutrino Flavor Transformation Experiments . . . . .	13
2.3.4 Atmospheric Neutrino . . . . .	13
2.4 Solar Neutrino . . . . .	14
2.5 Neutrino Mass . . . . .	15

2.6	Measure the Absolute Neutrino Mass . . . . .	25
2.6.1	Cosmological Approach . . . . .	25
2.6.2	Direct Kinetic Measurements from Beta Decay . . . . .	26
2.6.3	Double Beta Decay . . . . .	28
2.6.4	Status of Double Beta Decay Experiments . . . . .	30
<b>3</b>	<b>The SNO+ Experiment</b>	<b>36</b>
3.1	Overview . . . . .	36
3.2	SNO+ Physics Phases . . . . .	37
3.3	Detection Medium . . . . .	41
3.3.1	Cherenkov Radiation . . . . .	41
3.3.2	Scintillation from Organic Scintillator . . . . .	42
3.3.3	Liquid Scintillator for SNO+ . . . . .	45
3.4	Optics . . . . .	48
3.5	Electronics . . . . .	49
3.6	Calibration . . . . .	53
3.6.1	The $^{16}\text{N}$ Calibration Source . . . . .	54
3.6.2	The Americium Beryllium (AmBe) Calibration Source . . . . .	55
3.6.3	The Laserball . . . . .	56
3.7	Detector Backgrounds . . . . .	56
3.7.1	Physics Backgrounds . . . . .	56
3.7.2	Instrumental Backgrounds . . . . .	56
3.8	Monte Carlo Simulation and the RAT Software . . . . .	56
<b>4</b>	<b>Event Reconstruction</b>	<b>59</b>
4.1	An Overview of the Reconstruction Algorithms in SNO+ . . . . .	59
4.2	Multi-path Reconstruction Algorithm for SNO+ . . . . .	60
4.3	Multi-path Position and Direction Reconstructions for the Water Phase . . . . .	62
4.3.1	Vertex Reconstruction . . . . .	62

4.3.2	Direction Reconstruction . . . . .	64
4.3.3	Effective Group Velocity . . . . .	65
4.3.4	Fitter Pull and Drive Correction . . . . .	67
4.3.5	Multi-path Fitter Structure . . . . .	71
4.4	Vertex and Direction Reconstruction for the Water-based Wavelength-shifter	73
4.5	Vertex Reconstruction for the Partial-fill and Scintillator Phases . . . . .	77
4.6	PMT Selectors for the Reconstruction . . . . .	85
4.7	Energy Reconstruction . . . . .	87
4.7.1	Energy Reconstruction in Partial-fill Phase . . . . .	87
4.8	Other Reconstruction Algorithms . . . . .	88
4.8.1	Hough Transformation for Direction Reconstruction . . . . .	88
4.9	Conclusion . . . . .	89
<b>5</b>	<b>SNO+ Water Phase Analysis</b>	<b>90</b>
5.1	High Level Cuts: Classifiers . . . . .	90
5.2	$^{16}\text{N}$ Calibration Scans in the Water Phase . . . . .	91
5.2.1	Angular Resolution . . . . .	96
5.3	Energy . . . . .	102
5.4	Extracting $\gamma$ -rays from Neutron Capture . . . . .	108
5.5	Solar $\nu_e$ Analysis and Background Separation in Water Phase . . . . .	108
<b>6</b>	<b>Towards the SNO+ Future Phases</b>	<b>112</b>
6.1	Partial-fill Phase Analysis . . . . .	112
6.1.1	High Level Cuts: Sky-shine Classifier . . . . .	112
6.1.2	Different PPO Concentrations during the Filling . . . . .	116
6.1.3	Bi-Po Analysis . . . . .	119
6.1.4	$^{16}\text{N}$ Calibration Calibration in the Partial-fill Phase . . . . .	119
6.1.5	Extracting the Cherenkov Signals in Partial-fill Phase . . . . .	120
6.2	Towards the Te-loaded Phase . . . . .	122

6.2.1	Muon Induced Backgrounds in the Te-loaded Phase . . . . .	122
6.2.2	Relative Light Yield Measurements of the Te-loaded Liquid Scintillators	127
6.2.3	Measurement Setup and Data Acquisition . . . . .	129
<b>7</b>	<b>Conclusions</b>	<b>138</b>
<b>A</b>	<b>Details for the MultiPath Fitter</b>	<b>139</b>
A.1	Create a Random Vertex . . . . .	139
A.2	Levenberg-Marquardt (MRQ) Method for Minimization[1] . . . . .	139
A.3	Detailed Light Path Calculations in the MultiPath Scint-water Fitter . . . . .	142
<b>B</b>	<b>Information for <math>^{16}\text{N}</math> Scan Runs</b>	<b>145</b>
B.1	Information for $^{16}\text{N}$ Scan Runs . . . . .	145
<b>References</b>		<b>149</b>

# List of Figures

2.1	Feynman diagrams (at tree level) for different channels of the elastic scattering interaction. (a) and (b): charged current for s and t channels, respectively; (c): neutral current. . . . .	7
2.2	All reactions in the three PP chains: PP-I, PP-II, PP-III. The reactions producing neutrinos are labeled in the solid frames. Modified from [2]. . . . .	16
2.3	All reactions in the CNO bicycle. The reactions producing neutrinos are labeled in the solid frames. Modified from [2]. . . . .	16
2.4	Solar neutrino energy spectrum ( $E_\nu$ vs. flux) for the solar model BS05(OP). Figure is from [3]. . . . .	17
2.5	Tree-level Feynman diagrams for the Seesaw Mechanisms, modified from [4]: type-I (left) and type-II (right). The type-III scheme shares the same diagram to the type-I, but with the $\nu_R$ replaced by $T^0$ . . . . .	24
2.6	$\sqrt{\langle m_{\nu_e}^2 \rangle}$ as a function of the lightest mass ( $m_1$ for NH or $m_3$ for IH). . . . .	27
2.7	Feynman diagrams for $2\nu\beta\beta$ (a) and $0\nu\beta\beta$ (b). . . . .	28
2.8	Effective Majorana mass as a function of the lightest mass eigenvalue. Solid lines are for NH cases and dashed lines are for IH. Different colors stand for taking different values of $(\alpha_1, \alpha_2)$ . . . . .	31
2.9	Energy spectrum of the $^{130}\text{Te}$ $2\nu\beta\beta$ decay and the hypothetical $0\nu\beta\beta$ decay. The SNO+ simulation package (RAT) was used to produce the plot. . . . .	31
2.10	Natural abundance vs. Q-values for different $2\nu\beta\beta$ isotopes[5]. . . . .	34

3.1	The SNO+ detector labelled with main structures, figure modified from [6]. . . . .	38
3.2	A Jablonski diagram for the organic scintillator, modified from [7, 8]. . . . .	43
3.3	Structural formulae of LAB (left) and PPO (right). . . . .	46
3.4	Absorption length of SNO+ optical components. ;the internal (solid blue line) and external water (dashed blue line) absorption curves are based on the measurements of the laserball scans in July 2018 during the SNO+ water phase. The horizontal lines are due to absence of the measurements and they are conservative assumptions. . . . .	47
3.5	$^{16}\text{N}$ main decay scheme, modified from [9]. . . . .	54
3.6	$^{16}\text{N}$ calibration source geometry. Left: a detailed diagram of $^{16}\text{N}$ source geometry, modified from [10, 11]; middle: source geometry implemented in RAT, modified from [12]; right: a picture of the $^{16}\text{N}$ source, taken from [13].	55
4.1	Diagrams of position (left) and direction (right) reconstruction in SNO+ water phase. . . . .	62
4.2	PMT response time as the timing pdf for vertex reconstruction. . . . .	63
4.3	PMT angular distribution as the angular response pdf for direction reconstruction. . . . .	64
4.4	Refractive index vs wavelength. These values are based on the measurements from laserball calibration scans in the SNO+ water phase[14]. . . . .	65
4.5	A cartoon shows effects of tuning the effective group velocity. In this case, the effective group velocity is faster than expected, the fitted position is dragged back along the direction to increase the time of flight. . . . .	66
4.6	$^{16}\text{N}$ central run. . . . .	67
4.7	A cartoon shows fitter pull effect, modified from Fig. C.2 in [15] and Fig. 2,3,4 in [16]. . . . .	68
4.8	A diagram illustrates the drive correction. . . . .	69
4.9	Drive correction parameter $p_0$ , $p_1$ vs energy. . . . .	70

4.10 Radial biases of simulated electron events before and after the drive correction, as a function of energy. . . . .	70
4.11 Position distributions of triggered PMTs (in zenith and azimuth angles) for 5 MeV electrons travelling along $+x$ direction in the pure water (left) and the water plus 0.1 ppm PPO (right). . . . .	74
4.12 The energies of simulated electrons as a function of mean nhits. The values in the 0.1 ppm PPO (solid line with inverted triangle) are compared with the water (dashed line with star). . . . .	75
4.13 The timing pdf for the wbWLS. . . . .	75
4.14 Fit position projected on x axis. The WLS fitter reconstructed $x$ positions of the 5 MeV electron events in the wbWLS (red) are compared to the ones in the water (blue). . . . .	76
4.15 Light path calculation for the MP Partial Fitter. The light path intersects with the neck cylinder surface, the AV sphere as well as the water-scintillator interface. The total length of the path in the scintillator region (scintillator path, $sp$ ), $d_{sp}$ is evaluated by intersection calculations. . . . .	78
4.16 Line-sphere intersections. (a): the light ray intersects the sphere with 2 points; (b): the light ray intersects the sphere with 1 point; (c) and (d): the light ray never passes through the sphere. . . . .	79
4.17 The timing pdfs used by the MP Partial Fitter. Blue: the timing pdf used by the MP Water Fitter; red: the scintillator timing pdf. . . . .	81
4.18 Distributions of fit position bias projected on x axis ( $x_{fit} - x_{MC}$ ). . . . .	82
4.19 Fit results: $\rho_{fit} = \sqrt{x_{fit}^2 + y_{fit}^2}$ vs. $z_{fit}$ . . . . .	82
4.20 Timing profiles for liquid scintillators in different SNO+ phases. . . . .	84
4.21 Group the PMTs by dividing the PMT sphere with latitudes and longitudes. . . . .	86
4.22 Hough transformation for catching the ring structure of Cherenkov signals and fitting the direction. . . . .	88
5.1 A cartoon shows the $^{16}\text{N}$ source. . . . .	92

5.2	Spatial distributions of $^{16}\text{N}$ first $\gamma$ -rays interaction position projected on x axis, obtained from RAT simulations. The double-peak structure is due to the wall of the stainless steel container of the $^{16}\text{N}$ source. . . . .	92
5.3	Position resolutions, compared the data (red) and MC (black). The resolution fit functions are overlaid with histograms. . . . .	94
5.4	Fit position biases ( $ \vec{X}_{fit} - \vec{X}_{MC} $ ) vs FOM (scaled LogL) for the $^{16}\text{N}$ central run-107055. . . . .	94
5.5	Fit direction resolutions ( $ \vec{X}_{fit} - \vec{X}_{MC} $ ) vs FOM (scaled LogL) for the $^{16}\text{N}$ central run-107055. . . . .	95
5.6	Likelihood surface of an $^{16}\text{N}$ event projected on X-Y, Y-Z, X-Z planes. A clear global maxima is reached for the fitted vertex. . . . .	97
5.7	Likelihood surface of an $^{16}\text{N}$ event projected on x, y, z, t axes. . . . .	98
5.8	Derivatives of logLikelihood of an $^{16}\text{N}$ event projected on x, y, z, t axes. The analytical derivatives (blue) are overlaid with numerical derivatives (red). They are well-matched. . . . .	99
5.9	X scan. . . . .	99
5.10	Y scan. . . . .	100
5.11	Z scan. The data (black boxes) is compared with MC (red circles). . . . .	100
5.12	Angular distributions extracted from the data (red solid line) and the MC (black dashed line); both are reconstructed by the MPW fitter. These distributions are fitted with the angular resolution functions ranging from 0.3 to 1. . . . .	102
5.13	$\beta_{14}$ systematic for various $^{16}\text{N}$ scans. . . . .	103
5.14	$\Delta\beta_M$ (top) and $\Delta\beta_S$ (bottom) systematic for various $^{16}\text{N}$ scans along three axes. . . . .	103
5.15	NHit spectrum for the $^{16}\text{N}$ central run-107055. Dashed lines for the MC and solid lines for data; red for the MPW fitter results and black for the Rat results.	104
5.16	Energy spectrum, extracted from $10^5$ MC simulation events. . . . .	104

5.17	Reconstructed $^{16}\text{N}$ energy spectrum for run-106925 ( $\vec{X}_{source} = (-186.0, 254.0, -4999.899)$ mm) . . . . .	105
5.18	Reconstructed energy spectrum for the $^{16}\text{N}$ central run-107055. Dashed lines for the MC and +solid lines for data; red for the MPW fitter results and black for the Rat results. . . . .	105
5.19	Distributions of $\beta_{14}$ for the $^{16}\text{N}$ central run-107055. Dashed lines for the MC and solid lines for data; red for the MPW fitter processed results and black for the Rat results. . . . .	106
5.20	Comparisons of the $\beta_{14}$ for the data and the MC. Both of the distributions are the MPW processed results and are fitted with Gaussian distributions in a region of $[-0.5, 1.5]$ . The data shows a smaller mean value (0.4157) than the MC (0.4388). . . . .	106
5.21	Electron energy vs number of Cherenkov photons. . . . .	107
5.22	Energy vs $\beta_{14}$ for the data and MC. Both the Rat and the MPW results are shown. . . . .	107
5.23	$^{16}\text{N}$ external run-111230 with a nominal position at [-5861,-2524,4001] mm; MPW results. . . . .	108
5.24	Fit results for the candidate events, projected onto PMT sinusoidal maps. Black circles stand for the hit PMTs used by the fitter; crosses stand for the hit PMTs removed by the selectors; blue full star stands for the event direction fitted by the waterFitter; red open star stands for the direction fitted by the MPW; full double diamond stands for the solar direction*-1; blue full square stands for the event position fitted by the waterFitter; open square stands for the position fitted by the MPW. . . . .	109
5.25	Comparison between solar $\nu_e$ and external solar $\nu_e$ ; MPW results. . . . .	111
6.1	An illustration for the Sky-shine classifier, modified from [17]. . . . .	113
6.2	MC (left) and fitted positions (right) of $^{208}\text{Tl}$ simulations. . . . .	114
6.3	MC positions vs. skyShine values for simulated $^{208}\text{Tl}$ events. . . . .	115

6.4	MC positions after Sky-shine cuts ( $skyShine < 1.7$ and $skyShine < 1.5$ ) for simulated $^{208}\text{Tl}$ events. It shows that most of the events with small $skyShine$ values are located in the neck region while very few events in the FV region can be mis-tagged. . . . .	115
6.5	Fit biases vs. skyShine values for simulated $^{208}\text{Tl}$ events. . . . .	116
6.6	Fit biases vs. skyShine values for simulated $^{208}\text{Tl}$ events. . . . .	117
6.7	Radial resolutions with different skyShine cuts. . . . .	117
6.8	Timing spectrum for different PPO concentrations based on the Oxford bench-top measurements. . . . .	119
6.9	A flow chart for Bi-Po tagging. . . . .	121
6.10	Distributions of $\cos \theta_{PMT}$ after the prompt time cut for various $e^-$ energies simulations. . . . .	122
6.11	PMT hit patterns after the prompt time cut and NHit cut. . . . .	123
6.12	$^{16}\text{N}$ source calibration in external water during the partial-fill phase. . . . .	124
6.13	Simulated main track of 7.1 MeV $\gamma$ for one event from $^{16}\text{N}$ source in the external water during the partial-fill phase. . . . .	124
6.14	Energy spectrum of cosmic muon induced $^{11}\text{C}$ backgrounds in SNO+ Te-loaded phase for one year duration. Left: Monte Carlo energy distributions. Right: Reconstructed energy distributions. . . . .	126
6.15	Energy spectrum of cosmic muon induced $^{10}\text{C}$ backgrounds in SNO+ Te-loaded phase for one year duration. Left: Monte Carlo energy distributions. Right: Reconstructed energy distributions. . . . .	126
6.16	Energy spectrum of cosmic muon induced $^6\text{He}$ backgrounds in SNO+ Te-loaded phase for one year duration. Left: Monte Carlo energy distributions. Right: Reconstructed energy distributions. . . . .	126
6.17	Energy spectrum of cosmic muon induced $^{11}\text{C}$ backgrounds in SNO+ solar phase for one year duration. Left: Monte Carlo energy distributions. Right: Reconstructed energy distributions. . . . .	128

6.18	Energy spectrum of cosmic muon induced $^{10}\text{C}$ backgrounds in SNO+ solar phase for one year duration. Left: Monte Carlo energy distributions. Right: Reconstructed energy distributions. . . . .	128
6.19	Energy spectrum of cosmic muon induced $^6\text{He}$ backgrounds in SNO+ solar phase for one year duration. Left: Monte Carlo energy distributions. Right: Reconstructed energy distributions. . . . .	128
6.20	Test sample (left) and setup (right). Left: The samples were filled into scintillation vials. The dimensions are shown in the picture. Right: two PMTs are aligned to face to the scintillation vial from each side. . . . .	130
6.21	A diagram shows the light yield measurement setup. See the text for details.	131
6.22	A typical waveform triggered by scintillation photons from $^{137}\text{Cs}$ $\gamma$ -rays interaction with LAB-PPO sample. . . . .	134
6.23	Measured LAB-PPO energy spectrum with and without coincidence cut on the ADC channel 0. A threshold for counting is set by comparing the two spectrum. . . . .	134
6.24	2D energy spectrum of the counting measurements of LAB-PPO (a), TeSOP (b), and TeDDA (c) samples, projected the 2D plots into one channel (d). The single photo-electron (p.e.) peak is mainly caused by backgrounds while the multiple p.e. peak is from scintillation photons. . . . .	135
A.1	Layouts for the scintillator light paths inside the AV sphere. . . . .	143
A.2	Layouts of the scintillator light paths inside the neck cylinder. . . . .	144

# List of Tables

2.1	Oscillation neutrino experiments. . . . .	10
2.2	. . . . .	16
2.3	The limits of $T_{1/2}^{0\nu}$ and $m_{\beta\beta}$ at 90% C.L. . . . .	34
2.4	The limits of $T_{1/2}^{0\nu}$ and $m_{\beta\beta}$ at 90% C.L. . . . .	35
4.1	A comparison of quantitative estimates for the angular resolution between the SNO heavy water, SNO+ wbWLS and the SNO+ pure water cases. . . . .	77
4.2	Reconstructed position biases and resolutions for simulated events in partial fill. . . . .	81
4.3	. . . . .	83
5.1	Position resolution parameters for the MP Water Fitter. . . . .	96
5.2	Candidate events in the open dataset. Compared the fitted results of the candidate events with different fitters. . . . .	96
5.3	Candidate events in the open dataset. Compared the fitted results of the candidate events with different fitters. . . . .	96
5.4	Candidate events in the open dataset. Compared the fitted results of the candidate events with different fitters. . . . .	101
5.5	Candidate events in the open dataset. Compared the fitted results of the candidate events with different fitters. . . . .	110
5.6	Candidate events in the open dataset, searched by the MPW fitter. . . . .	110
6.1	time constants and amplitudes measured by Oxford group [18]. . . . .	118

6.2	Relative light yield (RLY) measured by [18]. . . . .	118
6.3	Tuned effective group velocities for different PPO concentrations. . . . .	118
6.4	Fit speeds and biases for various PPO concentrations. . . . .	119
6.5	Fit speeds and biases for various PPO concentrations. . . . .	120
6.6	Cosmic muon induced isotopes production rates $R_i [kt^{-1}yr^1]$ . . . . .	125
6.7	Decay information of the isotopes. . . . .	125
6.8	Production rates for $^{11}\text{C}$ , $^{10}\text{C}$ and $^6\text{He}$ backgrounds in SNO+ Te-loaded Phase.	127
6.9	Event rates of cosmic muon induced $^{11}\text{C}$ , $^{10}\text{C}$ and $^6\text{He}$ backgrounds in SNO+ Te-loaded Phase (unit: $kt^{-1} \cdot yr^{-1}$ ). Different fiducial volume (FV) cuts and ROI region cuts are applied. The “MC” Column presents the values obtained from the Monte Carlo and the “Recon.” column presents the values obtained from the reconstructed energies. . . . .	127
6.10	Event rates of cosmic muon induced $^{11}\text{C}$ , $^{10}\text{C}$ and $^6\text{He}$ backgrounds in SNO+ solar phase (unit: $kt^{-1} \cdot yr^{-1}$ ). FV Cuts ROI [MeV] $^{11}\text{C}$ events $^{10}\text{C}$ events $^6\text{He}$ events . . . . .	129
6.11	Number of photons calculated by Charge weighted photon number method. . . . .	137
B.1	. . . . .	146
B.2	. . . . .	147
B.3	. . . . .	148
B.4	. . . . .	148

# Chapter 1

## Introduction

A neutrino is a spin-1/2 fermion with neutral electric charge and interacts only via weak interaction and gravity, which is described by the Standard Model. The Standard Model is a theory describing all of the elementary particles to our current knowledge and their interactions. In the Standard Model, neutrinos are created from weak interactions in one of three leptonic flavors: electron neutrinos ( $\nu_e$ ), muon neutrinos ( $\nu_\mu$ ) and tauon neutrinos ( $\nu_\tau$ ), accompanied by electrons ( $e$ ), muons ( $\mu$ ) and tauons ( $\tau$ ) respectively. The weak interactions are described by fermions exchanging  $W^\pm$  and  $Z^0$  bosons as weak force carriers.

The Standard Model has successfully explained and predicted phenomena in particle physics since the latter half of the 20th century, including the discovery of Higgs bosons in 2012, which is a crucial piece predicted by the Standard Model. However, there are opening issues in the Standard Model, such as the requirement of input parameters which can not be determined by the theory itself. Moreover, there are a few questions and problems the Standard Model can not answer or solve. The mystery properties and behaviors of neutrinos contribute a few of those questions: What are the masses of neutrinos? How do neutrinos obtain their masses? Why their masses are so small compared to the other elementary particles? Are neutrinos their own antiparticles? And so on. To answer these questions about neutrinos will open a door to the new physics theories beyond the Standard Model.

Since neutrinos weakly interact with other particles and fields, they can penetrate

through massive matter or travel a long way through the space without being interrupted. Neutrinos produced in the core of the Sun, in Supernovae, or in the galactic core of the Milky Way can carry original information of these astrophysics objects and easily reach the detectors on the Earth. This enables neutrinos as a probe to study the status of astrophysics objects.

These interesting facts put the researches of neutrinos under the spotlight. Among state-of-the-art neutrino experiments, SNO+ aims to search for an extremely rare process called neutrinoless double beta decay ( $0\nu\beta\beta$ ). This search will explore the unknown nature of neutrinos: whether they are Majorana or Dirac particles, unravel the masses of neutrinos, and test the new physics theories as well.

The SNO+ experiment will go through three major stages, which are mainly determined by the working medium inside the SNO+ detector. First, the detector was filled with water and worked as a water Cherenkov detector. This period of data collection for physics research is called the “water phase”. During this stage, certain fluxes of neutrinos from the Sun has been measured. Rare decay process modes, the invisible nucleon decay, which is predicted by the Grand Unified Theory (GUT) have also been searched. During this phase, calibration sources have been deployed for measuring the detector properties. Up until this thesis writing, the water phase stage has been completed and the water is gradually replaced by the liquid scintillator. Once the detector is fully filled with the liquid scintillator, the experiment will walk into the “scintillator phase”.

After that, the Tellurium will be loaded into the liquid scintillator

This transition stage is called “partial-fill phase”.

Then I further developed and completed it for multiple SNO+ physics phases, especially for the “partial-fill phase”, which refers to the transition statuses when the SNO+ detector is partially filled with the liquid scintillator.

In this thesis, a framework of event position and time reconstruction algorithms is developed for multiple SNO+ physics phases. This event reconstruction framework was first developed by the author’s supervisor, Dr. Aksel Hallin, to reconstruct and investigate

the data taken at an early stage of SNO+ when the detector was partially filled with water at the end of 2014 (called “partial water fill stage”)[19]. It was further developed by the researchers from the University of Alberta: Dr. Kalpana Singh and Dr. David Auty, for investigating the wavelength shifter and water events[20, 21, 22, 23]. Dr. Jeff Tseng from the University of Oxford restructured the framework into more flexible and efficient C++ codes and implemented it into the SNO+ software[24]. I first involved in testing and optimizing this reconstruction framework on the simulations and data.

The data taken from these statuses are used for background estimations. The framework is also extended for the scintillator phase and the Tellurium-loading phase as well. The principles and optimizations are described in Chapter 4.

In Chapter 2,  
neutrino physics  
solar neutrinos neutrino flavor transformation, neutrino mass, neutrinoless double beta decay.

In Chapter 3, the SNO+ experiment, how the SNO+ detector works and reads the physics data. The properties of the liquid scintillator

In Chapter 5, this reconstruction framework is applied for the water phase physics analyses. I analyzed the calibration source data during the water phase. By comparing the simulations and data, I obtained the reconstruction resolutions and uncertainties. Then it is applied for the solar neutrino and backgrounds analysis. The SNO+ official reconstruction results were compared with the and it shows that the better direction resolutions, which would be useful for the solar neutrino analyses.

Moving towards the Tellurium-loading phase for searching  $0\nu\beta\beta$  process, the SNO+ collaboration started filling the liquid scintillator into the detector from July 2019.  
for background analysis.

These transition statuses are called ”partial-fill”.

In Chapter 6,  
based on Monte Carlo simulations.

higher light yield

A light yield measurement for Tellurium-loaded liquid scintillator

The last chapter summarizes the works of this thesis.

# Chapter 2

## Neutrino physics

In this chapter, I will give an overview of the neutrino and its properties. After an introduction of the history studies, two important properties: neutrino flavor transformations and neutrino mass are discussed.

### 2.1 Discovery of Neutrino

The existence of neutrinos was first put forward by Wolfgang Pauli in the 1930s to solve the contradictions observed in beta decay experiments. It was shown definitively by James Chadwick in 1914 that the electrons emitted in beta decay did not have a discrete set of energies but instead had a continuous spectrum[25]. This means that the energy, momentum and angular momentum (spin) were not conserved between the nucleus and electron. To solve this problem, Wolfgang Pauli introduced a charge-neutral, spin-1/2 and nearly massless new particle. The sum of the energies of the new particle, the nucleus and electron is constant, which solved the problem.

In 1934, Bethe and Peierls suggested direct neutrino detection via a neutrino-induced interaction, called the inverse beta decay (IBD):  $\bar{\nu}_e + p \rightarrow e^+ + n$ . Their calculation showed that the IBD cross section was of the order of  $10^{-44} \text{ cm}^2$ . Such a small cross section indicates that the neutrino is difficult to detect[26].

In 1956, Fred Reines and Clyde Cowan made the first discovery of the neutrino (specif-

ically, it was electron antineutrinos  $\bar{\nu}_e$ ) by using a nuclear reactor as an intense neutrino source with neutrino fluxes on the order of  $10^{12} - 10^{13} \bar{\nu}_e$  s/second/cm<sup>2</sup>. The active volume of their detector was two tanks filled with water in which cadmium chloride ( $\text{CdCl}_2$ ) was dissolved. The water tanks were surrounded by liquid scintillator layers coupled with photomultiplier tubes (PMT) to detect emitted photons. The incoming antineutrinos interacted with the water via IBD. The produced positrons quickly annihilated with  $e^-$  and gave  $\gamma$  signals while the produced neutrons went through the neutron capture process:  $n + {}^{108}\text{Cd} \rightarrow {}^{109}\text{Cd}^* \rightarrow {}^{109}\text{Cd} + \gamma$  and gave delayed  $\gamma$  signals. A coincidence of these two characteristic signals provided a distinctive signature for the neutrino reaction. They measured the cross-section as  $6.3 \times 10^{-44}$  cm<sup>2</sup>, which was consistent with Bethe's calculation[27].

## 2.2 Basic Properties

Neutrinos have three flavors.

the muon neutrino was discovered by Lederman, Schwartz and Steinberger in 1962.

In 1962, Lederman, Schwartz and Steinberger demonstrated that more than one type of neutrino exists by detecting the interactions of the muon neutrino [8]. The tau neutrino was only proposed after the discovery of the lepton and was not observed until 2000 by the DONUT collaboration

Helicity

the measurement of neutrino helicity[28]

In the next two sections, I will show the two properties which are under the spotlight: neutrinos can change their flavors and they have masses.

## 2.3 Neutrino Flavor Transformation

Neutrino flavor transformation is a quantum mechanical interference phenomenon[29]. It was first discovered in 1998, based on the analysis of atmospheric neutrino fluxes measured by the Super-Kamiokande (SuperK) experiment to solve the “atmospheric neutrino

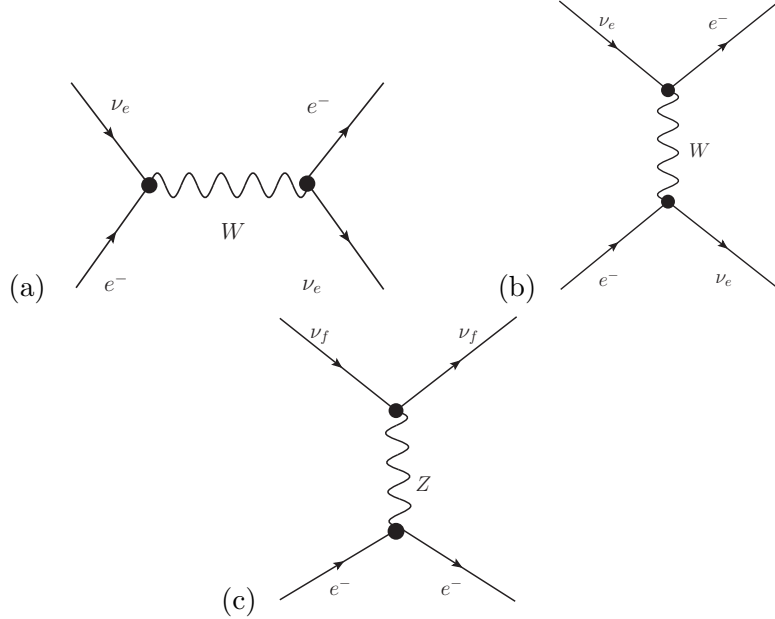


Figure 2.1: Feynman diagrams (at tree level) for different channels of the elastic scattering interaction. (a) and (b): charged current for  $s$  and  $t$  channels, respectively; (c): neutral current.

anomaly” mentioned in the last section[30]. It is the first direct evidence showing that neutrinos have finite masses and the Standard Model (SM) is incomplete.

Based on current knowledge, neutrinos only interact via the weak force and gravity. A neutrino  $\nu_\alpha$  is generated with a definite flavor from weak interaction and is related to a charged lepton with a given flavor: the electron ( $e$ ), the muon ( $\mu$ ) or the tauon ( $\tau$ ) and thus  $\alpha = e, \mu, \tau$ .

### 2.3.1 Vacuum Oscillation

For neutrino flavor oscillation experiments, neutrinos are detected in certain flavor eigenstates via weak interaction. A neutrino flavor state vector can be taken as a linear superposition of the mass eigenstates. For three-flavor neutrino mixing, we have[31]:

$$|\nu_f\rangle = \sum_{i=1}^3 U_{fi}^* |\nu_i\rangle, \quad (2.1)$$

where  $f = e, \mu, \tau$  and  $k = 1, 2, 3$ . The unitary PMNS matrix,  $U_{PMNS}$ , can be parameterized as<sup>1</sup> :

$$U_{PMNS} = \begin{pmatrix} 1 & 0 & 0 \\ 0 & c_{23} & s_{23} \\ 0 & -s_{23} & c_{23} \end{pmatrix} \begin{pmatrix} c_{13} & 0 & e^{-i\delta_{CP}} s_{13} \\ 0 & 1 & 0 \\ e^{-i\delta_{CP}} s_{13} & 0 & c_{13} \end{pmatrix} \begin{pmatrix} c_{12} & s_{12} & 0 \\ -s_{12} & c_{12} & 0 \\ 0 & 0 & 1 \end{pmatrix}, \quad (2.2)$$

where  $c_{ij} \equiv \cos \theta_{ij}$  and  $s_{ij} \equiv \sin \theta_{ij}$  ( $i, j = 1, 2, 3$ ) are shorthands. In the PMNS matrix, there are four parameters: the three mixing angles  $\theta_{12}$ ,  $\theta_{13}$ ,  $\theta_{23}$  and the charge-parity (CP) violation parameter of lepton sector,  $\delta_{CP}$ . The unknown value of  $\delta_{CP}$  is related to leptogenesis, the hypothetical physical process that produced an asymmetry between leptons and anti-leptons in the very early universe[32].

Now discuss the vacuum flavor oscillation: in the lab frame, assume a neutrino is generated at time  $t_0 = 0$  from a source with a certain flavor state  $|\nu_\alpha\rangle$ . It then propagates in vacuum with a speed close to the speed of light (ultra-relativistic) for a distance  $L$  and is finally detected at time  $t$  in a detector. The flavor eigenstate evolves in space-time is  $|\nu_\alpha\rangle = \sum_i U_{\alpha i}^* |\nu_i, p_i\rangle$ , where  $p_i$  is the 4-momentum of  $\nu_i$ . The momentum is assumed to be along the direction from the source to the detector and only in one dimension. Via the Schrödinger equation, the amplitude for the flavor eigenstate  $|\nu_\beta\rangle$  in the detector at  $(L, t)$  is (use the natural units:  $\hbar = c = 1$ ) [33]:

$$\mathcal{A}(\nu_\alpha \rightarrow \nu_\beta; L, E) = \sum_i U_{\alpha i}^* e^{-iE_i t + ip_i L} \langle \nu_\beta | \nu_i, p_i \rangle = \sum_i U_{\alpha i}^* U_{\beta i} e^{-iE_i t + ip_i L}, \quad (2.3)$$

Then the probability of  $\nu_\alpha$  at time  $t_0 = 0$  transforms into a  $\nu_\beta$  at time  $t$  is:

$$\begin{aligned} P(\nu_\alpha \rightarrow \nu_\beta; L, E) &= |\langle \mathcal{A}(\nu_\alpha \rightarrow \nu_\beta; L, E) | \mathcal{A}(\nu_\alpha \rightarrow \nu_\beta; L, E) \rangle|^2 = \\ &= (U_{\alpha 1}^* U_{\beta 1} e^{-iE_1 t + ip_1 L} + U_{\alpha 2}^* U_{\beta 2} e^{-iE_2 t + ip_2 L} + \dots) (U_{\alpha 1} U_{\beta 1}^* e^{+iE_1 t - ip_1 L} + U_{\alpha 2} U_{\beta 2}^* e^{+iE_2 t - ip_2 L} + \dots) = \\ &= \sum_i |U_{\alpha i}|^2 |U_{\beta i}|^2 + \sum_{i>j} (U_{\alpha i}^* U_{\beta i} U_{\alpha j} U_{\beta j}^*) \exp\{-i(E_i - E_j)t + i(p_i - p_j)L\} + (i \leftrightarrow j), \end{aligned} \quad (2.4)$$

where  $(i \leftrightarrow j)$  stands for the second term exchanging the  $i, j$  indices.

---

<sup>1</sup>Here we ignore the Majorana CP violation phases, which are cancelled out when tackling with the flavor transformation probability. We will come to this part in section. 2.5

For the second term in 2.4: in the ultra-relativistic case,  $p_i \simeq p_j \equiv p \simeq E \gg m$ , where  $E$  is the average energy. Then  $E_i = \sqrt{p_i^2 + m_i^2} \simeq p + \frac{m_i^2}{2E}$  and thus  $E_i - E_j \simeq \frac{m_i^2 - m_j^2}{2E} \equiv \frac{\Delta m_{ij}^2}{2E}$  [31, 33]. Here  $\Delta m_{ij}^2$  is a set of parameters called mass square difference, popping out in the flavor transition probability. Along with  $L \simeq ct = t$  ( $c \equiv 1$ ), we have  $\exp\{-i(E_i - E_j)t + i(p_i - p_j)L\} \simeq \exp\{-i\frac{\Delta m_{ij}^2}{2E}t\}$ . In addition,  $U_{\alpha i}^* U_{\beta i} U_{\alpha j} U_{\beta j}^* = |U_{\alpha i}^* U_{\beta i} U_{\alpha j} U_{\beta j}^*| \exp\{i\phi_{\alpha\beta;ij}\}$ , where  $\phi_{\alpha\beta;ij} = \text{Arg}(U_{\alpha i}^* U_{\beta i} U_{\alpha j} U_{\beta j}^*)$  and  $\phi_{\alpha\beta;ij} = -\phi_{\alpha\beta;ji}$ . Then combine the second term and the  $(i \leftrightarrow j)$  term, 2.4 can be written as[33]:

$$P_{\nu_\alpha \rightarrow \nu_\beta}(L, E) = \sum_i |U_{\alpha i}|^2 |U_{\beta i}|^2 + 2 \sum_{i>j} |U_{\alpha i}^* U_{\beta i} U_{\alpha j} U_{\beta j}^*| \cos\left(\frac{\Delta m_{ij}^2}{2E} L - \phi_{\alpha\beta;ij}\right). \quad (2.5)$$

Further expand the second term in 2.5:

$$\begin{aligned} & |U_{\alpha i}^* U_{\beta i} U_{\alpha j} U_{\beta j}^*| \left\{ \cos(\phi_{\alpha\beta;ij}) \cos\left(\frac{\Delta m_{ij}^2}{2E} L\right) + \sin(\phi_{\alpha\beta;ij}) \sin\left(\frac{\Delta m_{ij}^2}{2E} L\right) \right\} = \\ & \Re(U_{\alpha i}^* U_{\beta i} U_{\alpha j} U_{\beta j}^*)(1 - 2 \sin^2 \frac{\Delta m_{ij}^2 L}{4E}) + \Im(U_{\alpha i}^* U_{\beta i} U_{\alpha j} U_{\beta j}^*) \sin \frac{\Delta m_{ij}^2 L}{2E}, \end{aligned} \quad (2.6)$$

since the matrix  $U$  is unitary and when  $t = 0$ ,

$$P_{\nu_\alpha \rightarrow \nu_\beta} = \delta_{\alpha\beta} = \sum_i |U_{\alpha i}|^2 |U_{\beta i}|^2 + 2 \sum_{i>j} \Re(U_{\alpha i}^* U_{\beta i} U_{\alpha j} U_{\beta j}^*), \quad (2.7)$$

finally it comes out the commonly used vacuum oscillation equation[31, 33]:

$$P_{\nu_\alpha \rightarrow \nu_\beta}(L, E) = \delta_{\alpha\beta} - 4 \sum_{i>j} \Re(U_{\beta i} U_{\alpha i}^* U_{\alpha j} U_{\beta j}^*) \sin^2 \frac{\Delta m_{ij}^2 L}{4E} + 2 \sum_{i>j} \Im(U_{\beta i} U_{\alpha i}^* U_{\alpha j} U_{\beta j}^*) \sin \frac{\Delta m_{ij}^2 L}{2E}. \quad (2.8)$$

Choose a set of units commonly used by experiments and with dimensional transformation, we have[31]:

$$X_{ij} \equiv \frac{\Delta m_{ij}^2 L}{4E} = \frac{1.267 \Delta m_{ij}^2 [eV^2] L [m]}{E_\nu [MeV]}. \quad (2.9)$$

Maximum oscillation occurs when  $X_{ij} \sim \pi$ , which gives an effective length  $L^{osc}(\Delta m_{ij}, E_\nu) = 4\pi E / |\Delta m_{ij}^2|$ .

Currently, the four parameters in PMNS matrix as well as the parameters of the  $\Delta m_{ij}$  have been measured by neutrino oscillation experiments. These experiments can be classified by the neutrino sources they use. They are the solar, the reactor, the atmospheric, the

Table 2.1: Oscillation neutrino experiments.

type	source	$E_\nu$	example
solar	the Sun	MeV scale	SNO
reactor	reactor	MeV scale	DayaBay
atmospheric	cosmic-ray	GeV scale	SuperK
accelerator	$\nu$ beam from accelerator	GeV scale	T2K
astronomical	astronomical objects	GeV-EeV scale	IceCube

accelerator and the astronomical and cosmological neutrino experiments. Table 2.1 lists the energy scale of the neutrino source as well as the example experiments.

For the  $\Delta m_{21}^2$  and  $\theta_{12}$ , the combined analysis of the measurements from the reactor experiment KamLAND and SNO gave  $\Delta m_{21}^2 = 7.59_{-0.21}^{+0.21} \times 10^{-5} eV^2$  and  $\tan^2 \theta_{21} = 0.47_{-0.05}^{+0.06}$ [34].

The accelerator neutrino experiments as well as the atmospheric neutrino experiments have measured  $\Delta m_{32}^2$  and  $\theta_{23}$ . The most recent results from SuperK show that in NH,  $\sin^2 \theta_{23} = 0.588_{-0.064}^{+0.031}$  and  $\Delta m_{32}^2 = 2.5_{-0.20}^{+0.13} \times 10^{-3} eV^2$ [35].

In 2012, the reactor neutrino experiment Daya Bay reported the discovery of non-zero  $\theta_{13}$  with a significance of  $5.2\sigma$ . In 2016, Daya Bay reported that  $\sin^2 2\theta_{13} = 0.0841 \pm 0.0027(stat.) \pm 0.0019(syst.)$ . This high-precision result makes  $\sin^2 2\theta_{13}$  the best measured mixing angle[36, 37].

In addition, there are two squared-mass differences,  $\Delta m_{21}^2 = m_2^2 - m_1^2$  and  $\Delta m_{32}^2 = |m_3^2 - m_2^2|$ . The sign of  $\Delta m_{32}^2$  is unknown and it indicates a mass hierarchy problem of whether neutrino mass is normal hierarchy (NH,  $m_3 > m_2 > m_1$ ) or inverted hierarchy (IH,  $m_3 < m_1 < m_2$ )[31].

$$L/L^{osc}(\Delta m_{31}, E_\nu) \sim 1 \text{ and } L/L^{osc}(\Delta m_{21}, E_\nu) \ll 1$$

$$P_{\nu_\alpha \rightarrow \nu_\beta}(L, E) \simeq \delta_{\alpha\beta} - 4|U_{\alpha 3}|^3(\delta_{\alpha\beta} - |U_{\beta 3}|^2) \sin^2 \frac{\Delta m_{31}^2 L}{4E} = P_{\bar{\nu}_\alpha \rightarrow \bar{\nu}_\beta}(L, E) \quad (2.10)$$

In the case of antineutrino flavor oscillation, we have:  $|\bar{\nu}_\alpha\rangle = \sum_i U_{\alpha i} |\bar{\nu}_i, p_i\rangle$ , via the same calculation, a similar oscillation probability equation can be found but with the last

term in 2.8 being negative[33]:

$$P_{\bar{\nu}_\alpha \rightarrow \bar{\nu}_\beta}(L, E) = \delta_{\alpha\beta} - 4 \sum_{i>j} \Re[U_{\beta i} U_{\alpha i}^* U_{\alpha j} U_{\beta j}^*] \sin^2 \frac{\Delta m_{ij}^2 L}{4E} - 2 \sum_{i>j} \Im(U_{\beta i} U_{\alpha i}^* U_{\alpha j} U_{\beta j}^*) \sin \frac{\Delta m_{ij}^2 L}{2E}. \quad (2.11)$$

This provides a measure of CP violation[33]:

$$\mathcal{A}_{CP} = P_{\nu_\alpha \rightarrow \nu_\beta}(L, E) - P_{\bar{\nu}_\alpha \rightarrow \bar{\nu}_\beta}(L, E) = 4 \sum_{i>j} \Im(U_{\beta i} U_{\alpha i}^* U_{\alpha j} U_{\beta j}^*) \sin \frac{\Delta m_{ij}^2 L}{2E}. \quad (2.12)$$

[38]

$\delta_{CP}$  is examined by the experiments which measure the difference between neutrino and antineutrino oscillation probabilities  $P(\bar{\nu}_\alpha \rightarrow \bar{\nu}_\beta)$  and  $P(\nu_\alpha \rightarrow \nu_\beta)$ [39]. In 2017, the Tokai-to-Kamioka (T2K) experiment in Japan rejected the hypothesis that neutrinos and antineutrinos oscillate with the same probability at 95% confidence ( $2\sigma$ ) level. This indicates a hint of CP symmetry broken by neutrinos[40]. In 2019, T2K claimed confidence intervals for  $\delta_{CP}$  with three standard deviations ( $3\sigma$ ): [-3.41,-0.03] for NH and [-2.54,-0.32] for IH. This result indicates that the CP violation exists in leptons[41].

### 2.3.2 Matter Effect

The matter effect is caused by neutrinos interacting with ambient electrons and nucleons in matter such as the Sun or the Earth.  $\nu_e$  interacts with electrons via both charged weak current (exchanging  $W$  boson) and neutral weak current ( $Z$  boson) while  $\nu_\mu$  and  $\nu_\tau$  interact only by the neutral current. The  $\nu_e$  energy has an addition term,  $V_{CC} = \sqrt{2}G_F n_e$ , where  $n_e$  is the number density of the electrons in matter and  $G_F$  is the Fermi coupling constant for the weak interaction. This affects the oscillation probabilities for neutrinos propagating in matter compared to vacuum, which is called the Mikheyev-Smirnov-Wolfenstein (MSW) mechanism[42, 43].

In vacuum two-flavor mixing, the Schrödinger equation can be written (in natural units)[39]:

$$i \frac{d}{dt} \begin{pmatrix} \nu_e \\ \nu_\mu \end{pmatrix} = H_0^f \begin{pmatrix} \nu_e \\ \nu_\mu \end{pmatrix}, \quad (2.13)$$

where

$$H_0^f = \frac{1}{2E} \begin{pmatrix} m_1^2 \cos^2 \theta + m_2^2 \sin^2 \theta & (m_2^2 - m_1^2) \sin \theta \cos \theta \\ (m_2^2 - m_1^2) \sin \theta \cos \theta & m_1^2 \sin 2\theta + m_2^2 \cos^2 \theta \end{pmatrix} = \frac{\Delta m_{21}^2}{4E} \begin{pmatrix} -\cos 2\theta & \sin 2\theta \\ \sin 2\theta & \cos 2\theta \end{pmatrix} + \frac{(m_1^2 + m_2^2)}{4E} \begin{pmatrix} 1 & 0 \\ 0 & 1 \end{pmatrix}, \quad (2.14)$$

and  $\Delta m_{21}^2 = (m_2^2 - m_1^2)$ .

To simplify the calculation, we can drop the second unitary term of  $H_0^f$  that is irrelevant to the neutrino flavor transformation. Including the matter effect, we obtain:

$$H_m = \begin{pmatrix} -\frac{\Delta m_{21}^2}{4E} \cos 2\theta + \sqrt{2}G_F n_e & \frac{\Delta m_{21}^2}{4E} \sin 2\theta \\ \frac{\Delta m_{21}^2}{4E} \sin 2\theta & \frac{\Delta m_{21}^2}{4E} \cos 2\theta \end{pmatrix} \quad (2.15)$$

We define a mixing angle in matter,  $\theta_m$  as:

$$\tan 2\theta_m = \frac{\Delta m^2 \sin 2\theta}{\Delta m^2 \cos 2\theta - 2\sqrt{2}EG_F n_e}, \quad (2.16)$$

and define an effective squared-mass difference in matter  $\Delta m_m^2$  as:

$$\Delta m_m^2 = \sqrt{(\Delta m^2 \cos 2\theta - 2\sqrt{2}EG_F n_e)^2 + (\Delta m^2 \sin 2\theta)^2}. \quad (2.17)$$

In analogy with mixing in vacuum, we can write the mixing equation relating the energy eigenstates in matter  $(\nu_{1m}, \nu_{2m})$  to the flavor eigenstates with a diagonalized Hamiltonian:

$$\begin{pmatrix} \nu_e \\ \nu_\mu \end{pmatrix} = \begin{pmatrix} \cos \theta_m & \sin \theta_m \\ -\sin \theta_m & \cos \theta_m \end{pmatrix} \begin{pmatrix} \nu_{1m} \\ \nu_{2m} \end{pmatrix}. \quad (2.18)$$

The probability of flavor transformation in matter is:

$$P_{\nu_e \rightarrow \nu_\mu} = \sin^2(2\theta_m) \sin^2 \left( \frac{\Delta m_m^2 L}{4E} \right). \quad (2.19)$$

The denominator in equation (2.16) implies a resonance condition:

$$V(n_e) = \sqrt{2}G_F n_e = \frac{\Delta m^2 \cos 2\theta}{2E}. \quad (2.20)$$

From this condition, for a given  $E$ , there is a resonance density  $n_e^{reson}$  while for a given  $n_e$ , there is a resonance energy  $E^{reson}$ . When the resonance condition is satisfied,  $\theta_m = \frac{\pi}{4}$

and two flavor neutrinos are maximally mixed, even if the vacuum mixing angle  $\theta$  is small. This is called matter enhanced neutrino oscillation[42, 44].

The oscillation probability in matter can be written in a concise and exact form as [45]:

$$P(\nu_e \rightarrow \nu_\mu) = A \cos \delta + B \sin \delta + C$$

will also provide the information for the CP- and T-violation by investigating the quantities of:

$$A_{CP} = \frac{P(\nu_\alpha \rightarrow \nu_\beta) - P(\bar{\nu}_\alpha \rightarrow \bar{\nu}_\beta)}{P(\nu_\alpha \rightarrow \nu_\beta) + P(\bar{\nu}_\alpha \rightarrow \bar{\nu}_\beta)}$$

$$A_T = \frac{P(\nu_\alpha \rightarrow \nu_\beta) - P(\bar{\nu}_\beta \rightarrow \bar{\nu}_\alpha)}{P(\nu_\alpha \rightarrow \nu_\beta) + P(\bar{\nu}_\beta \rightarrow \bar{\nu}_\alpha)}$$

### 2.3.3 Status of the Neutrino Flavor Transformation Experiments

In 1964, John Bahcall and Raymond Davis proposed the first experiment to detect solar neutrinos[46, 47]. Raymond Davis designed an experiment that used a  $380 \text{ m}^3$  tank filled with Perchloroethylene ( $\text{C}_2\text{Cl}_4$ ), a dry-cleaning fluid rich in chlorine. Solar neutrinos were expected to change  $^{37}\text{Cl}$  to  $^{37}\text{Ar}$  via the endothermic reaction  $\nu_e + ^{37}\text{Cl} \rightarrow ^{37}\text{Ar} + e^-$  and the produced  $^{37}\text{Ar}$  were extracted and counted. The neutrino energy threshold ( $E_{thresh}$ ) of the experiment was 0.814 MeV, which allowed a measurement mostly of the  $^8\text{B}$  neutrino flux but also including some lower energy neutrinos[47]. Their first results, announced in 1968, showed that only about one-third of the predicted radioactive argon atoms were measured. This raised a problem of missing solar neutrinos.

### 2.3.4 Atmospheric Neutrino

Cosmic rays from outer space continuously interact with nuclei in the atmosphere and produce secondary particles. Atmospheric neutrinos come from decay products of the hadrons in the secondaries. The dominant processes of atmospheric  $\nu_e$  and  $\nu_\mu$  production is  $\pi^+ \rightarrow \mu^+ + \nu_\mu$  followed by  $\mu^+ \rightarrow e^+ + \bar{\nu}_\mu + \nu_e$ . In the 1980s, the Kamiokande experiment in Japan measured atmospheric neutrinos by utilizing a 3-kiloton water-Cherenkov detector.

The incoming neutrinos,  $\nu_e$  ( $\nu_\mu$ ) interacted with the water via charged current interactions and electrons (muons) were produced. The electrically charged leptons traversed the water at a speed higher than the speed of light in water and thus emit Cherenkov light, which was recorded by the detector as ring patterns (called Cherenkov rings). The produced electrons caused electro-magnetic showers during their propagation in the water while the produced muons propagated almost in straight lines without producing electro-magnetic showers. Then the  $\nu_\mu$  (the  $\mu$ -like events) were separated from the  $\nu_e$  (the  $e$ -like events) by the fact that the  $\mu$ -like events created sharper Cherenkov rings than the  $e$ -like events. Kamiokande measured the ratio of fluxes  $\Phi(\nu_\mu + \bar{\nu}_\mu)/\Phi(\nu_e + \bar{\nu}_e)$ . The fluxes of atmospheric neutrinos are well understood and the ratio  $\nu_\mu/\nu_e$  is expected to be  $\sim 2$  at low energies  $\leq 1$  GeV. In 1988, they found a deficit of measured  $\mu$ -like events compared to the prediction. This was later confirmed by IMB in 1992[48] and Soudan-2 in 1997[49] and called “atmospheric neutrino anomaly”[50].

Since neutrinos’ extremely low interaction cross-sections, neutrinos produced in the Sun can reach the detectors on the Earth without being interrupted. This enables the solar neutrino to be a probe to the stellar physics.

KamLAND

Daya Bay

The Jiangmen Underground Neutrino Observatory (JUNO) is a reactor neutrino experiment located at Kaiping, Jiangmen in Southern China. a large liquid scintillator detector large active mass of 20 kton

the energy resolution (3% at 1 MeV) [51]

## 2.4 Solar Neutrino

In the 1930s, Hans Bethe et al. explained the origin of the Sun’s energy as a series of nuclear reactions[52].

Based on the available physics and experimental data, the Standard Solar Model (SSM) is a modern accepted theory for the evolution of the Sun. The energy in the Sun is mainly

produced by two sets of reactions: the proton-proton (pp) chain, which contributes to  $\sim 98.6\%$  of the energy release and the Carbon-Nitrogen-Oxygen (CNO) cycle, which contributes  $\sim 1.4\%$ . Fig. 2.2 and Fig. 2.3 show all the reactions in the two sets respectively. Via these two main sets of nuclear reactions, hydrogen is eventually fused into helium, and the net nuclear transformation is:  $4p + 2e^- \rightarrow {}^4\text{He} + 2\nu_e + Q$ , where the released energy  $Q = 26.73 \text{ MeV}$  is mostly in the form of kinetic energy of the photons, with a small fraction carried by neutrinos[4, 38]. The average energy of solar  $\nu_e$  is calculated by summing over the  $E_{\nu_e}$  from the  $i^{th}$  reaction chain with a flux of  $\Phi_{\nu_e}^i$  and divided by  $\Phi_{\nu_e}^{tot}$

reaction chains. For

as[38]:

$$\langle E_{\nu_e} \rangle = \sum_i E_i \frac{\Phi_{\nu_e}^i}{\Phi_{\nu_e}^{tot}} \approx 0.265 \text{ MeV}, \quad (2.21)$$

(the average neutrino energy  $\langle E_{2\nu_e} \rangle \sim 0.59 \text{ MeV}$ ).

Besides, about 2 MeV of  $Q$  is from annihilation of positrons with electrons in the solar plasma[4, 38]. For every released energy, there are about 2  $\nu_e$  generated. The solar  $\nu_e$  flux at the Earth surface can be estimated via the measured solar radiation energy on the Earth surface:

$$\Phi_{\nu_e} \simeq \frac{2\mathcal{L}_\odot}{4\pi D_\odot^2} \frac{1}{Q - 2\langle E_{\nu_e} \rangle} = 6.35 \times 10^{10} \nu_e/\text{cm}^2/\text{s}, \quad (2.22)$$

where the solar constants  $G_{sc} = \mathcal{L}_\odot/(4\pi D_\odot^2) \simeq 0.136 \text{ W/cm}^2$  [53].

The electron neutrinos produced in the solar nuclear reactions are named solar neutrinos and they can be detected on the Earth. Due to the branching ratios and unterminated chains in the pp chain and CNO cycle, the solar neutrinos come from different reactions, as shown in Table 2.2. The specific solar neutrinos detected on the Earth are named after the specific fusion process[54]. They have different fluxes and energies, as shown in Fig. 2.4[3].

solar neutrinos are also a major backgrounds to the  $0\nu\beta\beta$  search

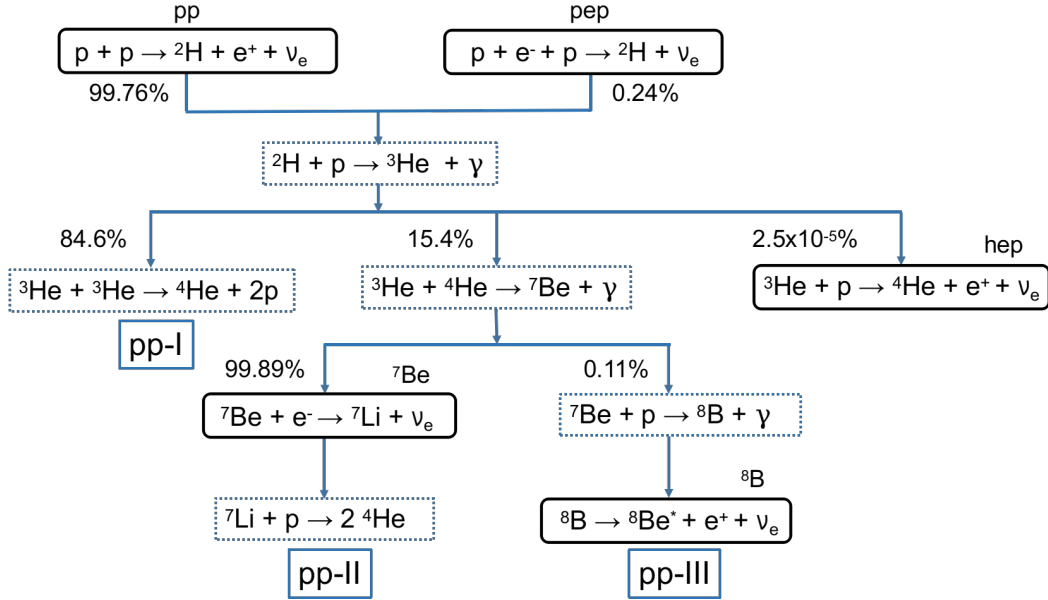


Figure 2.2: All reactions in the three PP chains: PP-I, PP-II, PP-III. The reactions producing neutrinos are labeled in the solid frames. Modified from [2].

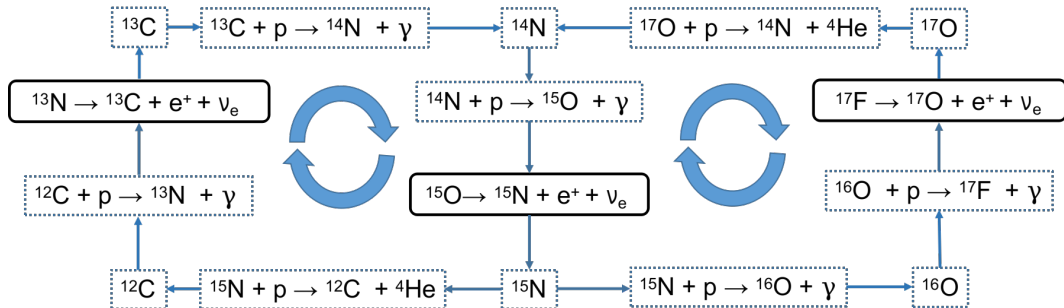


Figure 2.3: All reactions in the CNO bicycle. The reactions producing neutrinos are labeled in the solid frames. Modified from [2].

Table 2.2: Solar neutrinos from reactions in pp chain (a) and CNO cycle (b).

(a) pp chain		(b) CNO cycle	
solar $\nu_e$	reaction	solar $\nu_e$	reaction
pp	$p + p \rightarrow ^2\text{H} + e^+ + \nu_e$	CNO	$^{13}\text{N} \rightarrow ^{13}\text{C} + e^+ + \nu_e$
pep	$p + e^- + p \rightarrow ^2\text{H} + \nu_e$		$^{15}\text{O} \rightarrow ^{15}\text{N} + e^+ + \nu_e$
hep	$^3\text{He} + p \rightarrow ^4\text{He} + e^+ + \nu_e$		$^{17}\text{F} \rightarrow ^{17}\text{O} + e^+ + \nu_e$
$^7\text{Be}$	$^7\text{Be} + e^- \rightarrow ^7\text{Li} + \nu_e$		
$^8\text{B}$	$^8\text{B} \rightarrow ^8\text{Be}^* + e^+ + \nu_e$		

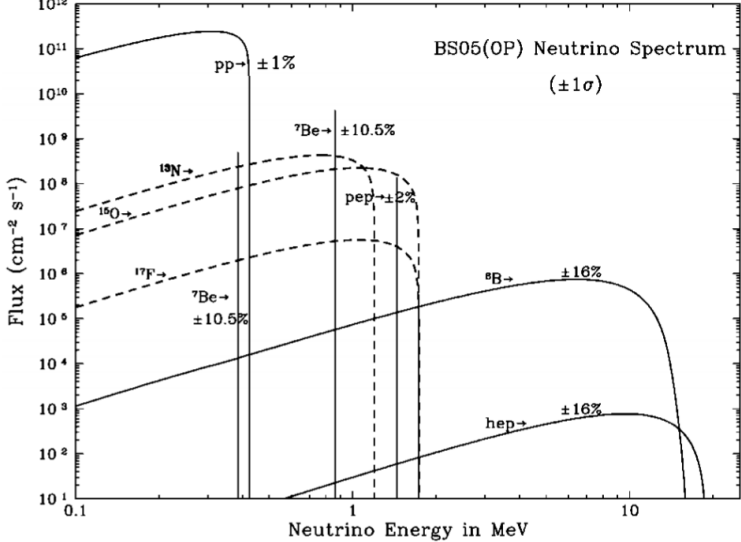


Figure 2.4: Solar neutrino energy spectrum ( $E_\nu$  vs. flux) for the solar model BS05(OP). Figure is from [3].

## 2.5 Neutrino Mass

A free neutrino with a mass  $m$  can be described by a four-component Dirac spinor field following the Dirac equation  $(i\gamma^\mu \partial_\mu - m)\psi = 0$ , where  $\partial_\mu \equiv \partial/\partial x^\mu$ , and  $\gamma^\mu$  ( $\mu = 0, 1, 2, 3$ ) is a set of  $4 \times 4$  matrices forming a Clifford algebra which satisfies the following relations[55, 56]:

$$\{\gamma^\mu, \gamma^\nu\} = 2\eta^{\mu\nu}, \quad (2.23)$$

where  $\eta^{\mu\nu} = \text{diag}(1, -1, -1, -1)$  is the Minkowski metric. From 2.23 we can deduce  $(\gamma^0)^2 = +1$ ,  $(\gamma^i)^2 = -1$  ( $i = 1, 2, 3$ ) and  $\gamma^0 \gamma^{\mu\dagger} \gamma^0 = \gamma^\mu$ . The product of the four gamma matrices is defined as  $\gamma_5 \equiv i\gamma^0 \gamma^1 \gamma^2 \gamma^3$ , which satisfies  $\{\gamma_5, \gamma^\mu\} = 0$  and  $(\gamma_5)^2 = 1$ . From  $\gamma_5$ , we can define the left-handed and right-handed chirality projector operators:  $P_L \equiv \frac{1}{2}(1 - \gamma_5)$  and  $P_R \equiv \frac{1}{2}(1 + \gamma_5)$ .

For fast moving particles like neutrinos, it's convenient to take  $\gamma$  matrices in chiral or Weyl representation (in which  $\gamma_5$  is diagonal) as[56]:

$$\gamma^0 = \begin{pmatrix} 0 & I \\ I & 0 \end{pmatrix}, \gamma^i = \begin{pmatrix} 0 & \sigma^i \\ -\sigma^i & 0 \end{pmatrix}, \gamma_5 = \begin{pmatrix} -I & 0 \\ 0 & I \end{pmatrix}, \quad (2.24)$$

where  $\sigma^i$  ( $i = 1, 2, 3$ ) are  $2 \times 2$  Pauli matrices and  $I$  is a  $2 \times 2$  identity matrix.

The Lagrangian density constructed from the Dirac equation is  $\mathcal{L}_D = \bar{\psi}(i\gamma^\mu\partial_\mu - m)\psi$ , where  $\bar{\psi} \equiv \psi^\dagger\gamma^0$  is an adjoint field. The Dirac spinor field  $\psi$  can be decomposed into left and right handed fields:  $\psi = \psi_L + \psi_R \equiv P_L\psi + P_R\psi$ . With  $\overline{\psi_L}\psi_L = \overline{\psi_R}\psi_R = 0$  the Dirac Lagrangian density which satisfies the Lorentz invariance and is hermitian can be written as[56]:

$$\mathcal{L}_D = (\overline{\psi_L}i\gamma^\mu\partial_\mu\psi_L + \overline{\psi_R}i\gamma^\mu\partial_\mu\psi_R) - m(\overline{\psi_R}\psi_L + \overline{\psi_L}\psi_R), \quad (2.25)$$

where the first two terms on the right hand side are kinetic energy terms with separated chiral components; the last two terms are the Dirac mass term  $\mathcal{L}_{mass}^D$  with coupled chiral components. For the massive Dirac fields, the left-handed component  $\psi_L$  is completely independent of the right-handed  $\psi_R$ .

A particle-antiparticle conjugation operator  $\hat{C}$  can associate the  $\psi_L$  with the  $\psi_R$ . It is defined as[55]:

$$\hat{C} : \psi \rightarrow \psi^c = \mathcal{C}\bar{\psi}^T = \mathcal{C}\gamma^0\psi^*, \quad (2.26)$$

where  $\mathcal{C}$  is the charge conjugation matrix and satisfies the following relations:

$$\mathcal{C}^{-1}\gamma^\mu\mathcal{C} = -(\gamma^\mu)^T, \quad \mathcal{C}^{-1}\gamma_5\mathcal{C} = (\gamma_5)^T, \quad \mathcal{C}^\dagger = \mathcal{C}^{-1} = -\mathcal{C}^* \quad (2.27)$$

In the Weyl representation,  $\mathcal{C} = i\gamma^2\gamma^0$ , then  $\mathcal{C}^2 = 1$ ,  $(\psi^c)^c = \psi$ ,  $(\psi_L)^c = P_R\psi^c = (\psi^c)_R$  and  $(\psi_R)^c = P_L\psi^c = (\psi^c)_L$ . Therefore the particle-antiparticle operation  $\hat{C}$  converts a left-handed antiparticle to a right-handed particle and vice versa (both the charge and chirality are changed).

In the SM, neutrinos are fermions without carrying electrical charges and they could be “truly neutral”, i.e., no charge-like quantum number can be used to distinguish a neutrino and an antineutrino, which is one of the reasons why neutrinos are special. As a comparison, a neutron is spin-1/2 and chargeless but it carries magnetic moments opposite to an antineutron[55].

From a viewpoint of mathematical aesthetics, Ettore Majorana found a representation which makes all the  $\gamma$  matrices be pure imaginary so that the Dirac equation gets rid

of complex coefficients[57]. Then the Dirac equation can be switched to the Majorana equation:  $i\gamma^\mu \partial_\mu \psi - m\psi^c = 0$ , which also satisfies the Lorentz invariance[56]. Since  $\psi$  and  $\psi^c$  have opposite charges, this equation should describe a neutral fermion[56].

Unlike the Dirac case, for a Majorana field  $\psi^M$ , the  $\psi_L^M$  and  $\psi_R^M$  are not independent. The right-handed component can be the charge conjugate of the left-handed component (or vice versa):  $\psi_R = (\psi_L)^c$ [55]. Therefore Majorana field can be written as:  $\psi^M = \psi_L^M + \psi_R^M = \psi_L^M + (\psi_L^M)^c = \psi_L^M + ((\psi^M)^c)_R$ , which immediately gives  $(\psi^M)^c = \psi^M$ . This equation is called the Majorana condition. The result implies that the particles associated with the Majorana fields, or the Majorana fermions, are their own antiparticles and “truly neutral”[55]. Also, the Majorana equation preserves the handedness[56]. Since the  $\psi_L^M$  and  $\psi_R^M$  are not independent and can be constructed by each other, the Majorana spinor  $\psi^M$  only has two degrees of freedom compared to the Dirac spinor which has four degrees of freedom. These facts indicate that the Majorana fermion theory is more economical than the Dirac one and it is also tailored for describing neutrinos. It is natural that neutrinos are of Majorana nature.

In the SM, the Majorana fermions are not included. Based on the experimental observations such as the discovery of the parity violation in the  $\beta$ -decay[58], the measurement of neutrino helicity[28] and so on, a maximal parity violating  $V - A$  theory was built and it only allows the left-handed flavor neutrino fields  $\nu_{\alpha L}$  ( $\alpha = e, \mu, \tau$ ) (or called “active” neutrinos) and right-handed flavor antineutrino fields  $\overline{\nu_{\alpha R}}$  involving in the weak interaction. In the theory, the neutrino fields  $\nu_\alpha$  and the charged lepton fields  $\ell_\alpha$  form the left-handed weak isospin doublets (isodoublets) and the right-handed isosinglets, which belong to the SU(2) group. The isodoublet  $\Psi_L = (\nu_{\alpha L}, \ell_{\alpha L})^T$  has weak isospin  $I = \frac{1}{2}$  and its third components  $I_3 = +\frac{1}{2}$  for  $\nu_\alpha$  and  $I_3 = -\frac{1}{2}$  for  $\ell_\alpha$ ; the isosinglet  $\Psi_R = (\ell_{\alpha R})$  has  $I = 0$  and  $I_3 = 0$ [33, 59].

According to the Gell-Mann-Nishijima formula  $Q = I_3 + \frac{1}{2}Y$ , where  $Q$  is the electric charge and  $Y$  is the hypercharge. For  $\Psi_L$ ,  $Y = -1$  and for  $\Psi_R$ ,  $Y = -2$ . The leptons acquire their masses by coupling to the Higgs fields. To realize this, the Higgs scalar fields also form an isodoublet  $\Phi = (\phi^+, \phi^0)^T$  with weak isospin  $I = \frac{1}{2}$ , where  $\phi^+$  is a positively

charged complex scalar field with  $I_3 = \frac{1}{2}$  and  $\phi^0$  is a neutrally charged complex scalar field with  $I_3 = -\frac{1}{2}$ . Such a coupling of the fermions to the scalar fields is a typical Yukawa coupling. The Lagrangian of the Yukawa coupling in the lepton sector is[60]:

$$-\mathcal{L}_{Yukawa}(\Phi, \Psi) = \sum_{\alpha, \beta=e, \mu, \tau} y_{\alpha\beta}^{lep'} \overline{\Psi'_{\alpha L}} \Phi \ell'_{\beta R} + h.c., \quad (2.28)$$

where  $y_{\alpha\beta}^{lep'}$  are complex Yukawa coupling matrices of charged leptons and the *h.c.* means hermitian conjugate. The terms are invariant under the  $SU(2)_L \times U(1)_Y$  group transformations required by the SM. The apostrophes indicate that these matrices are not diagonalized.

Since the lack of the isosinglet term  $\nu_R$ , neutrinos are considered as massless in the SM. The simplest extension to the SM to create neutrino masses is to introduce the  $SU(2)$  singlet states, or the right-handed neutrino fields  $\nu_R$ . This kind of isosinglet does not participate in the electroweak interactions and are thus called sterile neutrinos. By introducing the  $\nu_R$ , the SM is minimally extended and neutrinos can be massive[61].

Since the hypercharge of  $\overline{\Psi'_{\alpha L}}$  is  $Y = +1$  and  $\nu_R$  is  $Y = 0$ , the product  $\overline{\Psi'_{\alpha L}} \nu_{\beta R}$  is  $Y = 1$ . In order to form the  $SU(2)_L \times U(1)_Y$  invariant term, a conjugated Higgs doublet with hypercharge  $Y = -1$  is built as  $\tilde{\Phi} = i\sigma_2 \Phi^*$ , where  $\sigma_2$  is a Pauli matrix[61].

Then with right-handed singlets  $\nu_R$ , 2.28 turns to be[61, 60]:

$$-\mathcal{L}_{Yukawa} = \sum_{\alpha\beta} y_{\alpha\beta}^{lep'} \overline{\Psi'_{\alpha L}} \Phi \ell'_{\beta R} + \sum_{\alpha\beta} y_{\alpha\beta}^{\nu'} \overline{\Psi'_{\alpha L}} \tilde{\Phi} \nu'_{\beta R} + h.c.. \quad (2.29)$$

The Higgs field obtains a vacuum expectation value (VEV)  $v_0 = \langle \Phi \rangle$  via the electroweak symmetry breaking process. Taking the unitary gauge,  $\Phi = \frac{1}{\sqrt{2}} \begin{pmatrix} 0 \\ v_0 + h \end{pmatrix}$ , where  $h$  is a real scalar Higgs field.

To diagonalize the Lagrangian 2.29 to obtain definite masses of the fields, taking the unitary matrices:  $V_L^{lep}, V_R^{lep}, V_L^\nu$  and  $V_R^\nu$ , the Yukawa coupling matrices can be diagonalized by biunitary transformations:  $y^{lep} = V_L^{lep\dagger} y^{lep'} V_R^{lep}$ , with  $y_{\alpha\beta}^{lep} = y_\alpha^{lep} \delta_{\alpha\beta}$  for charged leptons;  $y^\nu = V_L^{lep\dagger} y^\nu V^{lep}$ , with  $y_{\alpha\beta}^\nu = y_\alpha^\nu \delta_{\alpha\beta}$  for neutrinos. The fields are transformed as:  $\ell_{L,R} = (V_{L,R}^{lep\dagger}) \ell'_{L,R}$  and  $\nu_{L,R} = (V_{L,R}^\nu) \nu'_{L,R}$ , where  $\ell'_{L,R} = (e', \mu', \tau')_{L,R}^T$  and  $\nu'_{L,R} = (\nu'_e, \nu'_\mu, \nu'_\tau)_{L,R}^T$

are in the flavor or generation space. The transformed fields  $\ell_{L,R}$  and  $\nu_{L,R}$  have definite masses. The product  $V_L^{lep\dagger} V_L^\nu \equiv U$  is actually the PMNS matrix which has the relation:  $\nu_{fL} = \sum_{i=1,2,3} U_{fi} \nu_{iL}$  [60, 62].

Thus the diagonalized Lagrangian 2.29 becomes[60]:

$$-\mathcal{L}_{Yukawa} = \left(\frac{v_0 + h}{\sqrt{2}}\right) \sum_{f=e,\mu,\tau} (y_f^{lep}) \overline{\ell_{fL}} \ell_{fR} + \sum_{i=1,2,3} (y_i^\nu) \overline{\nu_{iL}} \nu_{iR} + h.c., \quad (2.30)$$

In the Lagrangian 2.30, the terms proportional to the VEV of the Higgs doublet are mass terms while the terms proportional to the  $h$  describe the couplings between leptons and Higgs boson[61]. If neutrinos are Dirac particles, the mass term in 2.25 is  $-\mathcal{L}_\nu^D = m_D \overline{\nu_L} \nu_R + h.c.$ . In this case, the Dirac mass term becomes:

$$-\mathcal{L}_{mass}^D = \sum_{\alpha=e,\mu,\tau} \frac{v_0}{\sqrt{2}} (y_\alpha^{lep}) \overline{\ell_{\alpha L}} \ell_{\alpha R} + \sum_{i=1,2,3} \frac{v_0}{\sqrt{2}} (y_i^\nu) \overline{\nu_{iL}} \nu_{iR} + h.c., \quad (2.31)$$

So the charged lepton masses are given by:  $m_{\ell_\alpha} = \frac{y_\alpha^{lep} v_0}{\sqrt{2}}$  ( $\alpha = e, \mu, \tau$ ) and the neutrino masses are:  $m_i = \frac{y_i^\nu v_0}{\sqrt{2}}$  ( $i = 1, 2, 3$ ) [60].

In this Dirac mass case, the masses of charged leptons and neutrinos are both proportional to the Higgs VEV. However, the experimental measurements already show the masses of neutrinos are  $\mathcal{O}(eV)$  while charged leptons are  $\mathcal{O}(MeV)$ . The smallness of neutrino masses should be obtained by the tuning of the Yukawa couplings  $y_k^\nu$ , which does not have solid physics meanings or explanations.

If neutrinos are Majorana fermions, since  $\nu_L^c = (\nu^c)_R = (\nu)_R$ , we can take the neutrino field as  $\nu = \nu_L + \nu_L^c$  without introducing the extra  $\nu_R$ . For simplicity, only considering one flavor generation (such as  $\nu_e$ ), then the Majorana mass term is:

$$\mathcal{L}_{\nu mass}^{M,L} = -m_L \bar{\nu} \nu = -\frac{1}{2} m_L \overline{\nu_L^c} \nu_L + h.c., \quad (2.32)$$

where the 1/2 factor is to avoid double counting of  $\nu_L^c$  and  $\overline{\nu_L}$  since  $\nu_L^c = \mathcal{C} \overline{\nu_L}^T$  [61]. For this Majorana mass term, if considering the  $U(1)$  group transformations:  $\psi \rightarrow e^{i\alpha} \psi$  and  $\bar{\psi} \rightarrow \bar{\psi} e^{-i\alpha}$ , where  $\alpha$  is an arbitrary phase parameter. We find that in the Dirac case, the mass term in the form of  $\psi \bar{\psi}$  is invariant under  $U(1)$  transformations while in the

Majorana case it is not. This means that the Majorana fields break the conservation of all the  $U(1)$  charges, such as the electric charge and lepton number[55]. Since the law of electric charge conservation is solid in our universe, the particle with a Majorana mass must be electrically neutral while on the other hand, the lepton number for the Majorana fermion is not conserved, which is not described in the Standard Model. This allows for the neutrinoless double beta decay process and it will be discussed in the next section.

Also, since the terms  $\overline{\nu}_L^c \nu_L + h.c.$  are with the weak isospin  $I_3 = 1$  and then  $Y = -2$ , it requires a Higgs triplet with  $Y = 2$ , which is not included in the Standard Model[60]. Therefore, New Physics beyond the Standard Model is required for describing the Majorana mass term.

For a more general case: a hybrid mass term of Dirac and Majorana, if only considering one neutrino generation for simplicity, we can write the Dirac mass term in 2.25 as the same form of the Majorana mass term:  $\mathcal{L}_{\nu \text{ mass}}^D = -\frac{1}{2}m_D(\overline{\nu}_L \nu_R + \overline{\nu}_R^c \nu_L^c) + h.c..$  Likewise, introduce the  $\nu_R$  to the Majorana case and then we have a Majorana mass term with right-handed component:  $\mathcal{L}_{\nu \text{ mass}}^{M,R} = -m_R \overline{\nu}_R^c \nu_R + h.c..$  Therefore, the hybrid mass term combining the Majorana and Dirac fields is[55, 63]:

$$-\mathcal{L}_{\nu \text{ mass}}^{D+M} = -(\mathcal{L}_{\nu \text{ mass}}^D + \mathcal{L}_{\nu \text{ mass}}^{M,L} + \mathcal{L}_{\nu \text{ mass}}^{M,R}) = \frac{1}{2}N_L^T \mathcal{C}^\dagger \mathcal{M} N_L + h.c., \quad (2.33)$$

where  $N_L \equiv (\nu_L, (\nu_R)^c)^T = (\nu_L, \mathcal{C} \overline{\nu}_R^T)$ ; with  $m_L$  ( $m_R$ ) for the mass of the left-handed (right-handed) neutrino field, the mass matrix is written as:<sup>2</sup> :

$$\mathcal{M} = \begin{pmatrix} m_L^M & m^D \\ m^D & m_R^M \end{pmatrix}. \quad (2.34)$$

Using a unitary matrix  $U$  to diagonalize the  $\mathcal{M}$  so that  $U^T \mathcal{M} U = \mathcal{M}_d = \text{diag}(m_1, m_2)$ ;  $m_{1,2} \geq 0$  are the mass eigenvalues of the eigenstates  $\nu_{1,2}$  and

$$U = \mathcal{O}\rho = \begin{pmatrix} \cos \theta & \sin \theta \\ -\sin \theta & \cos \theta \end{pmatrix} \begin{pmatrix} \rho_1 & 0 \\ 0 & \rho_2 \end{pmatrix}, \quad (2.35)$$

---

<sup>2</sup>Here only considering one neutrino generation. In the general case  $\mathcal{M}$  is a  $(n_a + n_s) \times (n_a + n_s)$  matrix, for  $n_a$  active neutrinos and  $n_s$  sterile neutrinos[55, 63].

where  $\mathcal{O}$  is a real orthodox matrix and  $\rho$  is a phase matrix with  $(\rho_{1,2})^2 = \pm 1$  to guarantee that  $m_{1,2} \geq 0$ . From the transformation, the off-diagonal elements give a relation of  $\theta$ :  $\tan 2\theta = \frac{2m_D}{m_R^M - m_L^M}$ , which indicates a mixing of the normal active Dirac neutrino with a pair of the sterile Majorana neutrinos. For the left-handed neutrino mass eigenstates  $\nu_{1L}$  and  $\nu_{2L}$ , there is[55]:

$$N_L = \begin{pmatrix} \nu_L \\ (\nu_R)^c \end{pmatrix} = U \begin{pmatrix} \nu_{1L} \\ \nu_{2L} \end{pmatrix}, \quad (2.36)$$

Define  $\nu_i = \nu_{iL} + (\nu_{iL})^c$  ( $i = 1, 2$ ), the Lagrangian 2.33 now can be written as[55, 61]:

$$-\mathcal{L} = \frac{1}{2} N_L^T \mathcal{C}^\dagger \mathcal{M} N_L + h.c. = \frac{1}{2} \nu_L^T \mathcal{C}^{-1} \mathcal{M}_{diag} \nu_L + h.c. = \frac{1}{2} (|m_1| \bar{\nu}_1 \nu_1 + |m_2| \bar{\nu}_2 \nu_2). \quad (2.37)$$

On the other hand, the mass eigenvalues are solved as:

$$m_{1,2} \equiv m_{\mp} = \frac{1}{2} [ (m_L^M + m_R^M) \mp \sqrt{(m_L^M - m_R^M)^2 + 4(m^D)^2} ], \quad (2.38)$$

From (2.38), there are 4 cases to discuss:

(1) If  $m_L^M = m_R^M = 0$  (called “Dirac limit”), then  $m_{1,2} = m^D$  and neutrinos are pure Dirac particles.

(2) If  $m^D \gg m_{L,R}^M$ , then  $\tan 2\theta = \frac{2m^D}{m_R^M - m_L^M} \gg 1$  and  $\theta \simeq \pi/4$ ,  $m_{L,R}^M/m^D \rightarrow 0$ ,  $m_{1,2} = \frac{1}{2} m^D [ \frac{(m_L^M + m_R^M)}{m^D} + \sqrt{(\frac{m_L^M - m_R^M}{m^D})^2 + 4} ] \simeq \frac{1}{2} m^D (0 + \sqrt{0+4}) = m^D$ , the pair of Majorana neutrinos behaves like one Dirac neutrino, which is called a Pseudo-(or quasi-)Dirac Neutrino.

(3) If  $m^D = 0$ ,  $m_1 = m_L^M$ ,  $m_2 = m_R^M$ , neutrinos are pure Majorana particles.

(4) If  $m_R^M \gg m^D, m_L^M$ , then  $\theta \simeq (m^D/m_R^M) \ll 1$  and  $\tan 2\theta = \frac{2m^D}{m_R^M - m_L^M} \rightarrow 0$ , we get:

$$\begin{aligned} m_1 = m_- &= \frac{1}{2} \frac{(m_L^M + m_R^M)^2 - (m_L^M - m_R^M)^2 - 4(m^D)^2}{m_L^M + m_R^M + |m_L^M - m_R^M| \sqrt{1 + (\frac{2m^D}{m_L^M - m_R^M})^2}} \simeq \frac{2m_L^M m_R^M - 2(m^D)^2}{m_L^M + m_R^M + (m_R^M - m_L^M)} \\ &= |m_L^M - (m^D)^2/m_R^M|, \end{aligned} \quad (2.39)$$

<sup>3</sup> and:

$$m_2 = m_+ = \frac{1}{2} [m_R^M + m_R^M (1 + \frac{1}{2} (2m^D/m_R^M)^2)] = m_R^M [1 + (m^D/m_R^M)^2]. \quad (2.40)$$

---

<sup>3</sup>Here the absolute value is taken because we can find proper  $\rho_{1,2}$  values to ensure  $m_1 \geq 0$ .

In the case of (4), since  $\theta \ll 1$ ,  $U \simeq \text{diag}(\rho_1, \rho_2)$ , from 2.36, the mass eigenstates  $\nu_1 \simeq \nu_L + (\nu_L)^c, \nu_2 \simeq \nu_R + (\nu_R)^c$ . Since  $\nu_{1,2} = (\nu_{1,2})^c$ , it means that the massive neutrino eigenstates are of Majorana nature. It also shows that the mass eigenstate  $\nu_2$  relates to the right-handed sterile neutrino  $\nu_R$  while the  $\nu_1$  relates to the left-handed active neutrino  $\nu_L$ . Considering  $m_L^M = 0$  in the Standard Model[55], if the sterile neutrino  $\nu_R$  is heavy, the mass of the active neutrino  $m_1 = (m^D)^2/m_R^M$  will be light. This is called the Seesaw Mechanism.

In the Seesaw Mechanism, new neutral force carriers or messenger particles with unknown masses  $M_x$  are added into the Standard Model. There are mainly three types of Seesaw mechanism, depending on what new particles are introduced. Generally, a dimension-5 operator  $\mathcal{O}_5 = \frac{\kappa}{M_X} \Psi_L \Psi_L \Phi \Phi$  is considered, where  $\kappa$  is an unknown dimensionless coupling constant,  $\Psi_L$  is the  $SU(2)_L$  lepton doublet and  $\Phi = (\phi^+, \phi^0)^T$  is the Higgs doublet[64]. Via symmetry breaking at the electroweak scale ( $v_0 = 246 \text{ GeV}$ ), the neutrino mass can be obtained as  $m_\nu = \kappa v_0^2/M_X$ . In the case (4), adding a neutral, heavy right-handed neutrino  $\nu_R$  is called the type-I, or the conventional Seesaw Mechanism; its tree-level Feynman diagram is shown in Fig. 2.5 (left). Since we know the Dirac mass  $m^D = y_\nu v_0$  (from 2.31),  $m_1 = y_\nu^2 v_0^2/m_R^M$ . Since  $m^D \propto v_0 \sim \mathcal{O}(100 \text{ GeV})$ , if the active neutrinos is in the mass scale of  $m_1 \sim \mathcal{O}(0.01 \text{ eV})$ , then  $m_R^M \sim \mathcal{O}(10^{15} \text{ GeV})$ , which is a value close to the expected grand unification theory (GUT) mass scale  $m_{\text{GUT}} \mathcal{O}10^{16}$ . For the type-II, heavy  $SU(2)_L$  triplet Higgs scalars  $\Delta$  are introduced; its diagram is shown in Fig. 2.5 (right). For the type-III, heavy triplet fermions are introduced; its diagram is similar to the type-I, but with different exchanging particles.

As a summary, to explain how the neutrinos acquire their masses, New Physics theories are required to extend the Standard Model. If neutrinos are Majorana particles, the induced Seesaw Mechanism can explain the tiny mass of the active neutrinos naturally. As a bonus, the mass scale required by the Seesaw Mechanism implies the New Physics in GUT.

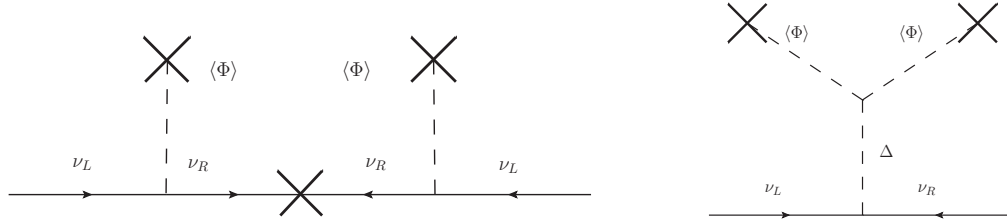


Figure 2.5: Tree-level Feynman diagrams for the Seesaw Mechanisms, modified from [4]: type-I (left) and type-II (right). The type-III scheme shares the same diagram to the type-I, but with the  $\nu_R$  replaced by  $T^0$ .

## 2.6 Measure the Absolute Neutrino Mass

The results from the neutrino flavor transformation experiments proved that neutrinos are not massless and have finite masses. However, in these experiments, the mass differences, rather than the absolute mass values are measured so we can not know the absolute scale of neutrino masses from these results. Currently, there are mainly three approaches to probe the neutrino masses: (1) cosmological measurements; (2) direct measurements for the  $\beta$ -decay spectrum; (3) a search for the  $0\nu\beta\beta$  process[4].

### 2.6.1 Cosmological Approach

Neutrinos play an important role in the formation and evolution of the universe. From the hot big bang model, there exists a relic sea of neutrinos forming a Cosmic Neutrino Background (CNB)[62]. Though the CNB has not been detected, the massive neutrinos can leave imprints on cosmological observables, such as the anisotropies of the Cosmic Microwave Background (CMB) temperature spectra, the matter power spectrum from the large-scale structure and the Baryon Acoustic Oscillations (BAO)[65, 66].

Combining the CMB data from the Planck space observatory (updated to 2018 results) with the BAO measurements, a tight 95% constraint on the sum of the masses of the three active types of neutrinos is obtained as:  $\sum m_\nu < 0.12 \text{ eV}$ [67]. Currently the cosmological approaches provide the strongest upper limit of the sum of neutrino masses[65]. On the other hand, these measurements are strongly model dependent. For example, the measurements

based on CMB mainly depend on the Lambda Cold Dark Matter ( $\Lambda CDM$ ) model, which is a standard model of Big Bang cosmology.

### 2.6.2 Direct Kinetic Measurements from Beta Decay

The classical experiments in history were designed to measure the kinetic energy of the emitted electron from the  $\beta^-$ -decay:  $(Z, A) \rightarrow (Z + 1, A) + e^- + \bar{\nu}_e$ , where  $A$  is the nucleon number and  $Z$  is the atomic or proton number. The energy difference between the initial and final state nuclei is the sum of the emitted electrons  $e^-$  (called the  $\beta$ -electron) energy  $E_e$ , the antineutrino  $\bar{\nu}_e$  energy  $E_\nu$  and the nuclear recoil energy  $E_R$ :  $Q = E_e + E_\nu + E_R$ . If considering the initial and final nuclei are at rest and  $E_R$  is negligible, due to the presence of  $E_\nu$ ,  $E_e$  can range from 0 to the maximal energy  $E_0 = Q$  (called the end-point energy). For the  $\beta$ -electron with a rest mass  $m_e$ , the kinetic energy  $T_e = E_e - m_e$  (taking the natural unit  $\hbar = c = 1$ ) and the momentum  $p_e = \sqrt{E^2 + 2Em_e}$ . Then by using the Fermi's Golden Rule, the differential  $\beta^-$ -decay spectrum of  $T_e$  is given by[68]:

$$\frac{d^2N}{dtdT_e} = \frac{G_F^2 \cos^2 \theta_C |\mathcal{M}_{nucl}|^2}{2\pi^3} \cdot F(Z + 1, T_e) \cdot (T_e + m_e) \cdot p_e \cdot (E_0 - T_e) \cdot \sqrt{(E_0 - T_e)^2 - m_{\bar{\nu}_e}^2} \Theta(E_0 - T_e - m_{\bar{\nu}_e}), \quad (2.41)$$

where  $G_F$  is the Fermi constant;  $\theta_C$  is the Cabibbo angle;  $\mathcal{M}_{nucl}$  is the nuclear matrix element (NME);  $F(Z, E)$  is the Fermi function describing the electromagnetic interaction between the  $\beta$ -electron and the final-state nucleus; and the Heaviside step function  $\Theta$  ensures that a neutrino can only be emitted if enough energy is left for its mass.

In this spectrum,  $m_{\bar{\nu}_e}^2$ , the square of the  $\bar{\nu}_e$  rest mass is the measurement observable. It can be evaluated by measuring the  $\beta$ -decay event rate[68].

If considering  $m_{\nu_e} = m_{\bar{\nu}_e}$  and the CPT is conserved,  $\langle m_{\bar{\nu}_e}^2 \rangle = \langle m_{\nu_e}^2 \rangle = \sum_i |U_{ei}|^2 m_i^2 = \sum_i |U_{ei}|^2 m_i^2$ . Taking out the lightest mass eigenvalue:  $m_1$  for normal hierarchy and  $m_3$  for inverted hierarchy, the  $\langle m_{\bar{\nu}_e}^2 \rangle$  can be expressed as[53]:

$$\langle m_{\bar{\nu}_e}^2 \rangle = \begin{cases} m_1^2 + s_{13}^2 |\Delta m_{31}^2| + c_{13}^2 s_{12}^2 \Delta m_{21}^2 & (\text{for NH}) \\ m_3^2 + c_{13}^2 |\Delta m_{31}^2| + c_{13}^2 s_{12}^2 \Delta m_{21}^2 & (\text{for IH}), \end{cases} \quad (2.42)$$

where  $s_{13}^2, c_{13}^2, \Delta m_{31}^2$  and  $\Delta m_{21}^2$  are the flavor transformation parameters and they are determined by flavor transformation experiments. If taking the currently best global-fit values with  $3\sigma$  (the values in brackets are for IH and the others are for NH):  $\Delta m_{21}^2 = 7.37 \times 10^{-5} \text{ eV}^2$ ,  $|\Delta m_{31}^2| = 2.56$  ( $2.54$ )  $\times 10^{-3} \text{ eV}^2$ ,  $s_{12}^2 = 0.297$ ,  $s_{13}^2 = 0.0215$  ( $0.0216$ )[31], then for NH,  $\langle m_{\nu_e}^2 \rangle \simeq m_1^2 + (8.74 \text{ meV})^2$  and for IH,  $\langle m_{\nu_e}^2 \rangle \simeq m_3^2 + (50.3 \text{ meV})^2$ . Fig. 2.6.2 plots the  $\sqrt{\langle m_{\nu_e}^2 \rangle}$  as a function of the lightest mass eigenvalue. Therefore, once the  $m_{\nu_e}^2$  is

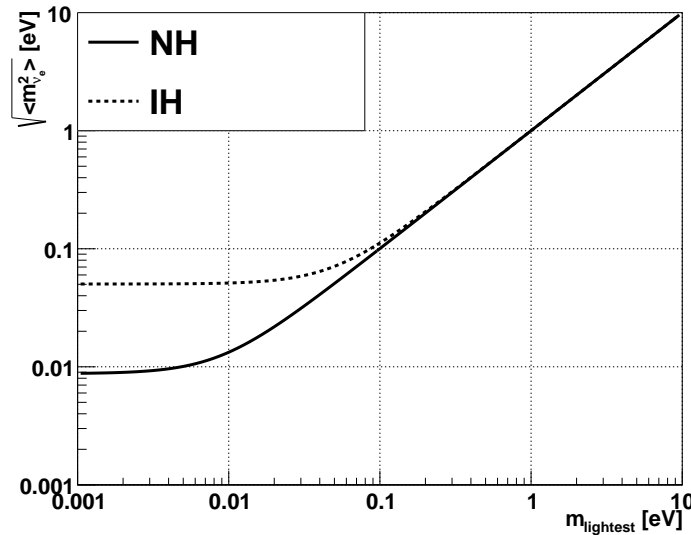


Figure 2.6:  $\sqrt{\langle m_{\nu_e}^2 \rangle}$  as a function of the lightest mass ( $m_1$  for NH or  $m_3$  for IH).

measured, the mass hierarchy as well as the mass eigenvalues  $m_i$  can be determined.

Among the  $\beta$ -decay processes, the tritium process:  ${}^3\text{H} \rightarrow {}^3\text{He}^+ + e^- + \bar{\nu}_e$  has a low endpoint energy  $E_0 = 18.57 \text{ keV}$ , a favorable half-life  $T_{1/2} = 12.32 \text{ years}$  and simple atomic structure for calculation. With these experimental advantages, it has been largely investigated since 1947 and is used as a standard technology for the kinetic measurement[44]. The KArlsruhe TRItium Neutrino (KATRIN) experiment is one of the state-of-the-art tritium experiments which uses a large magnetic spectrometer with high energy resolution for a precise measurement. In 2019, the experiment reported an upper limit of  $m_\nu < 1.1 \text{ eV}$  with 90% C.L.. After 5 years of measurement, the experiment is expected to reach the  $m_\nu$  sensitivity down to 0.2 eV with 90% C.L.[69].

### 2.6.3 Double Beta Decay

For heavy radioactive isotopes ( $A > 70$ ) with nuclei of even neutron number and even proton number (called even-even nucleus), beta decay will lead to an odd-odd nucleus which is less stable. Thus for such isotopes the  $\beta$ -decay is energetically forbidden. In 1935, Maria Goeppert-Mayer pointed out that these isotopes can still decay through a double beta decay process:  $(Z, A) \rightarrow (Z + 2, A) + 2e^- + 2\bar{\nu}_e + Q_{\beta\beta}$ , where  $Q_{\beta\beta}$  is the released energy. This is called ordinary double beta decay or  $2\nu\beta\beta$ , which is allowed by the Standard Model and with a typical half-life  $T_{1/2} > 10^{19}$  years (yr)[70, 71].

If neutrinos are Majorana particles, a process called neutrinoless double beta decay ( $0\nu\beta\beta$ ) will also be expected:  $(Z, A) \rightarrow (Z + 2, A) + 2e^- + Q_{\beta\beta}$ . In this process, the lepton number is violated by 2, which is not allowed in the SM. As mentioned in 2.5, New Physics interpretations for the process are required. The Feynman diagrams of  $2\nu\beta\beta$  and  $0\nu\beta\beta$  are illustrated in Fig. 2.7.

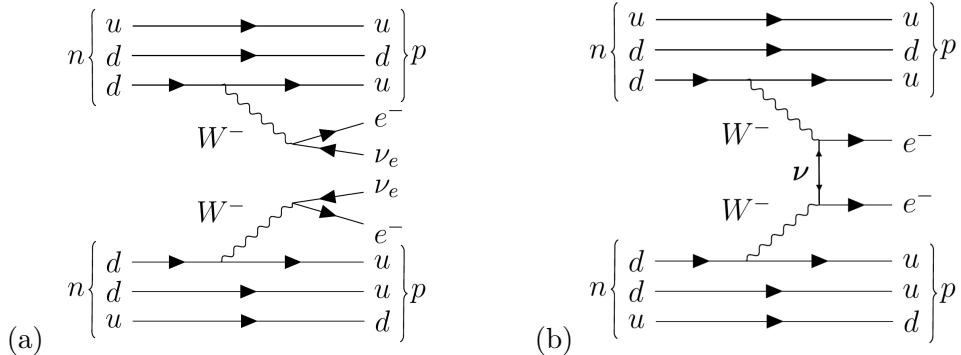


Figure 2.7: Feynman diagrams for  $2\nu\beta\beta$  (a) and  $0\nu\beta\beta$  (b).

One of the simple interpretations is the exchanging of virtual light Majorana neutrinos between the nucleus, as shown in Fig. 2.7 (b). Under the SM weak interactions, the amplitude of the lepton processes in the  $0\nu\beta\beta$  is a product of two weak charged current interactions happening at the vertices  $x$  (creating a  $\nu_{eL}$  and an  $e^-$ ) and  $y$  (absorbing a  $\nu_{eL}$  and creating an  $e^-$ ) [38]:

$$\mathcal{A} = \bar{e}(x)\gamma^\mu\nu_{eL}\nu_{eL}^T(y)\gamma_\mu^T\bar{e}^T(y), \quad (2.43)$$

Taking account of the three-neutrino mixing as well as the Majorana condition:  $\nu_i^c =$

$\mathcal{C}\bar{\nu}_i^T = \nu_i$ , the amplitude becomes[38, 72]:

$$\mathcal{A} = -\sum_{i=1}^3 U_{ei}^2 \frac{1-\gamma_5}{2} \nu_i(x) \bar{\nu}_i(y) \frac{1-\gamma_5}{2} \mathcal{C} \quad (2.44)$$

is propagator for a mass  $m_i$  virtual fermion transiting between vertices.

For the case of small neutrino mass,  $p \gg m_i$ , then  $\mathcal{A} \propto m_{ee} \equiv \sum_{i=1}^3 U_{ei}^2 m_i$  the effective Majorana mass

$\nu_i(x) \bar{\nu}_i(y)$  with a proper time ordering:

$$\begin{aligned} \langle T(\nu_i(x) \bar{\nu}_i(y)) \rangle &= -\frac{i}{(2\pi)^4} \int dp^4 e^{-iq(x-y)} \frac{\gamma^\mu p_\mu + m_i}{p^2 - m_i^2} \\ &= -\sum_{i=1}^3 U_{ei}^2 m_i \frac{1}{p^2 - m_i^2} \frac{1-\gamma_5}{2} \mathcal{C}. \end{aligned}$$

Therefore, the massive Majorana neutrino is required for the existence of the  $0\nu\beta\beta$  process. where

[73].

From [31],

transition between  $\bar{\nu}_{eR}$  and  $\nu_{eL}$ . underlying mechanisms

$$|\bar{\nu}_{eR}(t = \delta t)\rangle = |\bar{\nu}_{eR}\rangle - i \sum_{i=1}^3 m_i U_{ei} |\nu_{iL}\rangle \delta t$$

$$\text{amplitude } \langle \nu_{eL} | \bar{\nu}_{eR} \rangle = -i \sum_{i=1}^3 m_i U_{ei}^2 \delta t$$

Integrating the  $\delta t$  with a weight of the nuclear matrix element, the decay width and the half-life are obtained as[53, 74]:

$$\Gamma = (T_{1/2}^{0\nu\beta\beta})^{-1} = G_{PS}(Q, Z) |M_{Nuclear}|^2 \langle m_{ee} \rangle^2, \quad (2.45)$$

where  $G_{PS}(Q, Z)$  is a phase space corresponding to effective coupling constant, which depends on the endpoint energy  $Q$  and the atomic number  $Z$ ;  $|M_{Nuclear}|$  is the nuclear matrix element describing the nuclear transition and it can only be calculated theoretically from approximate methods based on many-body nuclear models, such as the Nuclear Shell Model (NSM),

interacting shell model (ISM) the Quasiparticle-Random Phase Approximation (QRPA), Interacting Boson Model (IBM), Energy Density Functional Method (EDF) and Projected Hatree-Fock-Bogoliubov Method (PHFB).

In this case the effective Majorana mass

$$\langle m_{ee} \rangle = \left| \sum_{i=1}^3 U_{ei}^2 m_i \right| = |c_{13}^2 c_{12}^2 m_1 + c_{13}^2 s_{12}^2 e^{i\alpha_1} m_2 + s_{13}^2 e^{i\alpha_2} m_3|, \quad (2.46)$$

where  $U_{ei}$  are the elements of the neutrino mixing matrix for the flavor state  $\nu_e$ , and  $m_i$  are the mass eigenvalues of the mass eigenstates (2.1));  $\alpha_1, \alpha_2$  are Majorana CP-violation phase factors and  $\alpha_2$  can also be taken as  $\alpha_2 - \delta_{CP}$ .

For NH,  $m_{lightest} = m_1$ ,  $m_2 = \sqrt{m_1^2 + \Delta m_{21}^2}$ ,  $m_3 = \sqrt{m_1^2 + |\Delta m_{31}^2|}$ ; for IH,  $m_{lightest} = m_3$ ,  $m_1 = \sqrt{m_3^2 + |\Delta m_{31}^2|}$ ,  $m_2 = \sqrt{m_3^2 + |\Delta m_{31}^2| + \Delta m_{21}^2}$

The phases  $\alpha$  and  $\beta$  are ranging from 0 to  $\pi$ , taking different pairs of  $(\alpha_1, \alpha_2) = (0, 0), (0, \pi), (\pi, 0)$  and  $(\pi, \pi)$  can determine the ranges of  $\langle m_{ee} \rangle$ .

Using the same best-fit values in the 2.6.2, a plot of  $\langle m_{ee} \rangle$  as a function of  $m_{lightest}$  is shown in Fig. 2.6.3.

the mass regions are bounded by lines taking different values of  $(\alpha_1, \alpha_2)$ .

Similar to the  $\beta$ -decay case, the  $2\nu\beta\beta$  process will cause a continuous spectrum in the detector while the  $0\nu\beta\beta$  process only has two electrons in the final state. These electrons take away the entire energy and their energy spectrum sum up to give a distinct energy peak at the Q-value. Taking the isotope  $^{130}\text{Te}$  as an example, Fig. 2.9 illustrates the shapes of the energy spectrum from the  $2\nu\beta\beta$  and the  $0\nu\beta\beta$  decay processes.

By measuring this distinct energy peak, a detector with high energy resolution is able to search for the  $0\nu\beta\beta$  signal from the  $0\nu\beta\beta$  decay radioactive isotopes. Diverse technologies have been developed during the past decades. The following section lists some of the mainstream experiments.

#### 2.6.4 Status of Double Beta Decay Experiments

There are 35 isotopes can undergo the double beta decay process, but only a few of them are suitable for the application in direct  $0\nu\beta\beta$  search experiments[61]. From the experimental view, the candidate isotopes are expected to have relatively high natural abundances, high Q-values, be deployed in a large amount with low costs, and are not toxic to the environment

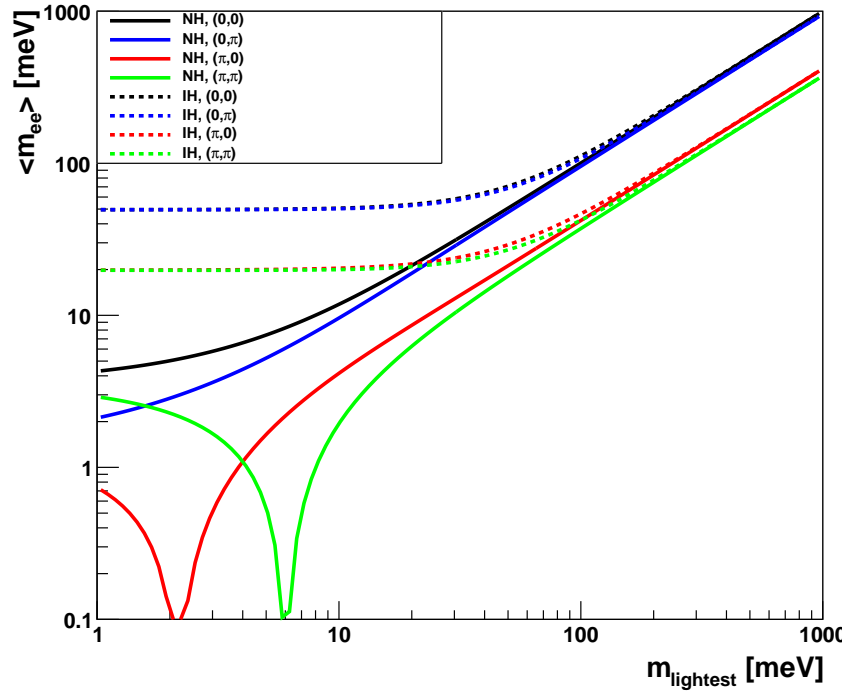


Figure 2.8: Effective Majorana mass as a function of the lightest mass eigenvalue. Solid lines are for NH cases and dashed lines are for IH. Different colors stand for taking different values of  $(\alpha_1, \alpha_2)$ .

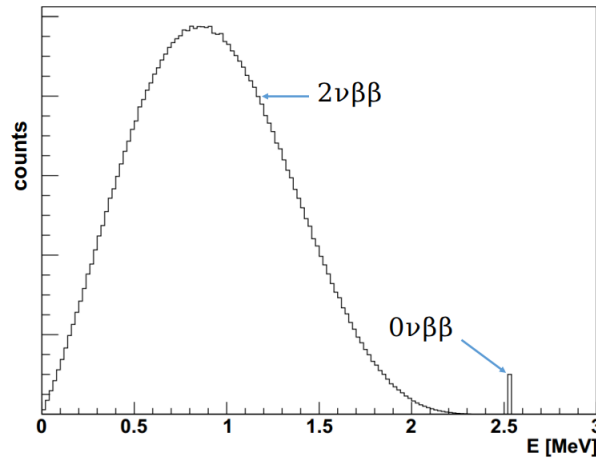


Figure 2.9: Energy spectrum of the  $^{130}\text{Te}$   $2\nu\beta\beta$  decay and the hypothetical  $0\nu\beta\beta$  decay. The SNO+ simulation package (RAT) was used to produce the plot.

as well. However, in realistic situation there is no isotope fulfills all these properties and the current experiments making trade-offs[73].

The experiments searching for direct signals of  $0\nu\beta\beta$  mainly measure the physics properties of the two emitted electrons, such as their energies, momentum and tracks.

inhomogeneous experiments use external  $\beta\beta$  source while homogeneous experiments use  $\beta\beta$  source as the detection medium, which are mainly referred as calorimeter experiments[75, 76].

$^{136}\text{Xe}$ ,  $^{48}\text{Ca}$ ,  $^{76}\text{Ge}$ ,  $^{130}\text{Te}$

At the time of writing,

$0\nu\beta\beta$  in the range of  $10^{25} - 10^{26}$  year,

The observed number of event in expectation is:

$$N_{event} = \ln 2 \frac{N_A}{M_A} \frac{\alpha \cdot \epsilon \cdot m \cdot t}{T_{1/2}^{0\nu}},$$

where  $N_A$  is the Avogadro's number,  $\alpha$  is the abundance of the isotope in the element,  $M$  is the molar mass of the isotope and  $t$  is the measurement time of total exposure.

The GERmanium Detector Array (GERDA) experiment searches for  $0\nu\beta\beta$  of  $^{76}\text{Ge}$ . The experiment uses bare germanium crystals with an enrichment of up to  $\sim 87\%$   $^{76}\text{Ge}$  operated in a radiopure cryogenic liquid argon (LAr)[77]. GERDA Phase I had an exposure of 21.6 kg·yr and Phase-II started with 35.6kg from enriched material in December 2015. With combined data of Phase I and Phase II,

a total exposure of 82.4 kg·yr

In 2017, GERDA reported a 90% confidence level (C.L.) lower limit for the half-life of  $^{76}\text{Ge}$ ,  $T_{1/2}^{0\nu}(^{76}\text{Ge}) > 8.0 \times 10^{25}$  years.

GERDA reported in 2019 a lower limit half-life of  $T_{1/2}^{0\nu}(^{76}\text{Ge}) > 0.9 \times 10^{26}$  years at 90% C.L.[78]. effective  $m_{ee}$  is [104,228] meV.

A new experiment, the Large Enriched Germanium Experiment forNeutrinoless Double-Beta Decay (LEGEND) will

Building on the successes of the MAJORANA DEMONSTRATOR and GERDA,

The Enriched Xenon Observatory (EXO) experiment uses 200-kg liquid Xenon (LXe) time projection chamber (TPC) to search for  $0\nu\beta\beta$  in  $^{136}\text{Xe}$ . In 2011 they observed the half life of double beta decay of  $^{136}\text{Xe}$  to be  $2.11 \times 10^{21}$  years and in 2014 they set a limit on  $T_{1/2}^{0\nu}(^{136}\text{Xe}) > 1.1 \times 10^{25}$  yr[79]. EXO is now upgrading to the next 5-tonne experiment (nEXO) and is expected to reach an exclusion sensitivity of  $T_{1/2}^{0\nu}(^{136}\text{Xe})$  to about  $10^{28}$  years at 90% C.L.[80].

Also looking into  $^{136}\text{Xe}$ , the KamLAND-Zen (ZZeroNeutrino) experiment exploits the existing facilities of KamLAND by setting a 3.08-m-diameter spherical inner balloon filled with 13 tons of Xe-loaded liquid scintillator at the center of the KamLAND detector.

liquid scintillator cocktail of 82% decane and 18% pseudocumene by volume, 2.7 g/L PPO.

photocathode coverage of 34%.

Their 2016 results from a 504 kg·yr exposure obtained a lower limit for the  $0\nu\beta\beta$  decay half-life of  $T_{1/2}^{0\nu}(^{136}\text{Xe}) > 1.07 \times 10^{26}$  yr at 90% C.L. and the corresponding upper limits on the effective Majorana neutrino mass are in the range 61 – 165 meV[81].

The Particle and Astrophysical Xenon Experiment III (PandaX-III) uses a high pressure gas-phase time projection chamber (TPC).

The Cryogenic Underground Observatory for Rare Events (CUORE) experiment searches for  $0\nu\beta\beta$  in  $^{130}\text{Te}$ . CUORE is a ton-scale cryogenic bolometer array that arranges 988 tellurium dioxide ( $\text{TeO}_2$ ) crystals. CUORE reported first results in 2017 after a total  $\text{TeO}_2$  exposure of 86.3 kg·yr. An effective energy resolution of  $(7.7 \pm 0.5)$  keV FWHM and a background count of  $(0.014 \pm 0.002)$   $\text{counts}/(\text{keV} \cdot \text{kg} \cdot \text{yr})$  in the ROI were achieved in that data exposure. Combined with the early data (the data from the two precursor experiments, Cuoricino and CUORE-0), they placed a lower limit of  $T_{1/2}^{0\nu}(^{130}\text{Te}) > 1.5 \times 10^{25}$  yr at 90% C.L. and  $m_{\beta\beta} < (110 - 520)$  meV[82]. In 5 years live time, the experiment will give a projected sensitivity of  $9.5 \times 10^{25}$  yr at the 90% C.L. and set an upper limit on the effective Majorana mass in the range 50 – 130 meV[83].

A more recent evaluations of the limits of  $T_{1/2}^{0\nu}$  and  $m_{\beta\beta}$  from the above mentioned

current and future experiments are summarized in

Table 2.3: The limits of  $T_{1/2}^{0\nu}$  and  $m_{\beta\beta}$  at 90% C.L.

Experiment	Isotope	Limit of $T_{1/2}^{0\nu}$ ( $10^{25}$ year)	Limit of $m_{\beta\beta}$ (eV)
GERDA	$^{76}\text{Ge}$	>8.0	<0.12-0.26
KamLAND-Zen	$^{136}\text{Xe}$	>10.7	<0.05-0.16
EXO	$^{136}\text{Xe}$	>1.1	<0.17-0.49
CUORE	$^{130}\text{Te}$	>1.5	<0.11-0.50

$3\sigma$  discovery sensitivities assuming 5 years of live time. Table 2.3[84, 78].

For planned future experiments

SNO+ Phase-I and II

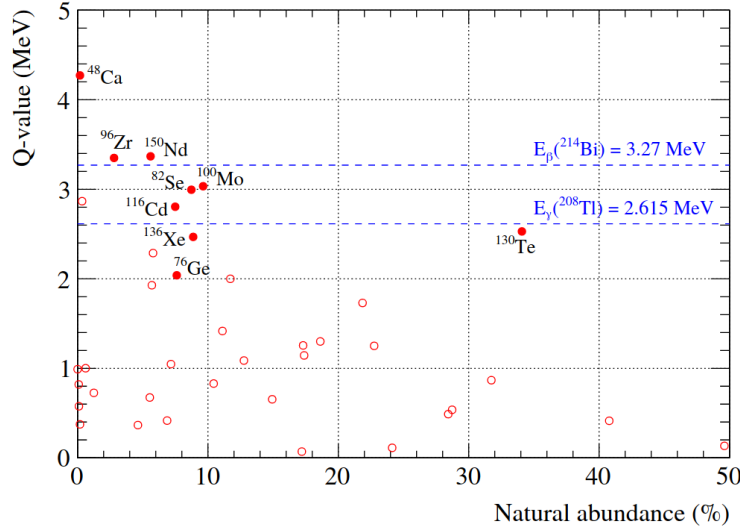


Figure 2.10: Natural abundance vs. Q-values for different  $2\nu\beta\beta$  isotopes[5].

Table 2.4: The limits of  $T_{1/2}^{0\nu}$  and  $m_{\beta\beta}$  at 90% C.L.

Experiment	Isotope	$m_{isotope}$ [kg]	$T_{1/2}^{0\nu}$ [ $\times 10^{25}$ year]	$m_{\beta\beta}$ [meV]
LEGEND 1k	$^{76}\text{Ge}$		84	0.04-0.073
KamLAND2-Zen	$^{136}\text{Xe}$		10.7	0.05-0.16
nEXO	$^{136}\text{Xe}$		410	0.09-0.022
NEXT 100	$^{136}\text{Xe}$	91	5.3	82-198
PandaX-III 200	$^{136}\text{Xe}$		8.3	
CUORE	$^{130}\text{Te}$		1.5	0.11-0.50
SNO+ Phase I	$^{130}\text{Te}$		11	
SNO+ Phase II	$^{130}\text{Te}$		48	

## Chapter 3

# The SNO+ Experiment

### 3.1 Overview

The SNO+ experiment is located at SNOLAB. This deep underground facility sits at Vale’s Creighton mine in Sudbury, Ontario, Canada (coordinate:  $46^{\circ}28'19.6''\text{N}$ ,  $81^{\circ}11'12.4''\text{W}$ ). It provides an environment with extremely low cosmic ray backgrounds. At sea level, an average cosmic muon ( $\mu$ ) flux rate is about  $1.44 \times 10^7 \mu/\text{m}^2/\text{day}$ [85]. Cosmic muons with high energies (mostly  $\mathcal{O}(\text{GeV})$ ) can induce spallation backgrounds, such as fast neutrons and lasting isotopes, which are harmful to the low background counting experiments[86]. The SNOLAB has a  $2092 \pm 6$  m flat overburden of rock, which is  $5890 \pm 94$  water equivalent meter (m.w.e). This rock overburden ensures that cosmic muon ( $\mu$ ) flux rate is as low as  $0.286 \pm 0.009 \mu/\text{m}^2/\text{day}$ [5], which means that every hour only about 1  $\mu$  passes through the SNO+ detector.

The SNO+ detector is a refurbishment of the SNO detector. The SNO+ collaboration makes use of the SNO infrastructure and upgraded it to be a liquid scintillator detector. As shown in Fig. 3.1, the detector is inside a barrel-like rock cavity with a diameter of 22 m at its waist and a height of 34 m. The cavity is filled with 7000 tonnes of ultrapure water (UPW) to provide buoyancy for the vessel and also to shield radiation backgrounds from the environment, such as the cosmic rays and isotope decays from the rock.

The detector consists of an acrylic vessel (AV) sphere of 12.01 m in diameter and 5.5 cm in thickness. The AV contains detection media and is held in place by a rope net system including hold-up and hold-down Tensylon ropes. This spheric structure is simple in geometry and reduces the complexities of simulation and event reconstruction. Furthermore, this geometry allows for spherical fiducial volume cuts from the center of the AV to further get rid of external backgrounds, which makes the SNO+ as a graded-shield type detector[87]. On the top of the AV sphere, there is an acrylic neck cylinder with 6.8 m high and 1.46 m inner diameter. The neck connects the AV sphere to the facilities on the deck above the detector. Through the neck, pipes can fill the detection medium into the AV and recirculate as well. Calibration sources for internal scans can also be lowered down into the AV through the neck.

The AV sphere is concentric within a stainless steel photomultiplier (PMT) support structure (PSUP), which is a geodesic dome with an average radius of 8.4 m. Hamamatsu 8-inch R1408 PMTs were mounted on the PSUP and 9394 PMTs are looking inward to the AV. A 27 cm diameter concentrator consisting of pedals coated with aluminum was mounted on each PMTs to increase their light collection efficiency as well as the photocathode coverage of the detector, which reaches about 54% effective coverage. Besides the inward-looking PMTs, 90 PMTs are looking outward, serving as muon vetos. Four Hamamatsu R5912 High Quantum Efficiency (HQE) PMTs were also installed for testing the performance of potential SNO+ phases-II[88].

## 3.2 SNO+ Physics Phases

The SNO+ experiment is designed for multi-purpose measurements of neutrino physics. The detector has been running since December 2016. There are three physics phases of the experiment and each phase has different detection media inside the AV: the water phase, the scintillator phase, and the tellurium phase[89].

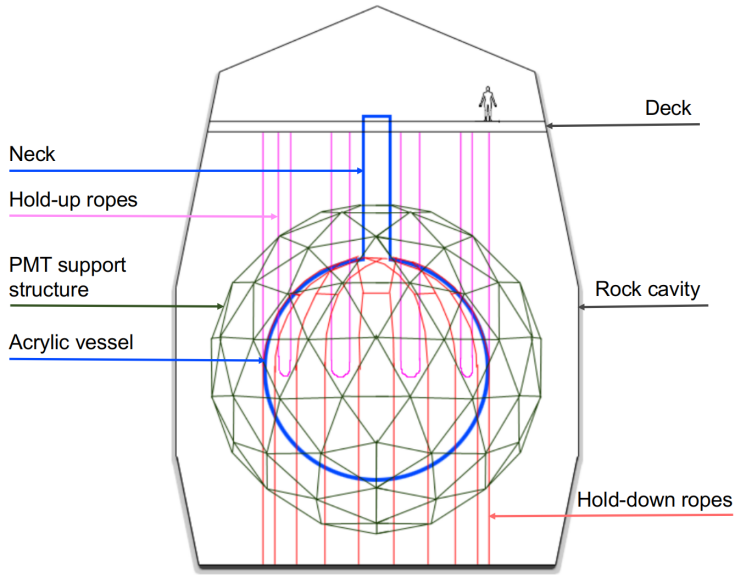


Figure 3.1: The SNO+ detector labelled with main structures, figure modified from [6].

### Water Phase

In this initial phase, the AV was filled with about 905 tonnes of ultrapure water. The detector collected water physics data from May 2017 to July 2019.

During the data-taking, different types of calibration runs have been taken. The detector timing and energy response, systematics, and backgrounds are studied. Multiple physics analyses of invisible nucleon decay, solar neutrinos, and reactor antineutrinos are ongoing and a few results have been published[90, 91, 92]. The external backgrounds are also measured, which will be the same as the following two phases.

The main physics goal in this phase is to search for the invisible nucleon decay, which violates baryon number and is a prediction of Grand Unified Theory (GUT). In the invisible decay mode, a proton or a bound neutron decays away without releasing charged particles, compared to the “visible” decay channels of  $p \rightarrow e\pi$  and  $p \rightarrow \nu K$  which has been searched and set limits by the SuperK experiment. In the SNO+ water detector,  $^{16}\text{O}$  may decay into  $^{15}\text{O}^*$  (bound neutron invisible decay) or  $^{15}\text{N}^*$  (proton invisible decay) excited state. The  $^{15}\text{O}^*$  has 44% chance to deexcite to produce 6.18 MeV  $\gamma$  ray and 2% chance to produce

7.03 MeV  $\gamma$ ; while  $^{15}\text{N}^*$  has 41% to release 6.32 MeV  $\gamma$  and 7.01, 7.03 and 9.93 MeV  $\gamma$  with chances of 2%, 2% and 3% respectively. The experiment has searched for these  $\gamma$  signals and the first publication sets world-leading limits of  $\mathcal{O}(10^{29})$  years for both the proton and neutron invisible decay lifetime at 90% Bayesian credibility level[90].

The  ${}^8\text{B}$  solar neutrinos were measured with a 69.2 kilo-tonnes·day dataset. By analyzing the solar neutrino elastic scattering events based on the dataset (the method will be discussed in Chapter 5 with more details), the number of the solar neutrino events were counted in different energy regions. In the first publication[91], by fitting to the non-oscillation solar neutrino model, an observed flux was obtained from the dataset to be  $2.53_{-0.28}^{+0.31}(\text{stat.})_{-0.10}^{+0.13}(\text{syst.}) \times 10^6 \text{ cm}^{-2}\text{s}^{-1}$  for the  ${}^8\text{B}$  solar neutrinos with energies larger than 5 MeV. In the energy region larger than 6 MeV, the dataset has a background rate of  $0.25_{-0.07}^{+0.09}$  events/kilo-tonne·day, which is extremely pure with solar neutrinos. Currently, this background rate is the lowest one compared to the other water Cherenkov detectors[91].

Reactor antineutrinos can be captured by the SNO+ detector and get measured. 40% of these antineutrinos are from one nearby reactor complex in Canada at a 240-km baseline; 20% are from two Canadian complexes at around 350 km; the rest are from the USA and elsewhere with longer baselines[89]. Though in pure water the antineutrino event rate is much smaller than in the scintillator, during the water phase, SNO+ still has the potentials to detect reactor antineutrinos due to the low background dataset and relatively high detection efficiency. To evaluate the sensitivity for detecting reactor antineutrinos, an Americium-Beryllium (AmBe) calibration source was deployed during the water phase. This source provides neutrons along with 4.4-MeV  $\gamma$ s. Neutrons are captured by hydrogen and 2.2-MeV  $\gamma$ s are released. An analysis of delayed coincidence between 4.4-MeV and 2.2-MeV  $\gamma$ s can help to tag neutrons, which is crucial for tagging the reactor antineutrinos since they are measured by the inverse  $\beta$ -decay process which produces neutrons with similar energy scale. In the first publication for the SNO+ water phase, a neutron detection efficiency of 50% was obtained when the AmBe source was deployed at the center of the detector; the neutron-hydrogen capture time constant  $\tau$  was measured to be  $202.35_{-0.76}^{+0.87} \mu\text{s}$  and from  $\tau$ ,

a thermal capture cross-section was calculated to be  $336.3^{+1.2}_{-1.5}$  milli-barn (mb)[92].

### **Scintillator Phase**

In this phase, the AV will be filled with 780 tonnes of liquid scintillator, which is a mixture of linear alkylbenzene (LAB) as a solvent and 2 g/L of 2,5-diphenyloxazole (PPO) as a fluor. This LAB-based organic liquid scintillator is referred to as the “unloaded” liquid scintillator.

The main physics goal of the scintillator phase is to measure low energy solar neutrinos: the CNO, pep, and low energy  $^8\text{B}$  neutrinos. The pep neutrinos are mono-energetic, with  $E_\nu=1.442$  MeV and their flux is well predicted by the Standard Solar Model[93]. A measurement of the pep neutrinos will give more information on the matter effects in neutrino oscillations.

The solar metallicity is the abundance of elements heavier than  $^4\text{He}$  (called “metal” elements in the context of astronomy). It is poorly constrained and the predictions from different solar models disagree with each other. A measurement of the CNO neutrinos can give the abundance of  $^{12}\text{C}$ ,  $^{13}\text{N}$  and  $^{15}\text{O}$  and can thus resolve the metallicity problem[94].

Three kinds of antineutrinos will also be measured: reactor antineutrinos as mentioned before; geoneutrinos from natural radioactivity in the Earth; and the supernova neutrinos. SNO+ is planned to join the SuperNova Early Warning System (SNEWS), which is an international network of experiments with abilities to provide an early warning of a galactic supernova[5].

### **Tellurium Phase**

In this final phase, 0.5% natural Tellurium (Te) by mass (with 1.3 kilo-tonnes of  $^{130}\text{Te}$ ) will be loaded into the scintillator, which is referred to as the “Te-loaded” scintillator. Higher loading concentrations would be possible for a further loading plan[95]. The main purpose of this phase is to search for the  $0\nu\beta\beta$  signals in  $^{130}\text{Te}$ .

### 3.3 Detection Medium

In the SNO+ detector, charged particles are expected to interact with the detection medium and create Cherenkov lights and scintillation lights.

#### 3.3.1 Cherenkov Radiation

For any charged particle traveling in a transparent medium at an ultrarelativistic speed (a speed greater than the local phase speed of light in the medium), a kind of electromagnetic radiation, called Cherenkov radiation, can be emitted from the coherent response of the medium under the action of the field of the moving particle[96, 97].

Suppose a charged particle moves in a transparent, isotropic, and non-magnetic medium and creates an electromagnetic wave. The electromagnetic wave propagates with a wavenumber  $k = n \cdot \omega/c$ , where  $c$  is the speed of light in vacuum,  $n$  is the real-valued refractive index and  $\omega$  is the frequency. If the particle travels uniformly along x-axis with a velocity of  $v$ , the x-component of the wave vector is  $k_x = \omega/v$ . For a freely propagating wave,  $k > k_x$ , therefore  $v > v_p = c/n(\omega)$ , where  $v_p$  is the phase velocity in the medium. Under this condition that the speed of the charged particle is greater than the  $v_p$ , the Cherenkov radiation is emitted with a frequency of  $\omega$ [97].

The Cherenkov angle,  $\theta_c$  is the angle between the direction of the particle and the direction of Cherenkov emission and it is well-defined by  $\cos \theta_c(\omega) = \frac{c}{n(\omega)v}$ . The radiation is distributed over a surface of a cone with the half-opening angle  $\theta_c$ .

Consider the condition  $v > v_p = c/n(\omega)$ , for the case of  $e^-$  travelling in a water detector, if neglecting the dependency on  $\omega$ ,  $n_{water} \simeq 1.33$  [31], then  $\theta_c \simeq 41.25^\circ$  and  $v_p \simeq 2.254 \times 10^8 \text{ m/s}$ , which corresponds to a kinetic energy  $E_k = (\gamma - 1)mc^2 = 0.264 \text{ MeV}$  for  $e^-$ , where  $\gamma = 1/\sqrt{1 - v_p^2/c^2}$ . This is the lowest kinetic energy to create Cherenkov radiation, which is referred to the Cherenkov threshold ( $E_{thresh}$ ). In the case that the LAB-PPO liquid scintillator is the medium,  $n \simeq 1.50$ [98],  $\theta_c \simeq 48.19^\circ$  and for  $e^-$ ,  $E_{thresh} \simeq 0.175 \text{ MeV}$ .

For a particle with a charge of  $ze$ , the number of photons produced by Cherenkov

radiation per unit path length and per unit frequency of the photons is given by[99]:

$$\frac{d^2N}{d\omega dx} = \frac{\alpha^2(ze)^2}{c} \sin^2 \theta_c = \frac{z^2\alpha}{c} \left(1 - \frac{1}{\beta^2 n^2(\omega)}\right),$$

where  $\alpha$  is the fine structure constant.

Translate the frequency into the wavelength ( $\lambda = 2\pi\omega$ ) and integrate over the wavelength, we have the number of photons and  $x$  is along the particle track[99]:

$$\frac{dN}{dx} = 2\pi(ze)^2 \alpha \sin \theta_c \int_{\lambda_1}^{\lambda_2} \frac{d\lambda}{\lambda^2},$$

For optical photons with wavelengths ranging from 350 to 550 nm (typical PMT detection sensitive range), the above formula can be calculate into[99]:

$$\frac{dN}{dx} = 476(ze)^2 \sin^2 \theta_c \text{ photons/cm.}$$

For the Cherenkov radiation caused by  $e^-$  in a water detector,  $dN/dx \simeq 207 \text{ photons/cm}$ ; while in the LAB-PPO case,  $dN/dx \simeq 264 \text{ photons/cm}$ . In a realistic measurement, the detection efficiency and the coverage of photon sensors are also required to be taken into account.

### 3.3.2 Scintillation from Organic Scintillator

Besides the Cherenkov photons described in the previous section, the majority of lights emitted from the organic scintillator are scintillation photons.

The organic liquid scintillator can convert the kinetic energy of charged particles into scintillation photons with wavelengths in the sensitive detection region of PMTs. They are aromatic hydrocarbon compounds with benzene-ring structures. When ionizing radiation happens in the scintillator, the free valence electrons of the molecules are excited and transit to occupy the  $\pi$ -molecular orbitals with the benzene rings. These highly delocalized electrons are called  $\pi$ -electrons, which can occupy a series of energy levels. A Jablonski diagram, invented by Polish physicist Aleksander Jabłoński, is generally used to describe molecular absorbance and emission of light. In Fig. 3.2, the Jablonski diagram illustrates the  $\pi$ -electronic energy levels of an organic scintillator molecule[8, 99].

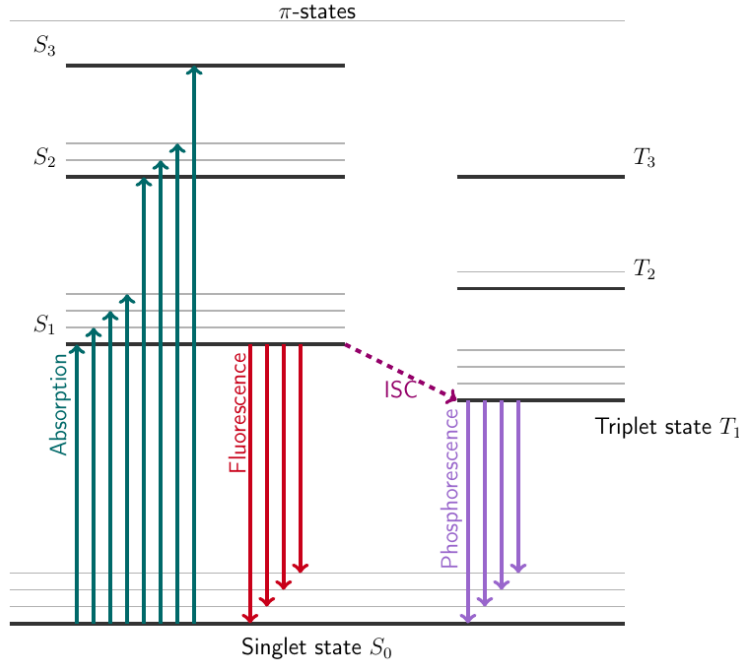


Figure 3.2: A Jablonski diagram for the organic scintillator, modified from [7, 8].

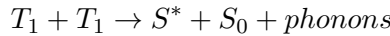
In the diagram,  $S_{0,1,2,3,\dots}$  are the energy levels of the spin-0 singlet states, where  $S_0$  is the ground state and  $S^* = S_{1,2,3,\dots}$  are the excited singlet states. Above the ground state  $S_0$ , there is also a set of spin-1 triplet states  $T_{1,2,3,\dots}$ , where  $T_1$  is the lowest triplet state. These electron energy levels are labeled with thick black lines. The energy spacings between these levels are  $\mathcal{O}(eV)$ . In each level, there are also fine structure levels that correspond to excited vibration modes of the molecule (labeled with gray lines and can be marked as  $S_{10}, S_{11}, \dots, S_{20}, S_{21}, \dots$ ). The energy spacing between these fine levels are  $\mathcal{O}(0.15\text{ eV})$ [99, 8].

The ionization radiation transfers the energy to the molecules and excites the electron levels as well as the vibrational levels, labeled as the absorption lines (in green). The decays between the excited singlet states (not to the ground state) are almost immediate ( $\leq 10\text{ ps}$ ) without the emission of light. This process is called internal degradation. The decays from the excited singlet state  $S_1$  (as well as the vibrational states  $S_{10}, S_{11}, S_{12}, \dots$ ) to the ground state (as well as the vibration states  $S_{01}, S_{02}, \dots$ ) happen promptly ( $\mathcal{O}(ns)$ ) and emit lights (labelled as red lines). This process is called fluorescence which contributes to the prompt

component of the emission of scintillation light. The probability of  $S_1$  decays into the vibrational states  $S_1 \rightarrow S_{01}, S_{02}, \dots$  among the ground state is more than  $S_1 \rightarrow S_0$ . Since the absorbed energy of  $S_0 \rightarrow S_1$  is larger than the emitted energy of  $S_1 \rightarrow S_{01}, S_{02}, \dots$ , the scintillators have very little self-absorption of the fluorescence and are transparent to their own radiation. The effect of Stokes shift, which refers to the overlap between the optical absorption and emission spectra, is small for the organic scintillator[99, 8].

The transitions between the singlet and triplet states are highly forbidden due to the electron spin-flip involved[100, 101]. There also exists a relatively rare process called intersystem crossing (ISC), which converts excited singlet states into triplet states. Besides this, 75% of triplet states can be produced by ionization-recombination[100, 102].

For the de-excitation, the similar processes of internal degradation occur among  $T_{2,3,\dots} \rightarrow T_1$ .  $T_1$  is a relatively stable state and the lifetime of the molecule in the triplet state is in  $\mathcal{O}(10^{-4} - 10 s)$ [103].  $T_1 \rightarrow S_0$  is highly forbidden. However, the  $T_1$  state can go through an indirect decay process by interacting with another excited  $T_1$  molecule and forms an excited singlet state:



The  $S^*$  will de-excite and emit delayed scintillation light. The process for emitting this delayed scintillation light is called delayed fluorescence or phosphorescence[99]. This process contributes to the delayed component of scintillation light.

For a typical scintillator detector, the time scale of detector response is  $\mathcal{O}(1-100 ns)$ . In this time region, the emission of the scintillation light contains the primary fluorescence from the de-excitation of the singlet states (prompt component) and the delayed fluorescence from the de-excitation of the indirect triplet states (delayed component)[102]. The time profile of the scintillation light emission is a mixture of prompt and delayed components.

Different charged particles can cause different ionization densities when they deposit energies to the scintillator molecules. The ionization density affects the relative population of the excited singlet and triplet states. Compared to an  $e^-$ , an  $\alpha$  particle can cause a high ionization density, which produces a higher ratio of triplet states. Therefore, the time profile

for the  $\alpha$  particle has more delayed components or longer tails than the  $e^-$ . This enables the organic scintillator to distinguish  $\alpha$  with  $e^-$  or other lighter charged particles[102, 104].

An empirical formula, called follows Birk's law[105, 7], describes the photon yield along with unit distance by the incident particle:

$$\frac{dY}{dx} = A \frac{dE/dx}{1 + k_B \cdot dE/dx},$$

where  $A$  is a normalization constant,  $k_B$  is the Birks' constant of the scintillator, which in practice is obtained by fitting the formula to the measured data.

### 3.3.3 Liquid Scintillator for SNO+

Organic scintillators can release a large number of photons with wavelengths in the sensitive regions of the PMTs and have abilities for particle identification. In addition, since organic liquids are non-polar media, it is hard for ionic impurities to dissolve in. This leads to the lower contamination levels of uranium (U), thorium (Th), and potassium (K) in the organic liquid scintillators. Among the organic scintillators, aromatic organic liquid scintillators have high electron densities which can provide sufficient targets for particle interactions[106]. Due to these advantages, aromatic organic liquid scintillators have been extensively developed as detection media for large particle detectors, especially for neutrino experiments, such as KamLAND, Borexino, Day Bay, and JUNO[104].

SNO+ has developed such kind of liquid scintillators that are compatible with the detector components, especially with the acrylic materials, such as the AV sphere. Two kinds of SNO+ liquid scintillators are discussed in the following sub-sections: the unloaded liquid scintillator for the scintillator phase and the Tellurium-loaded liquid scintillator (TeLS) for the tellurium phase.

#### Unloaded Liquid Scintillator

SNO+ adopts a scintillator cocktail contains two primary components: linear alkylbenzene (LAB) as solvent and 2,5-diphenyloxazole (PPO) as solute. For per liter LAB, 2 grams of PPO is dissolved. Fig. 3.3 shows the chemical structural formulae of LAB and PPO[104].

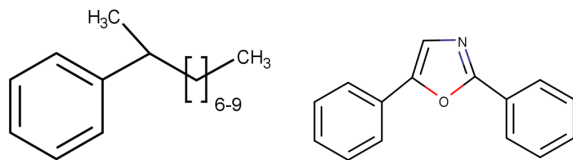


Figure 3.3: Structural formulae of LAB (left) and PPO (right).

LAB is a family of alkylated aromatic organic compounds with a phenyl group attached to a long carbon chain varying from 9 to 14 carbons[107, 104]. It has been used as a biodegradable detergent since the 1960s and it is proved to be relatively non-toxic and very low risks for the environment or human health[107].

LAB is an effective energy absorber.

good optical transparency

flash point at 140  $^{\circ}\text{C}$

The LAB is provided by CEPSA Química Bécancour Inc.

The advantages of LAB are:

- It has very low levels of natural radioactive contaminants such as U, Th and K. The target background levels for the SNO+ LAB are expected to be  $\mathcal{O}(10^{-17})$  gram of  $^{238}\text{U}$  in per gram LAB ( $\text{g}^{238}\text{U}/\text{gLAB}$ ), which is equal to be thousands of events per year; The  $^{232}\text{Th}$  and  $^{40}\text{K}$  levels are  $\mathcal{O}(10^{-17})$  g/gLAB, which is equal to be hundreds of events per year[108].
- High light yield and attenuation length.
- It has fast timing response different timing spectrum for  $\alpha$  and  $\beta$  events, which enables an  $\alpha/\beta$  discrimination.
- High flash point and low toxicity for lab safety.
- appropriate density for mechanical stability
- Good stability and chemically compatible with detector materials, mainly the AV.

- Low cost.

As a wavelength shifter, PPO is usually added and dissolved into the LAB [109]. This wavelength shifter is used as a fluor energies are transferred from LAB to PPO via non-radiative Förster resonant energy transfer it can shift the wavelengths of the scintillation photons to a range of 300-550 nm, which is the

sensitive range of the PMT detection. A 2 g/L PPO concentration in LAB is optimized by SNO+[89]. The absolute light yield of the LAB-PPO liquid scintillator has been well-measured from large particle physics experiments [110], borexino], as well as bench-top measurements [110], novikov, tanner]. The absolute light yield of the LAB+2g/L PPO liquid scintillator determined by SNO+ is 11900 photons/MeV [cite lightyield].

Fig. 3.4 shows absorption lengths.

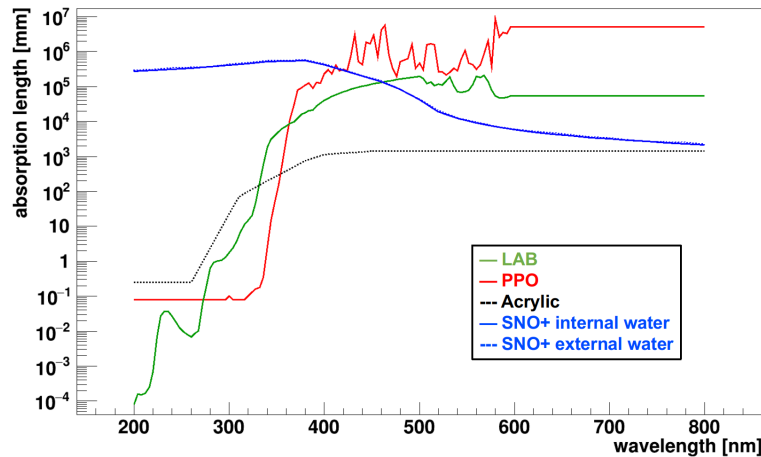


Figure 3.4: Absorption length of SNO+ optical components. ;the internal (solid blue line) and external water (dashed blue line) absorption curves are based on the measurements of the laserball scans in July 2018 during the SNO+ water phase. The horizontal lines are due to absence of the measurements and they are conservative assumptions.

non-radiative transfer from LAB (solvent) to PPO (fluor)

the non-radiative transfer efficiency for 2g/L PPO in LAB is measured as  $78.2 \pm 1.5\%$   
the transfer efficiencies

This transfer efficiency ( $\epsilon_{transfer}$ ) increases as the PPO concentration increasing, as shown in the Table. Above the 2 g/L concentration, the light yield reaches a plateau [104].

### 3.3.3[104].

concentration (g/L)	$\epsilon_{transfer}(\%)$
4	$86.0 \pm 0.8$
2	$78.2 \pm 1.5$
1	$67.7 \pm 2.3$
0.5	$59.3 \pm 3.2$
0.25	$48.7 \pm 5.0$

## Tellurium-loaded Liquid Scintillator

To load the Te into the liquid scintillator, a compound is made by condensation reactions between telluric acid (TeA) and 1,2-butanediol (BD), with N, N-dimethyldodecylamine (DDA) being used as a stabilization agent.

A tertiary amine (N, N-Dimethyldodecylamine, DDA) was added during the reaction to stabilize TeBD complexes and avoid any phase separation.

Tellurium-loaded 65% of the pure, unloaded scintillator  
water-based wavelength shifter  
timing profile, the intensity of scintillation light as a function of time  
the prompt fluorescence intensity at a time  $t$  excitation be  $I = I_0 e^{-\frac{t}{\tau}}$   
singlet and triplet states ionization density depend  $\alpha$ -particle high ionization density  
quenching,

2 g/L PPO gives an absolute light yield of 11900 photons/MeV.  
for the partial-fill phase, 0.5 g/L PPO gives Measurements in 0.5 g/L showed a light yield of 52% of 2 g/L, 6190 photons/MeV[111, 112].

To meet the low background requirement of the  $0\nu\beta\beta$  analysis, the purity of the TeLS cocktail is aimed to  $\mathcal{O}(10^{-15})$  g/g level for U and Th.

## 3.4 Optics

Optical parameters

Winston cone

timing

attenuation

scattering

laser pulse diffuser, it can run with different wavelengths: 337, 365, 385, 420, 450, and 500 nm. The laserball

The acrylic of the AV is UV-transparent

## 3.5 Electronics

In this section, the SNO+ electronics system is introduced. The system includes the trigger and readout systems. As mentioned in ??, the PMTs as photon sensors are the basic detection elements for the SNO+ detector. The signals from the PMTs are sent to the SNO+ electronics system, which records the PMT time and charges information and then transfers the digitized data to offsite computing systems for data analysis. These steps are detailed in the following.

The photons created from particle interactions in the detector propagate to the PMT sphere and may hit a certain PMT and strike on its photo-cathode, which is a thin cesium bialkali film coated on the inner surface of PMT glass. The photocathode then produces a photo-electron (p.e.) through a photoelectric effect. The photocathode is set at ground voltage while the anode is at a high voltage ranging from +1700 to +2100 V [113, 102]. This forms electric fields inside the PMT. The p.e. is accelerated and focused by the electric field in the PMT and goes through the volume which is under vacuum until it reaches the region of a series of secondary emission electrodes, called dynodes. The nine dynode strings are constructed in a Venetian blind configuration in R1408 PMT [113, 99]. When the p.e. transfers its energy to the materials in dynodes, a number of secondary electrons escape

and form a measurable current which is collected by a custom-made operating circuit (PMT base) at the anode[114].

The anode pulse produced from the PMT travels along 35 m-long RG59/U type coaxial cable (with a resistance of  $75 \Omega$ ) to the front-end electronics which are set up on the deck above the detector. The coaxial cable also carries the high-voltage[113].

To tackle more than 9000 PMTs in the SNO+ detector, the coaxial cables connected to each PMTs are grouped into bundles. Each bundle with 8 PMTs is connected to a Paddle Card. Four Paddle Cards are linked to a PMT Interface Card (PMTIC). The PMTIC supplies high voltages and receives signals of up to 32 channels. Each channel for one PMT. 32 channels in PMTIC are plugged into a Front End Card (FEC) that processes, digitizes, and stores PMT signals. Each FEC has 4 Daughter Boards (DB) and each DB handles 8 channels. 16 PMTICs and FECs are inserted in one electronic crate and thus each crate processes 512 PMTs. 19 crates tackle 9728 PMT channels in total, of which 32 channels are reserved for calibration inputs and labeled as FEC Diagnose (FECD) channels. The triggered PMTs can be labeled by the logical channel number (*lcn*) using the map of the PMT to the crates and cards[5, 88]:

$$lcn = 512 \times \text{crate} + 32 \times \text{FEC} + \text{channel} \quad (3.1)$$

To properly process and record information from PMTs, each DB tackling with 8 channels has three types of custom-made integrated circuits to implement three functions[113, 115, 5]:

- Two four-channel discriminators (SNOD) chips set thresholds for PMT signals.
- Eight single-channel CMOS chips record the time when the PMT pulse crosses the discriminator thresholds.
- Two eight-channel charge integrator (SNOINT) chips integrate the PMT pulses over a time interval to obtain PMT charge information. There are three different time windows for the integral, resulting in three types of charge values: QHS(Charge High

gain Short integration time), by integrating the pulse over 60 ns; QHL (Charge High gain Long integration time), by integrating the pulse over 400 ns; and the QLX (Charge Low gain), by integrating the low gain PMTs over either 60 or 400 ns.

First, the discriminator checks the input pulses from a PMT channel with the predefined threshold voltages. If the PMT pulse crosses the channel threshold, a discrete square trigger pulse is generated. The trigger pulse has different time widths for different trigger types, including a 93 ns long square pulse (N100) and a 48 ns square pulse (N20)[116]. These time widths are optimized for the timing of the photon propagation in the detector and later to determine the number of hit PMTs in a specific time window. Besides these two, there are also two triggers that copies the analog pulses of high and low gain of each hit PMTs, known as ESUMHi(gh) and ESUMLo(w). These triggers mainly measure the stability of the detector, in case that there would be large signals in the PMTs while the number of the hit PMTs are small due to one or a few PMTs being exposed to a high amount of light or experiencing break downs[117]. At the same time, CMOS chips produce a time-to-amplitude (TAC) voltage and the TAC starts to ramp. The SNOINT starts to integrate all pulses from the PMT channel from 10 ns before the threshold crossing time to 390 ns or 50 ns to get QHL, QHS, or QLX values mentioned before[113, 88].

The trigger pulses from all the channels in one crate with 16 FECs are sent to a Crate Trigger Card (CTC) and are summed up. For 19 crates, 19 CTCs are connected to 7 Master Trigger Cards/Analogue (MTC/A+) (“+” refers to SNO+’s upgrading from the SNO), which are installed in an individual rack. It takes about 110 ns for the signals to travel to the MTC/A+. The MTC/A+ sums the trigger pulses from all crates and checks whether the sum is above the trigger threshold. Then the summed trigger pulse is sent to the digital master trigger system (MTC/D) which checks 7 MTC/A+ triggers. As mentioned in the previous paragraph, the summed triggers of N100 and N20 indicate the number of hit PMTs within the pulse time widths. In the MTC/A+ discriminators, there are three different threshold values of the number of the hit PMTs for the summed trigger pulses: Lo(w), Med(ium), and Hi(gh). During the water phase, N100Lo, N100Med, N100Hi are

set based on the N100 pulses, where each has a different threshold value set. from lower value to higher value (for example, a setting of N100Lo=11, N100Med=16, N100Hi=21 was used in the water phase simulations). A lower threshold can increase the data-taking rates by including more signals as well as background noise. A high event rate can also make the detector unstable. On the other hand, a higher threshold removes more noises with a sacrifice of signals. The MTC/D checks the trigger type with the pre-defined trigger mask (a set of multiple trigger types with different trigger thresholds can be set), if it is satisfied, a Global Trigger (GT) is issued[5, 88, 118].

Once the GT is issued, an event is triggered and the MTCD sends the GT to the FEC which ramps the TAC within the next 20 ns (determined by a 50 MHz clock mentioned later). This takes another 110 ns. Thus there is a total delay of 220 ns after the FEC ramping the TAC. When the TAC ramps, a time gate of 400 ns is set for waiting the GT. If there is a GT in this 400 ns window, the TAC is stopped and the resultant voltage is digitized and recorded as the PMT hit time. If there is no GT, the TAC resets and the PMT hit is not recorded. Meanwhile, for the square trigger pulses from each PMT channel, if they are within the 400 ns gate and before the GT arrives, they will be recorded as the hits of an event. The recorded number of the hit PMTs for a given event is referred to as NHits. The charge information of the event is also recorded[88, 118].

A 10 MHz and a 50 MHz clocks are used to record the time of the triggered event. The universal time of the triggered event is calculated as the time elapsed from a predefined  $T_{zero}$ , the midnight of January 1, 2010 (GMT) to the moment when the event happensA 10 MHz clock used for counting the absolute time started at  $T_{zero}$ . It has a 53 bit register and can run for 28.5 years. Its accuracy is maintained by a GPS system. The 50 MHz clock gives more accurate timing. It limits the best time resolution of the GT to 20 ns. This clock has a 43 bit register and rolls over every 2.04 days. The relative time between the events can be used for analyzing specific physics processes, such as radioactive decays[118, 88].

The recorded hit information of the triggered event, including the values of the TAC, QHS, QHL, QLX (i.e., the time and charge information of hit PMTs of the event), and

the trigger settings are sent to a Crate Controller Card (XL3) in each crate. These cards were installed for SNO+ to handle higher data transfer rates compared to SNO, with a max rate of 14 MB/s, which is equivalent to approximately 2 million hits per second[115]. They read out the recorded data and wrap them as ethernet packets and send them to the Data Acquisition System (DAQ) and Event Builder system[119]. The Event Builder system writes information into event records based on their GT identification number (GTID) and saves them on storage disk[5]. These raw data are written in the ZEBRA data bank (ZDAB) format and they are further processed into ROOT format by high-performance computing clusters.

As a summary, the SNO+ electronic system can measure signals with a nanosecond-level timing resolution and a single-photon level charge resolution. It can handle an event rate of several kHz and even much higher rates for cases such as the burst events from a galactic supernova[5].

### 3.6 Calibration

Two kinds of calibration sources are used by SNO+: optical sources and radioactive sources. The optical sources are used to calibrate the PMT response and to measure the optical properties of the detector media

Radioactive source: energy scale, resolution, systematic uncertainties  
reconstruction performances and uncertainties. particle identifications

Calibration sources with known physics parameters: help to understand the detector response to the events and to make accurate measurements

the SNO+ Source Manipulator System (SMS) is inherited from the SNO.

An Umbilical Retrieval Mechanism (URM) is used to send the source down to the inner vessel.

The sources are connected to the umbilical.

An umbilical encloses electrical cables, optical fibers, and gas lines connected to the source.

A Universal Interface (UI) connecting the URM and the detector. Therefore, a sealed environment, which ensures radon gas not leaking into the detector when deploying the source.

The source manipulator system (see Section 6.3) allows the insertion of various types of calibration devices inside the acrylic vessel.

### 3.6.1 The $^{16}\text{N}$ Calibration Source

is one of the radioactive sources

This source is inherit from SNO experiment[120, 9, 121],

A deuterium-tritium (DT) generator in SNOLAB can produce neutrons through:  $D + T \rightarrow n + ^4\text{He}$ , flow  $\text{CO}_2$  gas stream through pipe lines the  $^{16}\text{N}$  isotopes are created by the process:  $n + ^{16}\text{O} \rightarrow ^{16}\text{N} + p$ ,

The  $^{16}\text{N}$  isotope mainly decays through  $\beta$ -decay process:  $^{16}\text{N} \rightarrow ^{16}\text{O} + e^- + \bar{\nu}_e$ . It has a 66.2% chance to emit an electron with end-point energy of 4.29 MeV and a 22.8% chance to 10.42 MeV

[122]

a simplified decay scheme is shown in Fig. 3.5.

6.13 MeV  $\gamma$  rays.

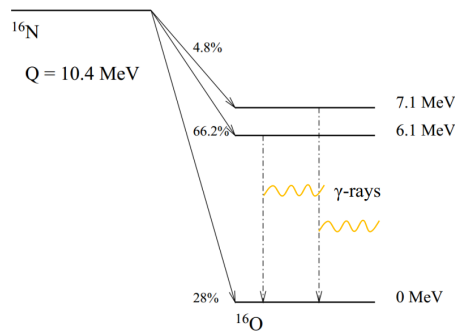


Figure 3.5:  $^{16}\text{N}$  main decay scheme, modified from [9].

Fig. 3.6 shows the geometry of the  $^{16}\text{N}$  source chamber. The chamber is a stainless steel cylinder mainly containing a small PMT and a gas decay chamber. The chamber

was designed to confine the electrons from  $^{16}\text{N}$  decay within the chamber and let them be detected by the PMT inside;

to ensure a high fraction of the  $\gamma$ -rays

lighthouse where the liquid in the scintillator volume (for example, pure water in the water phase) is free to enter.

tagged by a small PMT inside

A polyethelene bumper cone is at the bottom of the source.

gas capillary tube

[120].

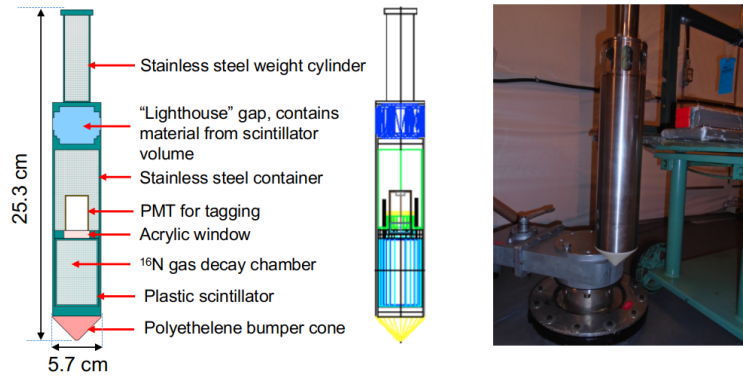


Figure 3.6:  $^{16}\text{N}$  calibration source geometry. Left: a detailed diagram of  $^{16}\text{N}$  source geometry, modified from [10, 11]; middle: source geometry implemented in RAT, modified from [12]; right: a picture of the  $^{16}\text{N}$  source, taken from [13].

The  $^{16}\text{N}$  source  $^3\text{H}(p, \gamma)^4\text{He}$  reaction.

### 3.6.2 The Americium Beryllium (AmBe) Calibration Source

Optical calibration *in-situ*

- Timing module for the Embedded LED Light Injection Entity (TELLIE)

light-emitting diode (LED)

time calibration, time response calibrates the gain and charge response of the PMTs, which is important to estimate the event energy.

a precision of  $\mathcal{O}(1\text{ ns})$

Blinky fiber optics nailed to the PSUP to calibrate stuff.

AMELLIE optical attenuation in the detector over time

SMELLIE scattering of the detector media

- 
- 

### 3.6.3 The Laserball

optical source, named as laserball, is a light diffusing sphere, which nitrogen dye laser glass bubbles.

fast pulsing LED or lasers measures optical properties, such as scattering, attenuation of the detector materials, the response of PMTs, angular and wavelength dependent wavelength dependent absorption and the optical degradation

In the scintillator and tellurium phases, three additional  $\gamma$  sources:  $^{48}\text{Sc}$ ,  $^{137}\text{Cs}$  and  $^{57}\text{Co}$  will be implemented.

$^{46}\text{Sc}$  source

## 3.7 Detector Backgrounds

### 3.7.1 Physics Backgrounds

Radioactive Isotopes

assays

in-situ ex-situ

the instrumental backgrounds can be removed by the data-cleaning approaches.

### 3.7.2 Instrumental Backgrounds

## 3.8 Monte Carlo Simulation and the RAT Software

The SNO+ collaboration has developed a software framework, called the Reactor Analysis Tool (RAT), which integrates a Monte Carlo simulation of the SNO+ detector and event-based analysis tools (for online and offline event analysis) since the beginning of the program. This software was originally developed by Stan Seibert for Braidwood Collaboration for a generic KamLAND like detector. It is also used by the other astroparticle physics experiments, such as DEAP/CLEAN, CLEAR and potentially for Darkside-50[123].

Geant4 Toolkit and incorporates ROOT libraries for data handling and analysis.

The RAT Monte Carlo was originally developed for the Braidwood Collaboration utilizing software developed for a generic KamLAND-like detector, called Generic Liquid Scintillator GEANT4 simulation (GLG4). It was branched and developed into the specialist SNO+ version, starting in 2006/2007.

GLG4sim

Braidwood

combines both Monte Carlo simulation of the Braidwood detector with event-based analysis tasks, like reconstruction. The primary goals are:

Make it easy to analyze Monte Carlo-generated events as well as data from disk using the same software with only a few command changes. Even in the proposal R&D phase, where there is no real data, this is still useful for dumping Monte Carlo events to disk to be analyzed by another job. When there is real data, being able to do the analysis with the same code path as was used on Monte Carlo is very reassuring. Allow for a modular, user-controlled analysis of events. This includes allowing the user to select which analysis tasks to perform (different fitters, pruning unneeded data from the event data structure, etc.). It should also be relatively straightforward for users to introduce their own code into the analysis process. Separate analysis into small tasks that can be developed asynchronously by different people, yet integrated with minimal (or perhaps zero) pain. Integrate into

existing GEANT4 and GLG4sim efforts with a minimum of code duplication. As much as possible, RAT should be designed to incorporate upgrades of these packages just by relinking. No cut and paste of code (mainly a question with GLG4sim). Design the detailed processes of data acquisition and trigger systems are [89].

The SNO+ version of RAT is being developed by the whole collaboration and evolves with the experiment progress. Besides more functions are added into the RAT, it is also tuned and optimized with the updated parameters from more precise descriptions of the physics processes or the detector responses to the calibration sources. Therefore, different versions of RAT may give different results. For the work in this thesis, multiple RAT versions are used, mainly the versions for the water phase and partial-fill phase. In this case, I will specify the RAT version when I discuss a certain analysis. [124]

# Chapter 4

## Event Reconstruction

### 4.1 An Overview of the Reconstruction Algorithms in SNO+

An event happens in the SNO+ detector can produce Cherenkov or scintillation photons. These photons propagate through the detector and finally are measured by the PMTs.

By utilizing the time and charge information recorded by the PMTs, reconstruction algorithms aim to determine the vertex (position and time), direction and energy of an event. Sets of algorithms have been or being developed for the SNO+ event reconstruction. These algorithms are based on different methods and are optimized for the different SNO+ physics phases. For a certain algorithm, its performances are basically tested by the Monte Carlo simulations as well as the calibration data. Once the algorithm shows proper results and approved by the collaboration, it is implemented into the SNO+ RAT software and process the SNO+ data and simulations.

The event vertex are evaluated by the timing parameter of the photon propagation.

The energy of an event is mainly determined by the number of the triggered PMTs ( $N_{Hits}$ ).

Multi-site or multi-vertex reconstruction algorithm is being developed.

In this chapter, we do not consider the case of multi-vertex.

Muon tracking

The huge amount of data provided by particle detectors make the field of experimental particle physics an ideal place for implementing machine learning. The machine learning algorithms, such as artificial neural network (ANN), have been implemented into the data analysis as well as the event reconstruction in SNO+. In the RAT software, an ANN position reconstruction algorithm (position ANN) has been developed and will be implemented in future. This algorithm trains the neural network from calibration data to find the position of an event.

Once a neural network is trained, Traditional approach can fail to converge [125, 126].

using calibrated hit time and angle between PMTs and an estimated event orientation as inputs to find a radius.

## 4.2 Multi-path Reconstruction Algorithm for SNO+

A Multi-path (MP) reconstruction framework was developed by the University of Alberta group as an additional vertex reconstruction algorithm for SNO+.

In this framework, the fitter is able to be adapted for various SNO+ physics phases, including the water phase, the conceptual wavelength shifter (WLS) phase, the partial-fill phase and the scintillator phase (with and without loading tellurium). In the SNO+ water phase, the cavity and the AV are both filled with ultra-pure water. This is a relatively simple geometry since everything inside the PSUP can be simplified as water. Therefore, we start with the MP water fitter (the MPW fitter) to explain the reconstruction concepts.

The MPW fitter fits for position, time and direction of a triggered event in SNO+ water phase. First, the fitter throws a random position built up by random variables which are uniformly distributed inside a sphere with a radius of 10 *meters* (larger than the actual PSUP radius  $r_{PSUP} = 8.39\text{ m}$ ). Meanwhile, a random event time is also generated, following a uniform distribution in a range of 100 to 300 *ns*. The Class Library for High Energy Physics (CLHEP) is used for creating pseudo-random numbers (see the Appendix A.1 for details). The random position and the random time are combined to form a random

event vertex, which is set as the trial event vertex.

For a triggered event, photons are produced around the event position and propagate to the PMTs. In a simplified situation neglecting reflection and refraction, these photons propagate along straight line. Connecting the trial event vertex to the triggered PMTs, the fitter evaluates a timing parameter, called the time residual ( $t_{res}$ ), which is defined as:

$$t_{res} = t_{PMT} - t_{transit} - t_{event}, \quad (4.1)$$

where  $t_{PMT}$  is the PMT trigger time recorded by the detector,  $t_{event}$  is the time when an event occurs (event time), and  $t_{transit}$  is the total transit time (or time of flight,  $TOF$ ) taken by a photon travelling from the event position ( $\vec{x}_{event}$ ) to the triggered PMT ( $\vec{x}_{PMT}$ ) and crossing different materials in the detector.

To calculate the  $t_{transit}$ , the fitter uses photons from prompt time window (prompt light) and assumes that photons propagate in straight lines (straight light paths). The simple straight light path calculation gives  $t_{transit} = |\vec{x}_{event} - \vec{x}_{PMT}|/v_{water}$ . Detailed calculations, such as refraction and reflection when the lights cross different detector materials, absorption and scattering from the materials, as well as the lensing effects caused by the spherical structure of the acrylic vessel, are neglected. We found that without these details, the fitter can still produce decent results that are consistent with the ones using detailed calculations.

For a trial vertex ( $\vec{x}_0, t_0$ ), the fitter calculates a set of  $t_{res}$  values with respect to all the triggered PMTs. These values are fed into a likelihood function:

$$\ln \mathcal{L}(\vec{x}_0, t_0) = \sum_{i=1}^{N_{hits}} \ln P(t_{res}^i), \quad (4.2)$$

where  $t_{res}^i$  is the time residual calculated from the  $i^{th}$  triggered PMT and  $N_{hits}$  here stands for the number of total triggered PMTs by an event.

A pre-set 1-dimensional (1D) probability density function (PDF) is used for fitting the model. The pdf was taken from the bench-top timing profile measurement as well as the measured detector response.

$P(t_{res}^i)$  is the probability returned from the PDF for the  $i^{th}$  triggered PMT and a trial event vertex.

The Levenberg-Marquardt method, which is commonly used for fitting the nonlinear model for multiple parameters, is used as an optimizer to find the best fit event parameters (position, time and direction). Appendix A.2 describes this method; A.3 describes the implementation of the method to the MultiPath fitter framework. Also see [127, 1].

As we will see in the following sections, one of the main tasks for the fitter is to calculate the  $t_{transit}$  by evaluating light paths. In the water phase, we consider photons created in an event travelling along straight line paths and the paths are always in water. In the other situations, for example, when the acrylic vessel is filled with the wavelength shifter or scintillator, the light path calculations will be modified.

Fig. 4.1 shows the reconstruction concepts for position and direction.

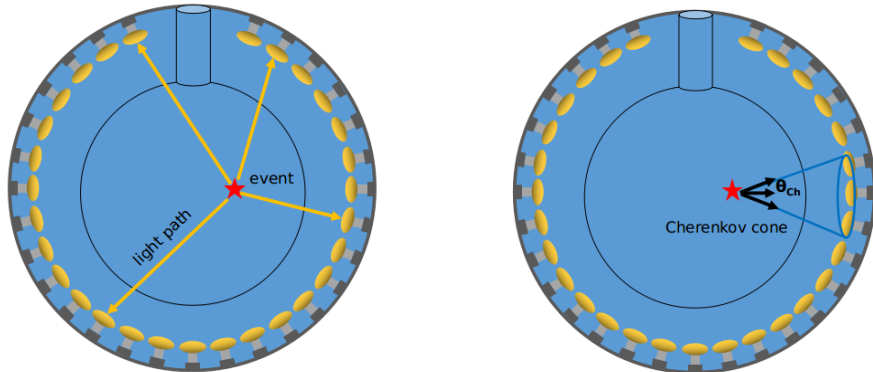


Figure 4.1: Diagrams of position (left) and direction (right) reconstruction in SNO+ water phase.

### 4.3 Multi-path Position and Direction Reconstructions for the Water Phase

#### 4.3.1 Vertex Reconstruction

For the position reconstruction of the MPW fitter, the likelihood function simply calculates the likelihood assuming straight line paths of prompt light from a position vertex  $\vec{X}_0$  (fVertex) and a starting time offset  $t_0$  to each of the hit PMTs.

We define the position difference  $\vec{X}_{\text{diffCh}} = \vec{X}_0 - \vec{X}_{\text{pmt}}$ , then the time of flight for prompt light is  $t_{\text{Ch}} = |\vec{X}_{\text{diffCh}}|/v_g$  and  $L_{\text{Ch}} = L(t_{\text{Ch}})$ .

The derivatives of the likelihood function can be calculated from explicit mathematical forms as:

$$\frac{\partial L}{\partial t_0} = \frac{dL_{\text{Ch}}}{dt_{\text{Ch}}},$$

$$\frac{\partial L}{\partial x} = \frac{\partial L_{\text{Ch}}}{\partial t_{\text{Ch}}} \frac{dt_{\text{Ch}}}{\partial x} = -\frac{dL_{\text{Ch}}}{dt_{\text{Ch}}} \frac{X_{\text{diffCh}}}{|\vec{X}_{\text{diffCh}}| \cdot v_g},$$

$$\frac{\partial L}{\partial y} = -\frac{dL_{\text{Ch}}}{dt_{\text{Ch}}} \frac{Y_{\text{diffCh}}}{|\vec{X}_{\text{diffCh}}| \cdot v_g},$$

$$\frac{\partial L}{\partial z} = -\frac{dL_{\text{Ch}}}{dt_{\text{Ch}}} \frac{Z_{\text{diffCh}}}{|\vec{X}_{\text{diffCh}}| \cdot v_g},$$

where  $\frac{dL_{\text{Ch}}}{dt_{\text{Ch}}}$  can be calculated numerically from the timing pdf.

In the WaterPosition class, it starts with a random  $(\vec{x}_0, t_0)$  as seed and calculates the likelihoods and their derivatives for various paths. These values are sent to the Multi-path Fitter, which is fitting 4 parameters:  $x, y, z, t$  and to maximize the likelihood function through the MRQ method and to find the best-fit positions.

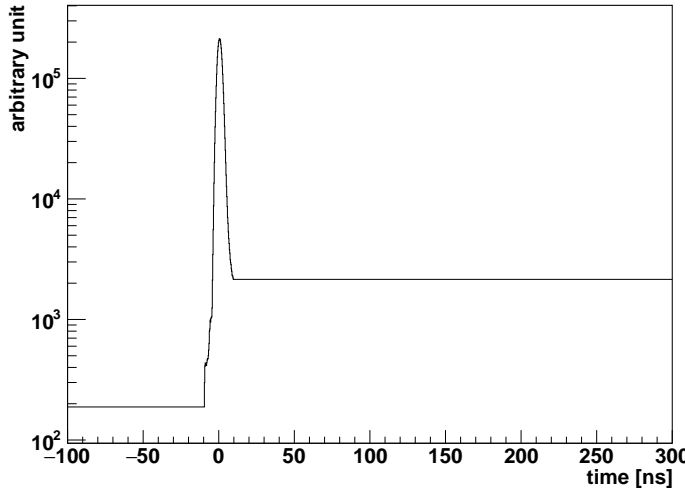


Figure 4.2: PMT response time as the timing pdf for vertex reconstruction.

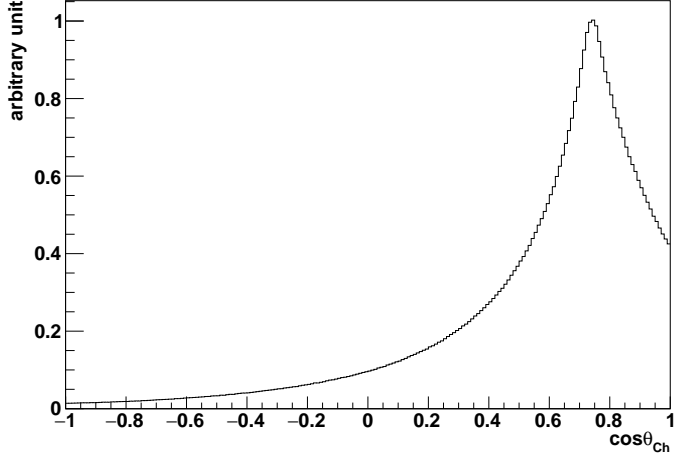


Figure 4.3: PMT angular distribution as the angular response pdf for direction reconstruction.

### 4.3.2 Direction Reconstruction

$\vec{u}_0 = (\cos \phi \sin \theta, \sin \phi \sin \theta, \cos \theta)$  (fDirection), where the  $\theta$  is zenith angle and  $\phi$  the azimuth.  $\cos \theta_{\text{Ch}}$  is the angle between  $\vec{u}_0$  and  $\vec{X}_{\text{diffCh}}$ , which is taken as the fitting parameter of the likelihood function for the direction reconstruction. For the i-th hit PMT,  $\cos \theta_{\text{Ch}}^i = \vec{u}_0 \cdot \frac{\vec{X}_{\text{diffCh}}^i}{|\vec{X}_{\text{diffCh}}^i|}$ , then the likelihood function is:

$$L(\vec{u}_0) = \sum_{i=1}^{\text{Nhits}} L_i(\cos \theta_{\text{Ch}}^i),$$

The derivatives have explicit mathematical forms:

$$\frac{\partial L}{\partial \theta} = \frac{dL_{\text{Ch}}}{d \cos \theta_{\text{Ch}}} \frac{d \cos \theta_{\text{Ch}}}{d \theta} = \frac{dL_{\text{Ch}}}{d \cos \theta_{\text{Ch}}} \frac{d \vec{u}_0}{d \theta} \cdot \frac{\vec{X}_{\text{diffCh}}}{|\vec{X}_{\text{diffCh}}|},$$

where  $d \vec{u}_0 / d \theta = (\cos \phi \cos \theta, \sin \phi \cos \theta, -\sin \theta)$  and

$$\frac{\partial L}{\partial \phi} = \frac{dL_{\text{Ch}}}{d \cos \theta_{\text{Ch}}} \frac{d \cos \theta_{\text{Ch}}}{d \phi} = \frac{dL_{\text{Ch}}}{d \cos \theta_{\text{Ch}}} \frac{d \vec{u}_0}{d \phi} \cdot \frac{\vec{X}_{\text{diffCh}}}{|\vec{X}_{\text{diffCh}}|},$$

where  $d \vec{u}_0 / d \phi = (-\sin \phi \sin \theta, \cos \phi \sin \theta, 0)$ .  $\frac{dL_{\text{Ch}}}{d \cos \theta_{\text{Ch}}}$  can be calculated numerically from the PMT angular response pdf.

In the FitterWaterDirection class, it starts with a random  $(\theta_0, \phi_0)$  as seed and calculates the likelihoods and their derivatives for various paths. These values are sent to the Multi-

path Fitter, which is now fitting 2 parameters:  $(\theta, \phi)$  and to maximize the likelihood function through the MRQ method and to find the best-fit directions.

### 4.3.3 Effective Group Velocity

When photons travel through the detector, their group velocities change with different refractive indices of different detector materials. The group velocities also depend on the wavelengths of the photons as  $v_g = c/n(\lambda)$ . Fig .4.4 shows the measured refractive indices as a function of wavelength, obtained from the measurements of laserball scans in the SNO+ water phase[14]. Furthermore, the group velocities can change when these photons are scattered, absorbed, refracted and reflected. To simplify these complicated situations for the reconstruction, an averaged value of the group velocity is used in the straight line light path calculation. This fixed group velocity is considered as an effective value.

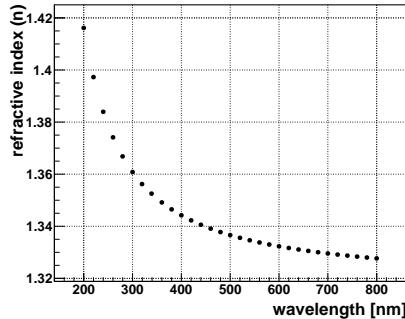


Figure 4.4: Refractive index vs wavelength. These values are based on the measurements from laserball calibration scans in the SNO+ water phase[14].

A reasonable selection of this value is required, since the value can introduce biases in the fitted position. This kind of bias is mainly due to a “complementary” effect of the fitter. As mentioned in section 4.2, the water vertex fitter calculates the  $t_{transit}$  by evaluating the distances from the trial vertex to the triggered PMTs:  $t_{transit} = |\vec{x}_{event} - \vec{x}_{PMT}|/v_{water}$ . If the value of the group velocity  $v_{water}$  is set large (or fast speed), the value of  $t_{transit}$  will decrease, and the corresponding value of  $t_{res}$  will increase according to the definition of  $t_{res}$ (4.1). These calculated  $t_{res}$  value is compared to the time pdf for the fitting. If  $t_{res}$  is

larger than the expected value, the fitter will place the trial vertex away from the hit PMTs to increase the  $t_{transit}$  and then decrease the  $t_{res}$ , as illustrated in Fig. 4.5. On the other hand, if  $v_{water}$  is set small (or slow speed),  $t_{transit}$  increases and  $t_{res}$  decreases, and the fitter will place the trial vertex closer towards the hit PMTs. Therefore, an overestimated group velocity (too fast) brings a positive radial bias to the true event position while an underestimated one (too slow) brings a negative radial bias.

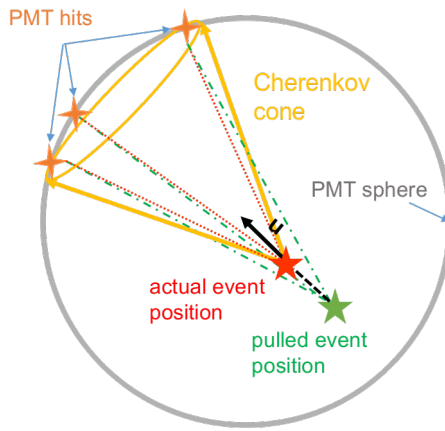


Figure 4.5: A cartoon shows effects of tuning the effective group velocity. In this case, the effective group velocity is faster than expected, the fitted position is dragged back along the direction to increase the time of flight.

In practice, the effective group velocity is tuned by an effective refractive index  $n_{eff}$  (or called *RI* value):  $v_{water} = c/n_{eff}$ . To select a reasonable effective group velocity for the water-phase vertex fitter, my first approach is to test on all the values of the refractive index provided by the SNO+ laserball measurements. The values are listed in Fig. 4.4.

I choose the one which gives the smallest radial bias based on MC simulations. For typical 5 MeV  $e^-$  events simulated uniformly inside the AV and isotropic momentum,

As shown in Fig. ??,  $n_{eff} = 1.40$  gives the smallest radial bias and is adopted for the MC case.

Later I turned to a more data-driven approach rather than just tuning from the simulations. This approach is to extract an average group velocity by analyzing the  $^{16}\text{N}$  calibration source data.

as shown in Fig. 4.6.

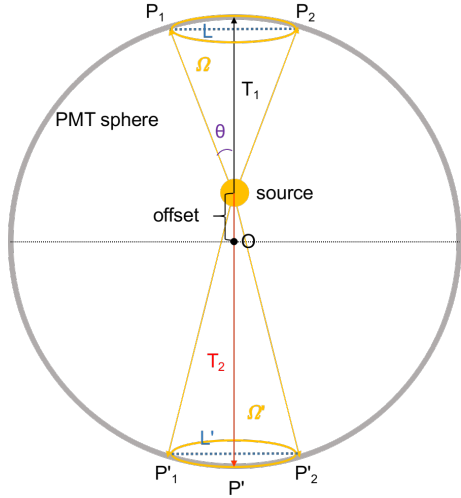


Figure 4.6:  $^{16}\text{N}$  central run.

For a more precise approach, a set of laserball calibration runs which to measure actual group velocities in the SNO+ water detector[128].

For the scintillator and partial-fill phase vertex fitters, I adopt a linear interpolation method described in [129], which will be discussed in section 4.5.

#### 4.3.4 Fitter Pull and Drive Correction

An effect of “fitter pull” in the event vertex reconstruction utilizing the Cherenkov light was observed in the SNO experiment. The distribution of  $(\vec{x}_{fit} - \vec{x}_{mc}) / |\vec{x}_{fit} - \vec{x}_{mc}| \cdot \vec{u}$  shows a large peak at +1, which indicates that the fitted position  $\vec{x}$  is prone to be pulled forward from the true position systematically along the event direction  $\vec{u}$ [16, 15, 129].

In the SNO+ water detection medium (or the SNO heavy water), Cherenkov photons created by an event trigger most of the PMT hits with early timing and these hits are located within the Cherenkov cone; for the same event, there are also a few triggered PMT hits with later timing. These PMT hits can be caused by the scattered or reflected photons and they are located throughout the detector. For a random PMT hit, it is more probable to be placed outside the Cherenkov cone due to the geometry: consider an event happens

at the center of the PSUP, the Cherenkov cone it produced will intersect the PSUP by an area of  $2\pi R_{PSUP}^2(1 - \cos 41^\circ)$ , which occupies about 12% of the total area of the PSUP sphere. Therefore, for a random PMT hit on the PSUP sphere, it has more than 88% of chance to be placed outside the Cherenkov cone.

For these later timing PMT hits, a similar “complementary” effect mentioned in 4.3.3 can also happen. When the fitter fits with  $t_{res}$ , for the large  $t_{res}$  values caused by the later timing hits, it pulls the trial position away from the later timing hits to increase  $t_{transit}$  and decrease  $t_{res}$ , as illustrated in Fig. 4.7. This effect was also explained as “straighten out delayed photons” by the timing fitter in [16]. Furthermore, the major early hits can also cause small  $t_{res}$  values and thus the fitter pulls the trial position closer towards the early hits to decrease  $t_{transit}$  and increase  $t_{res}$ . Recall that the early hits are located on or around the Cherenkov cone, therefore an overall effect of this “fitter pull” is that the fitted position will be pulled along the axis of the Cherenkov cone and towards the PSUP sphere. This pull direction is coincident with the event direction.

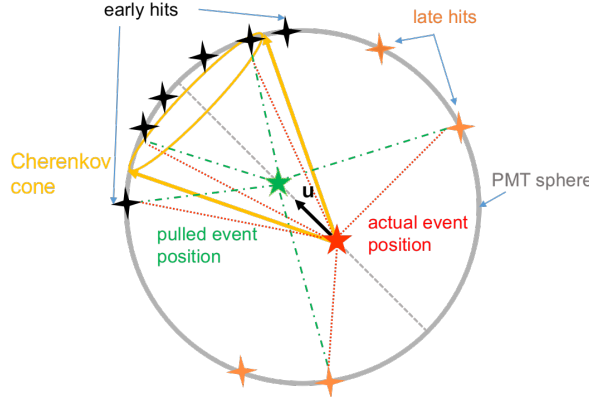


Figure 4.7: A cartoon shows fitter pull effect, modified from Fig. C.2 in [15] and Fig. 2,3,4 in [16].

A simple way to eliminate this “fitter pull” effect is to pull back the fitted event position against the event direction. This is called “drive correction”.

Once the MPW fitter obtains both of the fitted position and direction, the drive correction is applied on the fitted position by  $\vec{X}_{\text{corrected}} = p_0 \vec{X}_{\text{fit}} + p_1 \vec{u}_{\text{fit}}$ , where  $p_0$  and  $p_1$  are

the correction parameters, as shown in Fig. 4.8.

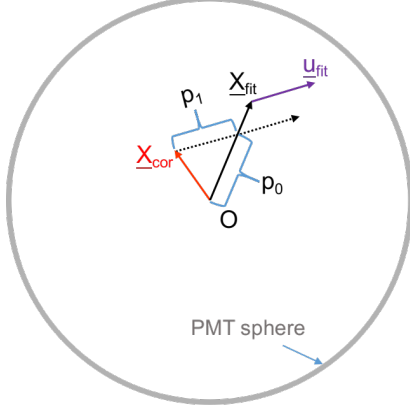


Figure 4.8: A diagram illustrates the drive correction.

To obtain the values of  $p_0$  and  $p_1$ , I generated electron events distributed isotropically inside the AV. The simulations of 2, 3, 4, ..., 10 MeV electrons are produced. Then the MPW fitter is applied on each simulations and returns the results of  $\vec{X}_{fit}$  and  $\vec{u}_{fit}$ . Take the Monte Carlo generated positions  $\vec{X}_{MC}$  as the true positions, for all the fitted events, a  $\chi^2$  function is calculated by:

$$\chi^2 = \sum_{i=1}^{N_{\text{events}}} [\vec{X}_{MC}^i - (p_0 \vec{X}_{fit}^i + p_1 \vec{u}_{fit}^i)]^2$$

The  $p_0$  and  $p_1$  are obtained by minimizing the  $\chi^2$  function. When calculating the  $\chi^2$ , the fitted events of  $|\vec{X}_{fit} - \vec{X}_{MC}| > 3 \text{ m}$  are thrown away to improve the  $\chi^2$  minimization results.

For the 2 to 10 MeV electrons simulations, the obtained values of  $p_0$  and  $p_1$  are energy or Nhit dependent. However, it does not improve the results if using the Nhit dependent functions  $p_0(Nhit)$  and  $p_1(Nhit)$  as drive corrections. Finally we take the average values from the 5 to 10 MeV electrons simulations and the drive correction is set as  $\vec{X}_{\text{corrected}} = 0.995765 \vec{X}_{fit} + -63.826 \vec{u}_{fit}$ .

It is important to note that since the drive correction parameters are obtained from the reconstructions of Monte Carlo, it depends on the Monte Carlo and the results of reconstruction. Therefore, the  $n_{water}$ , mode cut and time residue cut affecting the fitted

results will also affect the drive correction parameters, but not significantly.

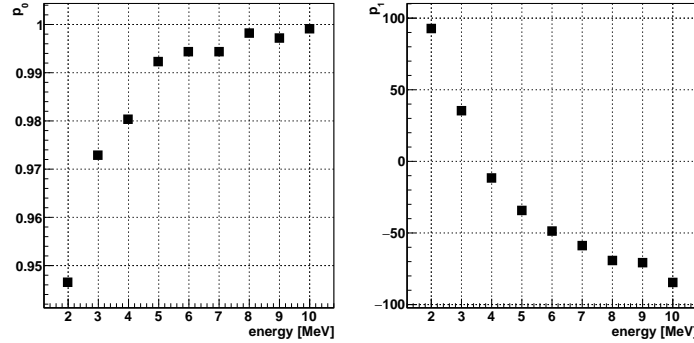


Figure 4.9: Drive correction parameter  $p_0$ ,  $p_1$  vs energy.

Electron events with various energies were generated at the detector center and their momentum were along +x direction.

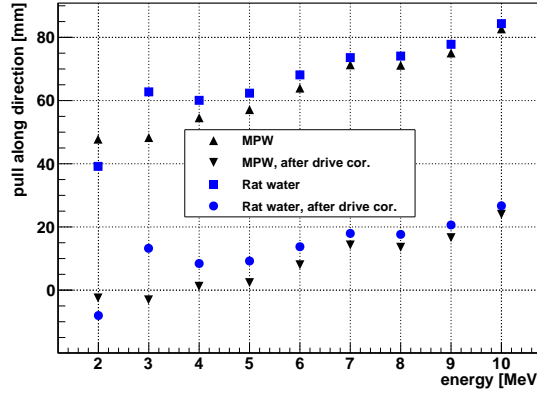


Figure 4.10: Radial biases of simulated electron events before and after the drive correction, as a function of energy.

By fitting the simulations of 5 MeV electrons generated at the detector center and travelling along +x direction, the drive effect of the MPW fitter causes a  $\sim$ 50 mm biases from the detector center along +x axis. The drive correction reduces this drive bias down to  $\sim$ 0.2 mm. For the reconstruction of  $^{16}\text{N}$  data, the drive correction can reduce the fitted position RMS by  $\sim$ 20 mm.

### 4.3.5 Multi-path Fitter Structure

The Multi-path fitter has already been implemented into the RAT software and being used in data processing and analyzing.

The MP fitter structure consists of:

- Fitter database

This database provides parameters used by the fitter, including the physics constants, detector geometry parameters, fit parameters and pdfs. The database is in a JSON format[130] and contains multiple tables tagged by indices to indicate different detection media or physics phases. In each table, there are fit parameters and pdfs optimized for the specific scintillator. For example, for the partial-fill phase with a PPO concentration of 0.5 g/L, the fitter will look for the index of “labppo\_0p5\_scintillator” and extract the pdfs and fit parameters under that index.

The fit parameters includes the fitter tolerance and the maximum iterations which determine how the fitter converges,

Reflective index (water\_RI, or  $n_{water}$ ), used for effective group velocity ( $v_g = c/n_{water}$ ) calculation. air refractive index (air\_RI), PSUP radius ( $r_{PSUP} = 8390\ mm$ ). Offsets boundary settings

The MPW fitter currently uses one fixed number for  $n_{water}$ , rather than a function of wavelengths. The value of  $n_{water}$  can be tuned to give the lowest biases of the fitted positions to the Monte Carlo and to give the lowest RMS of fitted results as well. But the effect of  $n_{water}$  can also be corrected by the drive correction afterwards. Currently  $n_{water} = 1.38486$  is obtained by analyzing the time of flight from the  $^{16}\text{N}$  central run-100934 data reconstructed by the MPW fitter.

time offset, position offset, radius cut x, fitting bin-width and steps.

- PMT response time (timing) pdf for the position reconstruction, as shown in Fig. 4.2.

The pdf shown in red line is modified from the measured PMT response time distribution from SNO time and the late light response is forced to be de-weighted (black).

The pdf is modified in [-100,-4] ns region to match the time residual spectrum obtained from  $^{16}\text{N}$  central run-100934 (blue).

- PMT angular response pdf for the direction reconstruction, as shown in Fig. 4.3. It is taken from the Monte Carlo simulation of 5 MeV electrons traverse in the AV with one direction.
- Likelihood Calculation Classes, Constructs likelihood functions, calculates likelihoods and their derivatives. For the MPW fitter, there are two classes: WaterPosition for position reconstruction and WaterDirection for direction reconstruction. The WaterPosition class tackles with 4 parameters ( $x,y,z,t$ ) and the WaterDirection class tackles with 2 parameters ( $\theta,\phi$ ).
- Multi-path Fitter

Processes the MPW fitter and finds the best-fit of the likelihood function. It is a general processor and is shared with the fitters using the Multi-path Fitter, including the MPW fitter, air-water (AW) fitter, wavelength-shifter (WLS) fitter and scint-water fitter. It processes a certain fitter by being assigned the fitter name in macro. It processes the fitter event by event: for every triggered event, it first calls PMT selectors (ModeCut or StraightTimeResidualCut) and sends the information of the reduced PMTs to a certain Likelihood Calculation Class for likelihood calculations. The Likelihood Calculation Class sends back the values of likelihoods and their derivatives, so the Multi-path Fitter does not care about how the likelihood functions are constructed and how the likelihoods and derivatives are calculated. Using these values, it constructs an  $n \times n$  Hessian matrix ( $n$  is the number of fitting parameters defined in Likelihood Calculation Class) and uses the Levenberg-Marquardt (MRQ) method to maximize the likelihood and finds the best-fit values. For the MPW, if the likelihood maxima is found 5 times for any position and direction then values are returned as the fitted position and direction. For the MPW case, it calls the ModeCut and fits for the position and time; then it calls the StraightTimeResidualCut and fits for the

directions.

- Dump Likelihood

This is a function inside the Multi-path Fitter. It stores the likelihood surfaces and derivatives with respect to arrays of trial vertices of the interested events which are designated by event GTIDs in the database. From the likelihood surfaces and derivatives of an interested event, people can evaluate the fit performance of that event by checking whether the fitter finds global or local maximum.

- SDecompQRH

This is a fit method class modified from ROOT TDecompQRH class[131]. It is used by the Multi-path fitter to invert the Hessian matrix through QR decomposition method[1]. Compared to ROOT, Solve() for  $Ax=b$  is modified to zero the component of  $x$  for which the diagonal element in  $R$  is small. This allows a Levenberg-Marquardt optimization to continue in many cases when the matrix is singular. For the MPW case, it is used to invert a  $4\times 4$  matrix of the WaterPosition Class while the inversion of  $2\times 2$  matrix of the WaterDirection is calculated directly[132].

- PMT selectors

Detailed descriptions are shown in section 4.6.

## 4.4 Vertex and Direction Reconstruction for the Water-based Wavelength-shifter

X. Dai et al.[133] made a proposal for adding wavelength shifters (WLS) into a water Cherenkov detector like SNO. Compared to the water Cherenkov detector, a water-based wavelength shifter (wbWLS) detector has a higher light yield (about threefold higher than SNO[133]) and thus lowers down the energy threshold and opens opportunity to detect low energy events. At the meantime, it will still keep the directionality from Cherenkov signals compared to a loss of the directionality for the liquid scintillator detector, which

can be used to suppress the backgrounds when analyzing directional signals, such as solar neutrinos. This technology is being studied by future neutrino experiments, such as the Advanced Scintillation Detector Concept (ASDC)[134], WATCHMAN experiment[135] and Jinping experiment[86].

There was a proposal of adding wavelength shifter (WLS) into the SNO+ detector in the middle of the water phase. The specific wavelength shifter we considered is PPO, which is a well-studied ingredient of the liquid scintillator used in the SNO+ scintillator phase and Te-loaded phase. Although this proposal was not adopted due to the experiment schedule, it is still worthwhile for a conceptual study of a SNO+-like detector that uses water-based wavelength shifter (wbWLS) as detection medium.

Figure 4.11 shows the position distributions of triggered PMTs for MC simulated 5 MeV electrons travelling along  $+x$  direction in the AV. The left panel shows the case when the detector is filled with pure water while the right panel is for water plus 0.1 ppm PPO. For the same electrons, the number of triggered PMTs ( $N_{Hit}$ ) in wbWLS is about 2.4 times greater than the pure water one. Although there is extra isotropic light emitted, the Cherenkov ring can still be seen clearly, allowing reconstruction of the directionality.

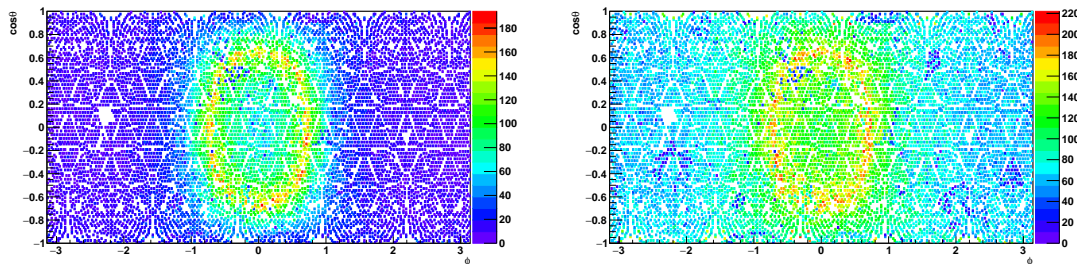


Figure 4.11: Position distributions of triggered PMTs (in zenith and azimuth angles) for 5 MeV electrons travelling along  $+x$  direction in the pure water (left) and the water plus 0.1 ppm PPO (right).

Figure 4.12 shows the energies of simulated electrons as a function of the mean value of the  $N_{Hit}$  distribution (mean nhits). In pure water, a 1 MeV electron simulation does not trigger any PMTs while in wbWLS case we have a mean nhits of 20.

In the wbWLS case, since WLS absorbs and re-emits photons, the reconstruction men-

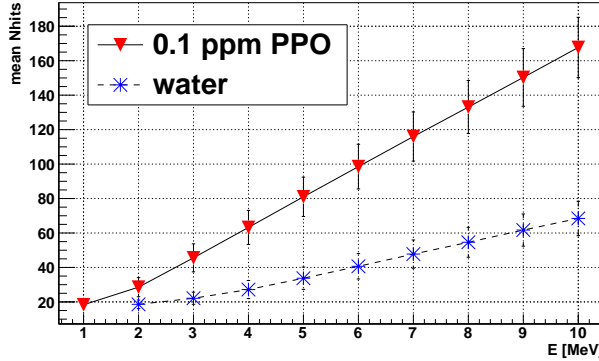


Figure 4.12: The energies of simulated electrons as a function of mean nhits. The values in the 0.1 ppm PPO (solid line with inverted triangle) are compared with the water (dashed line with star).

tioned in section 4.2 is slightly modified to build the MP WLS Fitter. According to the optical property of PPO, the prompt light emitted from an event has a probability of  $\sim 0.6$  to be absorbed by the WLS and then re-emitted at a shifted vertex along the particle direction  $\hat{n}$ . Then the fitter returns a shifted vertex,  $\vec{X}_{0,shifted} = \vec{X}_0 + \text{offset} \cdot \hat{n}$ . The offset we set in the fitter is 100 mm obtained from simulations. Figure 4.13 shows the timing pdf for the wbWLS, which is the PMT response time modified to photon propagation time in the wbWLS.

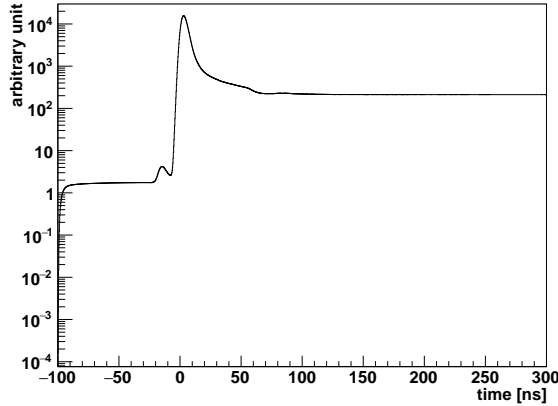


Figure 4.13: The timing pdf for the wbWLS.

To reconstruct the direction, besides the angular distribution of Cherenkov photons,

$\cos \theta_{Ch}$ , we also consider the fraction of the re-emitted and wavelength shifted photons that cause a flat angular distribution.

To test the performance of the MP WLS Fitter, 5 MeV electrons were simulated at the center of the AV filled with wbWLS and travelling along +x direction. As a comparison, the same simulation was done for the AV filled with pure water and the simulated events were reconstructed by the water fitter.

Fig. 4.14 shows the performance of the WLS fitter reconstructed positions of the MC simulations compared to the pure water case. For the fit position distribution of 5 MeV electrons in the wbWLS, we get a root mean square (RMS) of 201 mm and a bias to the center (the mean of histogram) of 29 mm. Compared to the pure water case, the fit bias is about 19 mm better and the RMS is 188 mm better.

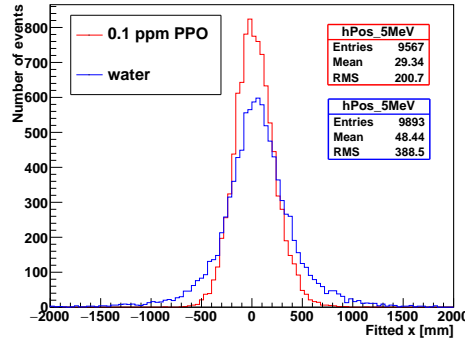


Figure 4.14: Fit position projected on x axis. The WLS fitter reconstructed  $x$  positions of the 5 MeV electron events in the wbWLS (red) are compared to the ones in the water (blue).

For a given Cherenkov event, the error in the reconstructed event direction is defined as[136]:  $\cos(\theta_e) = \vec{u}_{fit} \cdot \vec{u}_e$ , where  $\vec{u}_e$  is the simulated electron direction and  $\vec{u}_{fit}$  is the reconstructed direction. To quantify this error, we define a  $\cos \theta_a$  so that:

$$\frac{\int_{\cos \theta_a}^1 P(\cos \theta_e) d \cos \theta_e}{\int_0^1 P(\cos \theta_e) d \cos \theta_e} = a.$$

where  $P(\cos \theta_e)$  is the distribution of  $\cos \theta_e$  from MC data. The value of  $\cos \theta_a$  is found numerically to let  $\cos \theta_e$  contain  $a \cdot 100\%$  of the reconstructed data. A larger  $\cos \theta_a$  means better direction reconstruction.

Table 4.1 shows the results of  $\cos \theta_a$  for SNO heavy water data[136] and simulations for SNO+ pure water and wbWLS.

Table 4.1: A comparison of quantitative estimates for the angular resolution between the SNO heavy water, SNO+ wbWLS and the SNO+ pure water cases.

medium	$\cos \theta_{0.9}$	$\cos \theta_{0.8}$	$\cos \theta_{0.5}$
SNO heavy water	0.50	0.71	0.92
SNO+ water	0.53	0.76	0.93
wbWLS	0.37	0.63	0.90

Comparing a pure water SNO+ detector and the wbWLS one, using the MP WLS Fitter for physics events gives a better position resolution without a significant loss in the performance of the direction reconstruction.

This fitter was tested for in [137].

## 4.5 Vertex Reconstruction for the Partial-fill and Scintillator Phases

In the partial fill geometry, photons will travel with different speeds as they pass through two different mediums, water and scintillator. Assuming a straight light path, the MP Partial Fitter mainly calculates the total length of the light path ( $|\vec{l}_p| = |\vec{X}_{\text{PMT}} - \vec{X}_0|$ ) and separates the  $|\vec{l}_p|$  into the lengths in scintillator ( $d_{sp}$ ) and in water ( $|\vec{l}_p| - d_{sp}$ ).

In the partial-fill phase, the SNO+ detector can be considered as a geometry composed of the neck (cylinder), AV sphere and water-scintillator interface (plane). A ray connecting a position inside the PSUP to the PMT can intersect with these three geometries. As illustrated in Fig. 4.15, a detailed calculation of  $d_{sp}$  includes evaluations of (1) light path and neck (ray-cylinder) intersection; (2) light path and AV sphere (ray-sphere) intersection and (3) light path and water-scintillator interface (ray-plane) intersection.  $d_{sp}$  is further separated into the path length in the neck ( $d_{sp,neck}$ ) and in the AV ( $d_{sp,AV}$ ).

For a trial position  $\vec{X}_0 = (x_0, y_0, z_0)$  and a triggered PMT position  $\vec{X}_{\text{pmt}} = (x_{\text{pmt}}, y_{\text{pmt}}, z_{\text{pmt}})$ , define a light ray (rather than a line without direction)  $\vec{l}_0 \equiv \vec{X}_0 + a \cdot \vec{u}$ , where  $a$  is the dis-

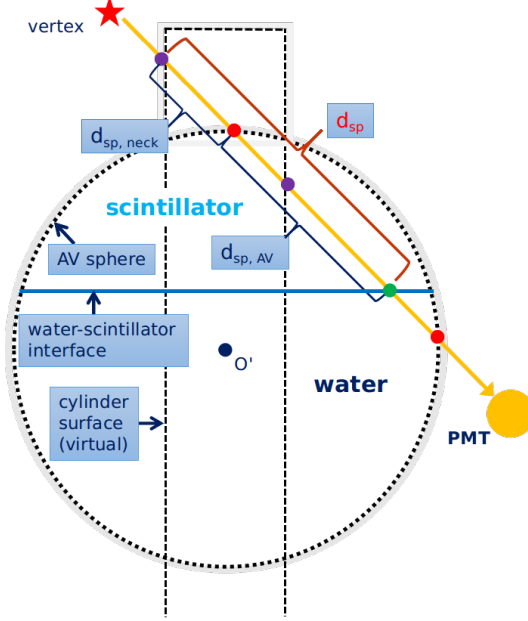


Figure 4.15: Light path calculation for the MP Partial Fitter. The light path intersects with the neck cylinder surface, the AV sphere as well as the water-scintillator interface. The total length of the path in the scintillator region (scintillator path, sp),  $d_{sp}$  is evaluated by intersection calculations.

tance between vertex and intersection point and it is the parameter to be determined;  $\vec{u} = \frac{\vec{X}_{pmt} - \vec{X}_0}{|\vec{X}_{pmt} - \vec{X}_0|}$  is the direction of the light ray. It is a unit vector pointing from the  $\vec{X}_0$  to the  $\vec{X}_{pmt}$ .

In the ray-sphere intersection case (light ray passes through the AV sphere), the intersection points on the  $\vec{l}_0$  satisfy the sphere equation  $(\vec{X} - \vec{O}_{av})^2 = r_{av}^2$ , where  $\vec{O}_{av}$  is the origin of the AV sphere and  $\vec{O}_{av} = (0, 0, 108)$  mm in the PSUP coordinate. Thus the intersection equation is:  $(\vec{l}_0 - \vec{O}_{av})^2 = r_{av}^2$ .

Let  $\Delta \equiv [(\vec{X}_0 - \vec{O}_{av}) \cdot \vec{u}]^2 - (\vec{X}_0 - \vec{O}_{av})^2 + r_{av}^2$ , if  $\Delta > 0$ , solve the equation and get:

$$a_{+,-} = -(\vec{X}_0 - \vec{O}_{av}) \cdot \vec{u} \pm \sqrt{\Delta}, \text{ if } \Delta > 0. \quad (4.3)$$

In this case, both  $a_+$  and  $a_-$  exist and have different values. If  $a_+ > a_- > 0$ , the length of the path inside the sphere is  $a_+ - a_-$ , as illustrated in Fig. 4.16 (a). Due to this geometry, the event position should be outside the AV, the condition  $|\vec{X}_0| \geq r_{AV}$  is automatically met. If  $a_+ > 0 > a_-$ ,  $a_-$  determines the intersection point along the opposite direction

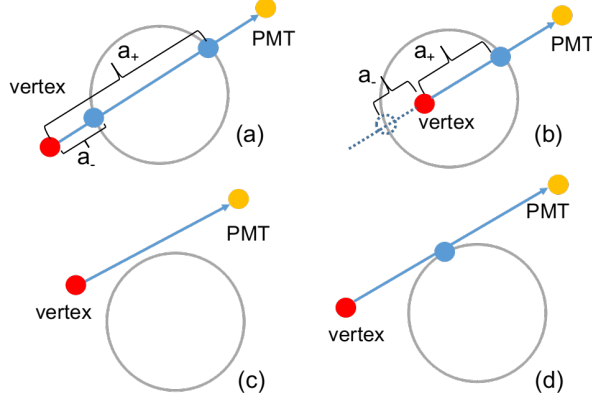


Figure 4.16: Line-sphere intersections. (a): the light ray intersects the sphere with 2 points; (b): the light ray intersects the sphere with 1 point; (c) and (d): the light ray never passes through the sphere.

of the light ray. Thus the light ray actually does not pass that point (different to the line intersection with no direction). Thus the length of the path inside the sphere is  $a_+$ , as illustrated in Fig. 4.16 (b). Also, the condition  $|\vec{X}_0| < r_{AV}$  is automatically met.

If  $\Delta \leq 0$ , there is no intersection point or only one intersection point at the AV, the light ray never passes through the AV sphere, as illustrated in Fig. 4.16 (c) and (d).

For the ray-plane intersection, the z components of the intersection points on  $\vec{l}_0$  satisfy the plane equation  $z = Z_{split}$ , where  $Z_{split}$  is the water level, i.e., the z position of the water-scintillator intersection. Thus the intersection equation is:  $l_{0,z} = Z_{split}$ , where  $l_{0,z} = z_0 + a \cdot u_z$ .

If  $u_z = z_{pmt} - z_0 = 0$ , the ray is parallel to the plane and never intersects the plane.

If  $u_z \neq 0$ , solve the equation, we have:  $a = (Z_{split} - z_0)/u_z = (Z_{split} - z_0)$ . Let:

$$a_3 \equiv a = \frac{(Z_{split} - z_0)|\vec{X}_{pmt} - \vec{X}_0|}{z_{pmt} - z_0} \quad (\text{if } z_{pmt} - z_0 \neq 0).$$

Similar to the case of ray-sphere intersection, if  $a_3 < 0$ , the ray-plane intersection point is on the extended line along the opposite direction to the ray;  $a_3 \geq 0$  ensures the ray hits the interface. Note that here we consider the plane is infinitely large. Later we will combine with the calculations of the other geometries to cut it off.

For the ray-cylinder intersection, the x and y components of the intersection points on

the  $\vec{l}_0$  satisfy the intersection equation:  $l_{0,x}^2 + l_{0,y}^2 = r_{neck}^2$ , where  $r_{neck}$  is the radius of the neck cylinder ( $r_{neck} = 785\text{ mm}$ ).

To solve the equation, let:  $\Delta' \equiv [x_0 \cdot (x_{PMT} - x_0) + y_0 \cdot (y_{PMT} - y_0)]^2 - (x_0^2 + y_0^2 - r_{neck}^2) \cdot [(x_{PMT} - x_0)^2 + (y_{PMT} - y_0)^2]$ , and then we get:

$$a'_\pm = |\vec{X}_{PMT} - \vec{X}_0| \cdot \frac{-[x_0 \cdot (x_{PMT} - x_0) + y_0 \cdot (y_{PMT} - y_0)] \pm \sqrt{\Delta'}}{(x_{PMT} - x_0)^2 + (y_{PMT} - y_0)^2}, \text{ if } \Delta' > 0, \quad (4.4)$$

Similar to the ray-sphere case, if  $a'_+ > a'_- > 0$ , the length of the path inside the cylinder is  $a'_+ - a'_-$ . Due to this geometry, the event position should be outside the cylinder, the condition  $(x_0^2 + y_0^2 \geq r_{neck}^2)$  is automatically met. If  $a'_+ > 0 > a'_-$ , the event position should be inside the cylinder and the ray-vector intersects the cylinder with one point (while the other point is along the opposite direction). Thus the length of the path inside the cylinder is  $a'_+$ . If  $\Delta' \leq 0$ , the light ray never passes through the neck cylinder. Also note that here we consider the cylinder is infinitely long. This will also be cut off by the combined calculations of the other geometries. In addition, since only the neck region inside the PSUP is valid for the fitter, we should also ensure  $z < 8390\text{ mm}$  (in PSUP coordination).

To evaluate the length of the light ray (light path) in the scintillator region ( $d_{sp}$ ), the above three geometries needs to be combined carefully. The following two procedures go through all the possible situations. First combine the evaluations of the ray-sphere and the ray-plane intersections to calculate the light path in the AV scintillator region ( $d_{sp,AV}$ ). Then combine the evaluations of the ray-sphere and the ray-cylinder intersections to calculate the light path in the neck scintillator region ( $d_{sp,neck}$ ).

Since the valid fit requires the events inside the PSUP sphere, only the neck region inside the PSUP sphere (with  $6108 < z_{neck} < 8390\text{ mm}$ ) needs to be considered. The neck path calculation is allowed to be turned off. Detailed calculations are listed in A.3.

Once the total lengths of the light path in the scintillator region or the water region are calculated, the time of flight,  $t_{transit}$  is obtained by:

$$t_{transit} = \frac{|\vec{l}_p| - d_{sp}}{v_{gr,water}} + \frac{d_{sp}}{v_{gr,scint}}, \quad (4.5)$$

and thus the time residual,  $t_{res}$  is calculated.

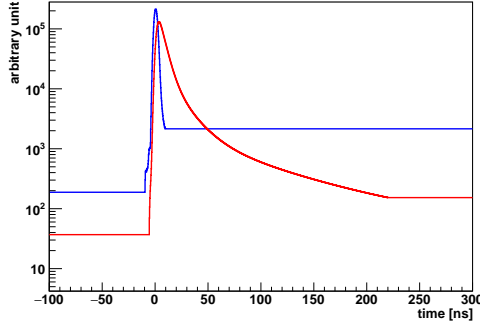


Figure 4.17: The timing pdfs used by the MP Partial Fitter. Blue: the timing pdf used by the MP Water Fitter; red: the scintillator timing pdf.

If  $d_{sp} = 0$ , the light path is always in the water. In this case, the fitter is the same as the MP Water Fitter. The fitter fits with the MP Water Fitter pdf. Once the light path passes through the scintillator region, the fitter fits with a scintillator timing pdf, the PMT time response modified to photon propagation time in scintillator, as shown in Fig. 4.17.

The performance of the fitter was studied with MC simulations. In a partial fill geometry with water level at 4.435 m, 2.5 MeV electrons are simulated inside the AV in the scintillator region only, the water region only and the whole AV region.

Fig. 4.18 and Fig. 4.19 show the MP Partial Fitter reconstructed results for these simulations. Fig. 4.18 shows the biases between the fit positions and MC positions, projected on the x axis. The distributions of position biases are fit with Gaussian functions. The values of Gaussian mean and sigma quantify the fit biases and resolutions. Table 4.2 lists these values.

Table 4.2: Reconstructed position biases and resolutions for simulated events in partial fill.

regions of simulated events	bias (mm)	resolution (mm)
scintillator region	-1.0	73.9
water region	-10.7	385.1
full region	6.9	331.72

For the events in water, the fit bias and resolution is comparable to the water phase results in Table 5.1. The events in the scintillator region have smaller fit bias and better resolution due to more triggered PMTs in the reconstruction.

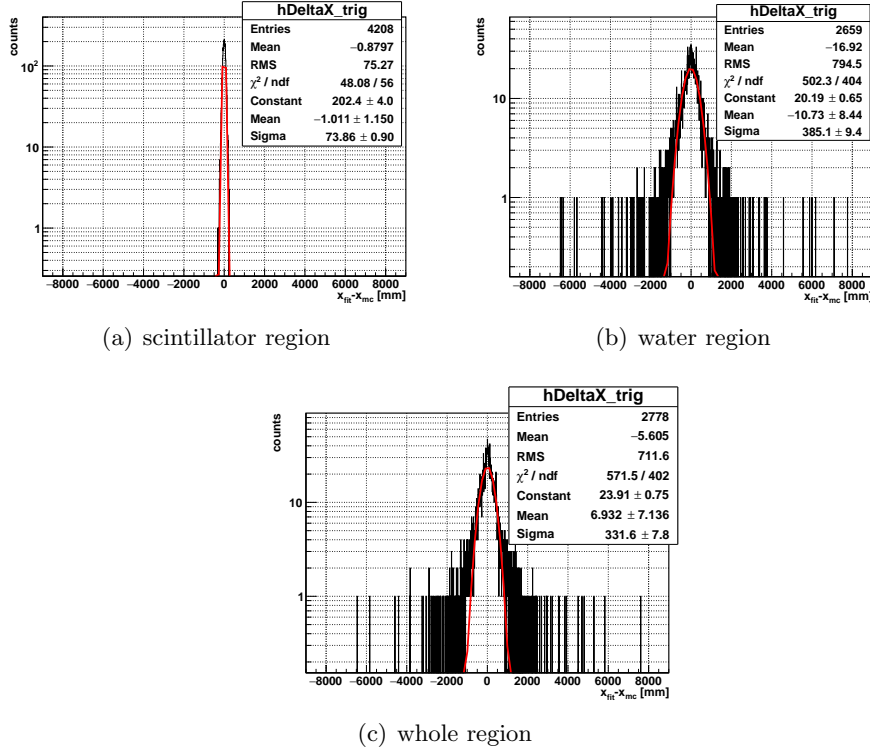


Figure 4.18: Distributions of fit position bias projected on x axis ( $x_{fit} - x_{MC}$ ).

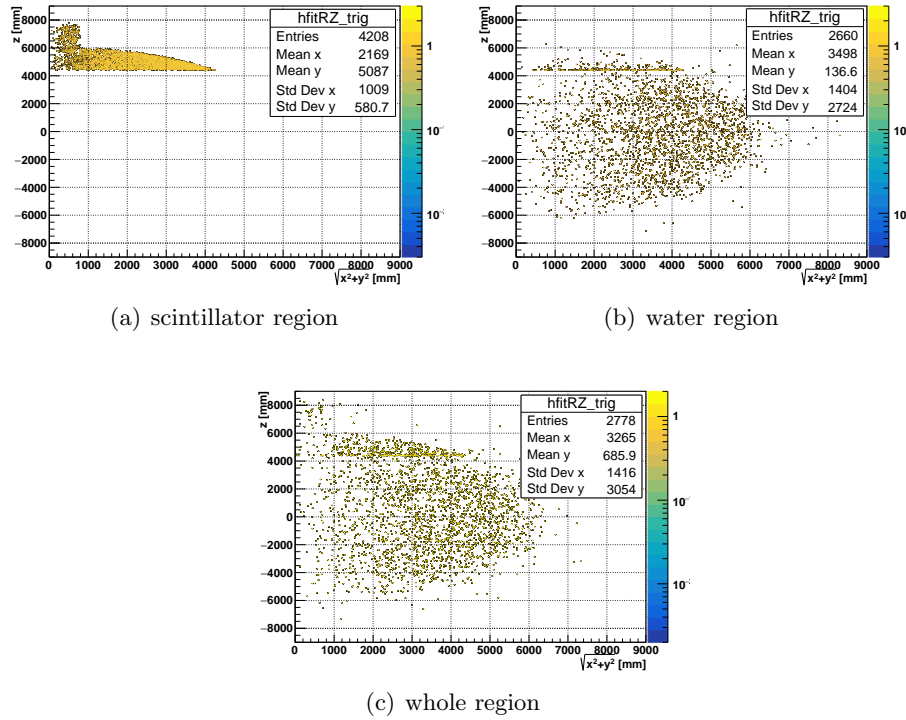


Figure 4.19: Fit results:  $\rho_{fit} = \sqrt{x_{fit}^2 + y_{fit}^2}$  vs.  $z_{fit}$ .

Fig. 4.19 shows the fitted  $\sqrt{x^2 + y^2}$  vs. fitted  $z$  positions. It shows that the fitter can distinguish different events in the water or scintillator region. The fitter gives reasonable results of the three different MC simulations.

the optical response of the liquid scintillator empirical model. This model consists  $n$  ( $n = 3$  or  $4$ ) exponential decays with a common rise time [138].

timing profile

scintillator timing

$$\sum_{i=1}^n A_i \cdot \frac{e^{-\frac{t}{\tau_i}} - e^{-\frac{t}{\tau_{rise}}}}{\tau_i - \tau_{rise}}$$

$$\left\{ \sum_{i=1}^n A_i \cdot \frac{e^{-\frac{t}{\tau_i}} - e^{-\frac{t}{\tau_{rise}}}}{\tau_i - \tau_{rise}} \otimes f_{PMT}(t - t') \right\} \otimes Gaus(t, 0)$$

from bench-top measurement, while the rise time,  $t_{rise} = 0.8$  ns the timing parameters  $t_i$ , amplitude  $a_i$  are determined by the bench-top measurements [139].

Table 4.3: scintillator  $\alpha/\beta$  timing parameters[111, 112, 139].

scintillator particles	timing [ns]				amplitudes			
	$t_1$	$t_2$	$t_3$	$t_4$	$a_1$	$a_2$	$a_3$	$a_4$
<b>LAB + 2g/L PPO (default scintillator)</b>								
$e^-$	4.88	15.4	66.0	400	0.665	0.218	0.083	0.0346
$\alpha$	4.79	18.4	92.0	900	0.427	0.313	0.157	0.1027
<b>LAB + 0.5g/L PPO (partial-fill phase)</b>								
$e^-$	7.19	24.81	269.87	—	0.553	0.331	0.116	—
$\alpha$	6.56	23.82	224.19	—	0.574	0.311	0.115	—
<b>LAB + 2g/L PPO + 0.5% molar concentrations DDA</b>								
$e^-$	5.0	12.1	33.3	499.0	0.68	0.21	0.07	0.04
$\alpha$	3.8	11.3	65.3	758.0	0.48	0.32	0.14	0.06
<b>LAB + 2g/L PPO + 0.5% molar concentrations Te+0.5% molar DDA</b>								
$e^-$	3.7	10.0	52.0	500.0	0.72	0.23	0.02	0.03
$\alpha$	3.69	15.5	79.3	489.0	0.63	0.23	0.07	0.07

pdfs for all timing

Radial bias is defined as the difference between the fitted and true position, projected

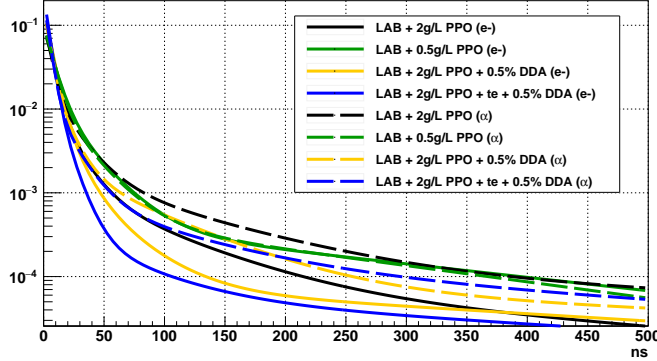


Figure 4.20: Timing profiles for liquid scintillators in different SNO+ phases.

along the radial component (unit vector) of the true position [129].

$$(\vec{X}_{fit} - \vec{X}_{true}) \cdot \hat{X}_{true}$$

The value of the mean radial bias is taken by fitting the histogram of the distributions of radial biases with a Gaussian profile and then get the mean of the fitted Gaussian profile.

### Water Level

$$\frac{\partial L}{\partial splitZ} = \frac{\partial L}{\partial tof} \cdot \frac{\partial tof}{\partial splitZ} = \frac{\partial L}{\partial tof} \cdot \frac{\partial a_3}{\partial splitZ}$$

$$\frac{\partial L}{\partial splitZ} = 0$$

Appendix: Levenberg-Marquardt method for fitter minimization (ref: press2007numerical)  
for M unknown parameters:  $a_0, a_1, \dots, a_{M-1}$  (for example, the 4 parameters of an event vertex:  $(x, y, z, t)$ )

The pdf can be expanded and fit with Chebyshev polynomials to obtain an analytic approximation function[1]. This analytical function can give proper analytical derivatives

The partial fitter is invulnerable to the change of pdfs caused by different PPO concentrations.

## 4.6 PMT Selectors for the Reconstruction

Several PMT selectors are used to select or remove PMTs from all the recorded PMTs triggered by an event and send the proper PMTs to the fitter for reconstruction. They are developed for optimizing the fitter or boosting up the fit speed:

- Straight Light Path Time Residual Cut Selector

This selector is used for the direction reconstruction for the SNO+ water phase. It is first developed by Singh for the MultiPath fitter. In the selector, the value of time residual ( $t_{res}$ ) is calculated for each triggered PMTs from an event and the PMT with a  $t_{res}$  value in a prompt time window of  $[-10.0, 120.0]$  ns is selected for the fitter. The selector calculates  $t_{res}$  by using straight line light path, which is the same to the MultiPath water fitter. This can remove the PMTs triggered by photons with late timing, such as the photons reflected off the detector elements (late light) and keep the possible Cherenkov ring hit pattern clear for the direction fitter to fit. Also, dropping the irrelevant PMTs can potentially boost up the fit speed.

- Mode Cut Selector

This selector was developed by the collaboration for all fitters. It checks the hit time ( $t_{PMT}$ ) distributions of all the triggered PMTs and finds a mode value of the hit time ( $t_{mode}$ ). If  $t_{mode}$  fails to be found, it calculates a median value ( $t_{median}$ ) instead[140]. Then it selects the PMT with  $t_{PMT} \in [t_{mode} + t_{low}, t_{mode} + t_{high}]$  ns. This selector is used to remove the PMTs triggered by noise and light light from reflection. The values of  $t_{low}$ ,  $t_{high}$  are optimized for different scintillators. For the MPW fitter, the optimized window is  $[t_{mode} - 50, t_{mode} + 100]$  ns by checking with the fit biases and resolutions for the  $^{16}\text{N}$  central run data in the water phase, while for the MP scint-water fitter the optimized window is  $[t_{mode} - 100, t_{mode} + 100]$  ns based on checking with the simulations.

- Uniform PMT Selector

I designed this selector for the partial-fill phase and the scintillator phase when a single event can trigger a large amount of PMTs. It reduces the number of the triggered PMTs to a designated number ( $n_{select}$ ) in order to boost up the fit speed. When an event triggers  $N$  calibrated PMTs, the selector goes through these recorded PMTs and uniformly picks up one PMT by an interval of  $\lceil N/n_{select} \rceil$ . If  $N \leq n_{select}$ , the selector does nothing. By doing this, the selector uniformly reduces the number of the PMTs for the fitter without an obvious bias.

- Earliest Hit PMT Selector

Similar to the uniform PMT selector, this selector reduces the number of the triggered PMTs to boost up the fit speed. It first groups the PMTs by their positions in the PMT support sphere. Take the centre of the sphere as coordinate origin, the sphere is divided by the azimuth angle  $\phi$  (as longitude) and zenith angle  $\theta$  (as latitude). In the sphere, the positions of the PMTs in  $\phi$ , ranging in  $[-\pi, \pi]$ , is uniformly divided into  $n$  intervals while the positions of the PMTs in  $\cos \theta$ , ranging in  $[-1, 1]$ , is also divided into  $n$  intervals. Thus, the PMTs are grouped into  $n \times n$  panels, see Fig. 4.21.

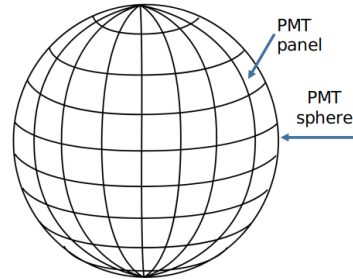


Figure 4.21: Group the PMTs by dividing the PMT sphere with latitudes and longitudes.

For each panel, the selector first drops the PMTs triggered too early ( $t_{PMT} < 100 \text{ ns}$ , where  $100 \text{ ns}$  is set as a default threshold). These PMTs could be triggered by noises, such as pre-pulsing. In the rest of the PMTs, the selector picks up one PMT with the earliest  $t_{PMT}$  in each panel. Thus the number of the PMTs is reduced to  $n \times n$  for the fitter, i.e.,  $n_{select} = n \times n$ . If  $N \leq n_{select}$ , the selector does nothing.

We can also use the other timing parameter, such as the  $t_{mode}$  or the  $t_{median}$  for

selecting the PMT in each panel. However, tests from the simulations for the scintillator phase show that using the earliest hit time gives less fit biases and better fit resolutions.

## 4.7 Energy Reconstruction

The previous sections mainly focus on vertex and direction reconstruction. For the energy reconstruction in the water phase

energy response processor, or the energy RSP fitter, is derived from SNO [136, 141].

It uses the fitted position and direction of an event as inputs and then calculates an effective

estimated  $N_\gamma$ ,

detailed detector effects are taken into account.

the asymmetric geometry of the detector, for example the neck cylinder on the top of the AV sphere; the actual number of online PMTs in a realistic physics run.

$^{16}\text{N}$  calibration scans at certain detector points.

Energy lookup table built from the simulation data set.

energy look up[142].

(energyRSP)

### 4.7.1 Energy Reconstruction in Partial-fill Phase

Up till this thesis writing, there is no proper energy fitter for the partial-fill phase works. I attempted two methods for the energy reconstruction in the partial-fill phase: the NHit scale method and the NHit ratio method. Both of them are based on the simulations. These two methods need more effects to be improved.

#### NHit Scale

In the partial-fill phase , In [143], to scale  $NHits$  based on several sets of simulations.

## NHit Ratio

The fitter follows the idea of the charge-ratio fitter for the partial energy reconstruction[144].

$$E = p_0 + p_1 \cdot NHit + p_2 \cdot NHit^2 \quad (4.6)$$

NHit ratio table based on position.

## 4.8 Other Reconstruction Algorithms

### 4.8.1 Hough Transformation for Direction Reconstruction

Hough transformation is a pattern recognition algorithm used in image analysis and computer vision[145]. This algorithm was first invented to extract patterns in bubble chamber[146], is used by Super-K[147].

The Hough transformation algorithm was used in SNO data analysis for counting the numbers of the Cherenkov rings caused by multiple charged particles in a high energy event such as atmospheric neutrinos event[115]. It is also suggested for the reconstruction of event direction in the SNO+ scintillator phase[148].

As illustrated in Fig. 4.22,

circular Hough transformation

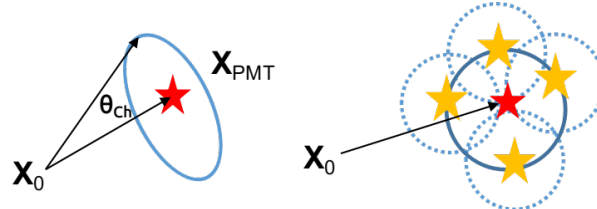


Figure 4.22: Hough transformation for catching the ring structure of Cherenkov signals and fitting the direction.

## 4.9 Conclusion

The Multi-path Fitter framework of event vertex reconstruction was developed for multiple SNO+ physics phases. Under this framework, the Multi-path Water Fitter works as an alternative fitter to provide additional reconstruction information for the water data and it gives proper position and direction resolutions for the water analysis. The Multi-path Scint-Water Fitter works as the prime fitter for the SNO+ partial-fill phase.

## Chapter 5

# SNO+ Water Phase Analysis

The SNO+ water data taking from May 2017 to September 2018. The period from May 2017 to October 2018 is the first stage of the water phase. During this stage, several calibration runs were taken, including the  $^{16}\text{N}$  calibration scans and the laserball scans. During the period from October 2018 to July 2019, over 20 tonnes of LAB (without PPO) was filled into the detector and the liquid mostly occupied the neck volume, slightly below the neck bottom. With the nitrogen cover gas on the top, the data taken during this period is considered as low background data.

The open dataset 100000 to 100399, from 4 to 14 May 2017.

### 5.1 High Level Cuts: Classifiers

A set of classifiers have been developed since the SNO analysis and been optimized for the SNO+ data [149].

- In time ratio (ITR) classifier

This classifier calculates the ratio of the number of hits in an optimized prompt time window ( $[-2.5, 5.0]$  ns for the water phase) to the total number of hits.

- $\beta_{14}$  isotropy classifier

This classifier uses Legendre polynomials to return the first ( $\beta_1$ ) and the fourth ( $\beta_4$ ) spherical harmonics of an event, where:

$$\beta_l = \frac{2}{N(N-1)} \sum_{i=1}^{N-1} \sum_{j=i+1}^N P_l(\cos \theta_{ij})$$

and  $P_l(\cos \theta_{ij})$  are Legendre polynomials.

The combination of these two polynomials returned by the classifier was practically chosen by the SNO collaboration to be:  $\beta_{14} = \beta_1 + 4\beta_4$  as this gives something that looks kinda gaussian-like for Cherenkov events. Essentially any deviation from zero suggests some polarity (i.e. the event is not isotropic).

- $\theta_{ij}$  isotropy classifier

describes the angle subtended at an event vertex by PMT #i and PMT #j.

$$\cos \theta_{ij} = \frac{(\vec{X}_{PMT\#i} - \vec{X}_{event}) \cdot (\vec{X}_{PMT\#j} - \vec{X}_{event})}{|\vec{X}_{PMT\#i} - \vec{X}_{event}| |\vec{X}_{PMT\#j} - \vec{X}_{event}|}$$

## 5.2 $^{16}\text{N}$ Calibration Scans in the Water Phase

During the water phase, an Nitrogen-16 ( $^{16}\text{N}$ ) calibration source was deployed for internal detector calibration scans in June and November, 2017 and external detector scans in March, 2018.

The  $^{16}\text{N}$  calibration runs provide an ideal test of fitter performance. From a comparison of reconstructions for data and MC, we can also extract the resolution and bias of the fitter. Here I worked out the vertex and the direction reconstruction performances for both of the RAT water fitter and the MPW. The vertex shifts as well as the uncertainties are evaluated.

The  $\gamma$ -rays emitted from the  $^{16}\text{N}$  source interact with the water in the detector mainly via Compton scattering. Figure 5.2 shows the spatial distributions of the first  $\gamma$ -ray interaction positions projected on the x axis (called spatial distribution  $S(x)$ ) obtained from MC simulation. The  $^{16}\text{N}$  source is considered as an electron source with a known spatial

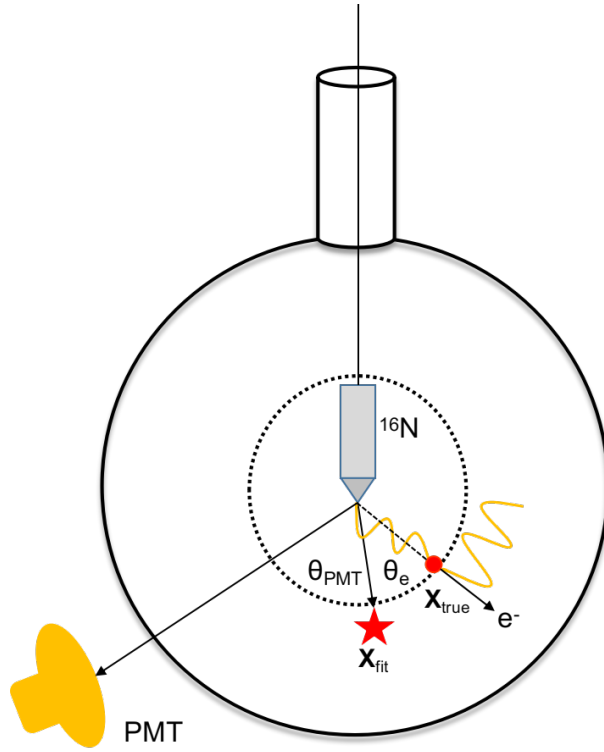


Figure 5.1: A cartoon shows the  $^{16}\text{N}$  source.

distribution[136]. For simplicity, in the following we always discuss the  $x$  component of the position vector  $\vec{X}$ .

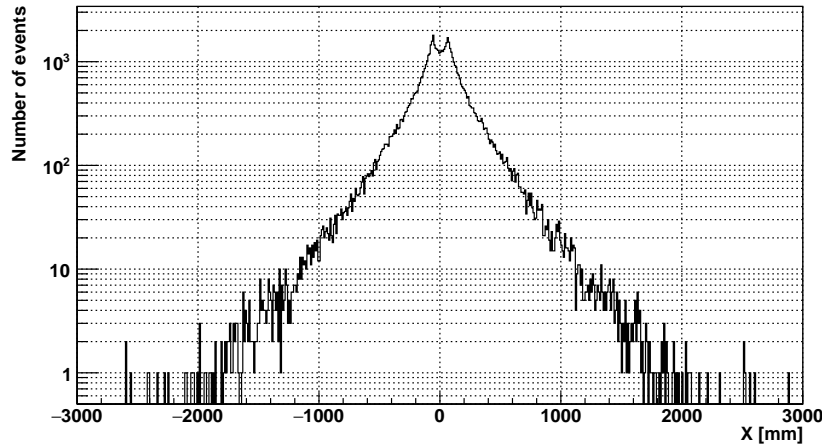


Figure 5.2: Spatial distributions of  $^{16}\text{N}$  first  $\gamma$ -rays interaction position projected on  $x$  axis, obtained from RAT simulations. The double-peak structure is due to the wall of the stainless steel container of the  $^{16}\text{N}$  source.

A position resolution function is defined for the reconstructed electron position distribution[136]:

$$R(x) = \frac{1 - \alpha_e}{\sqrt{2\pi}\sigma_p} \exp\left[-\frac{1}{2}\left(\frac{x - \mu_p}{\sigma_p}\right)^2\right] + \frac{\alpha_e}{2\tau_p} \exp\left[\frac{-|x - \mu_p|}{\tau_p}\right],$$

where  $\alpha_e$  is the fractional exponential component,  $\sigma_p$  is the Gaussian width (corresponding to the position resolution),  $\mu_p$  is the Gaussian shift (corresponding to the position bias) and  $\tau_p$  is the exponential slope (corresponding to the position distributions in tails).

For electrons from the  $^{16}\text{N}$  calibration source, their spatial distribution function  $N_R(x)$  can be described by the position resolution function smeared by the convolution of  $S(x)$  as[136]:

$$N_R(x) = \int_{-\infty}^{+\infty} S(x)R(x_{fit} - x)dx.$$

Since the  $S(x)$  and  $N_R(x)$  are histograms obtained from the data and MC, we calculate by the bin value  $x_i$ :

$$N_R(x_i) = \sum_{x_i=-\infty}^{+\infty} S(x_i)R(x_{fit}^i - x_i).$$

The  $\chi^2$  is calculated by:

$$\chi^2 = \sum_{i=0}^{N_{bins}} \left[ \frac{N_R(x_{fit}^i) - N_R^{fit}(x_{fit}^i)}{\sigma_i} \right]^2,$$

where  $N_R^{fit}$  is a trial fit to the  $N_R$  by tuning the  $\{\alpha_e, \mu_p, \sigma_p, \tau_p\}$  and  $\sigma_i$  is taken as the bin width of the histograms.

By minimizing the  $\chi^2$ , the parameters of the resolution function,  $\{\alpha_e, \mu_p, \sigma_p, \tau_p\}$  and a best  $N_R^{fit}$  are obtained.

Fig. 5.2 shows a comparison of the reconstructed x position of  $^{16}\text{N}$  events between data and MC. The reconstructed position distributions are fitted with  $N_R^{fit}$ .

Table 5.1 summarizes the values of position resolution parameters obtained from data and MC of  $^{16}\text{N}$  calibration runs at the detector center.

Vertex likelihood surface for an typical  $^{16}\text{N}$  event (calibration run-100934\_s000\_p001, event GTID = 61836), projected on X-Y, X-Z and Y-Z planes. A clean global maxima

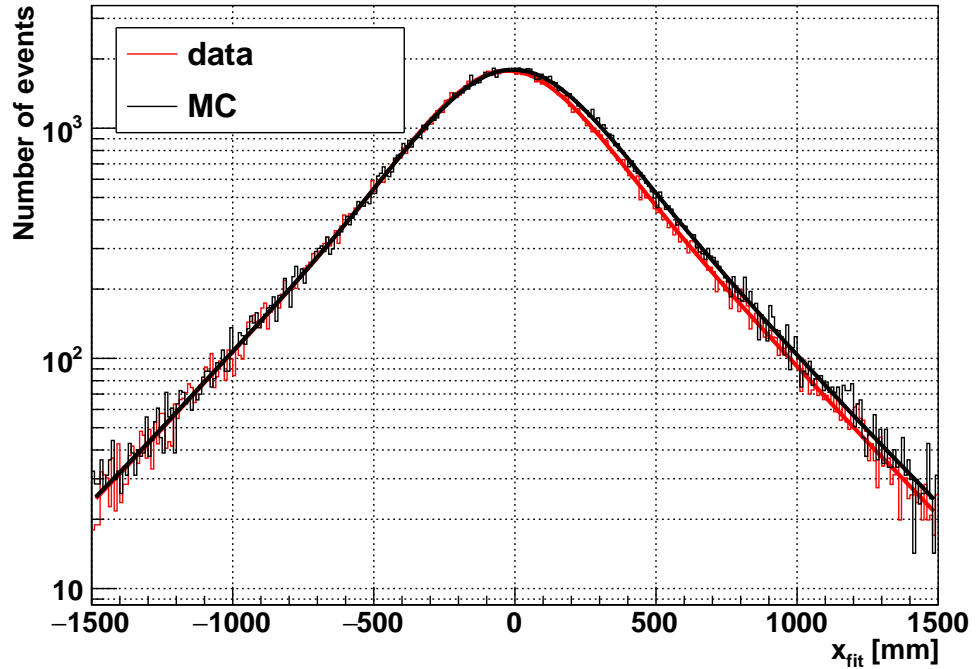


Figure 5.3: Position resolutions, compared the data (red) and MC (black). The resolution fit functions are overlaid with histograms.

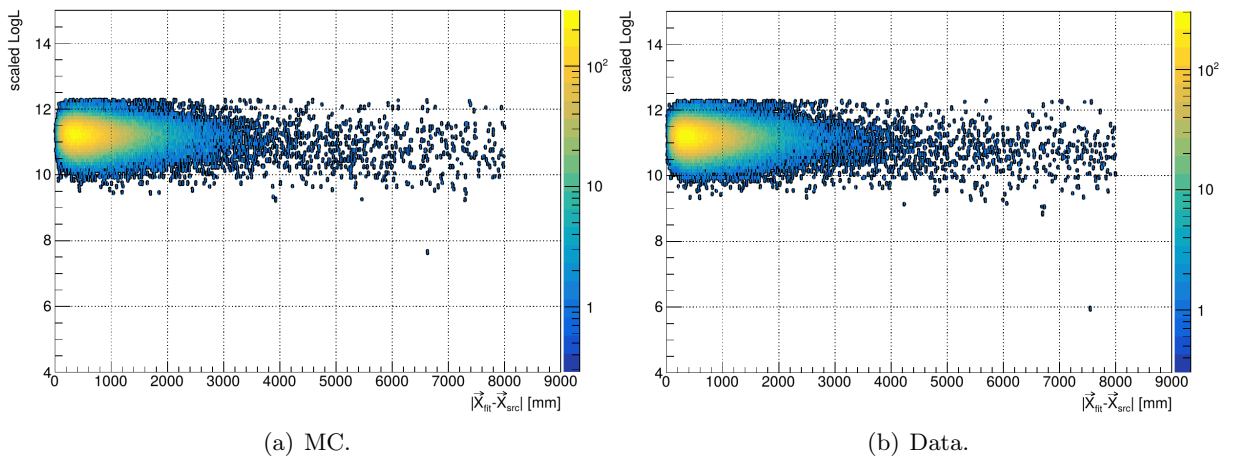


Figure 5.4: Fit position biases ( $|X_{fit} - X_{MC}|$ ) vs FOM (scaled LogL) for the <sup>16</sup>N central run-107055.

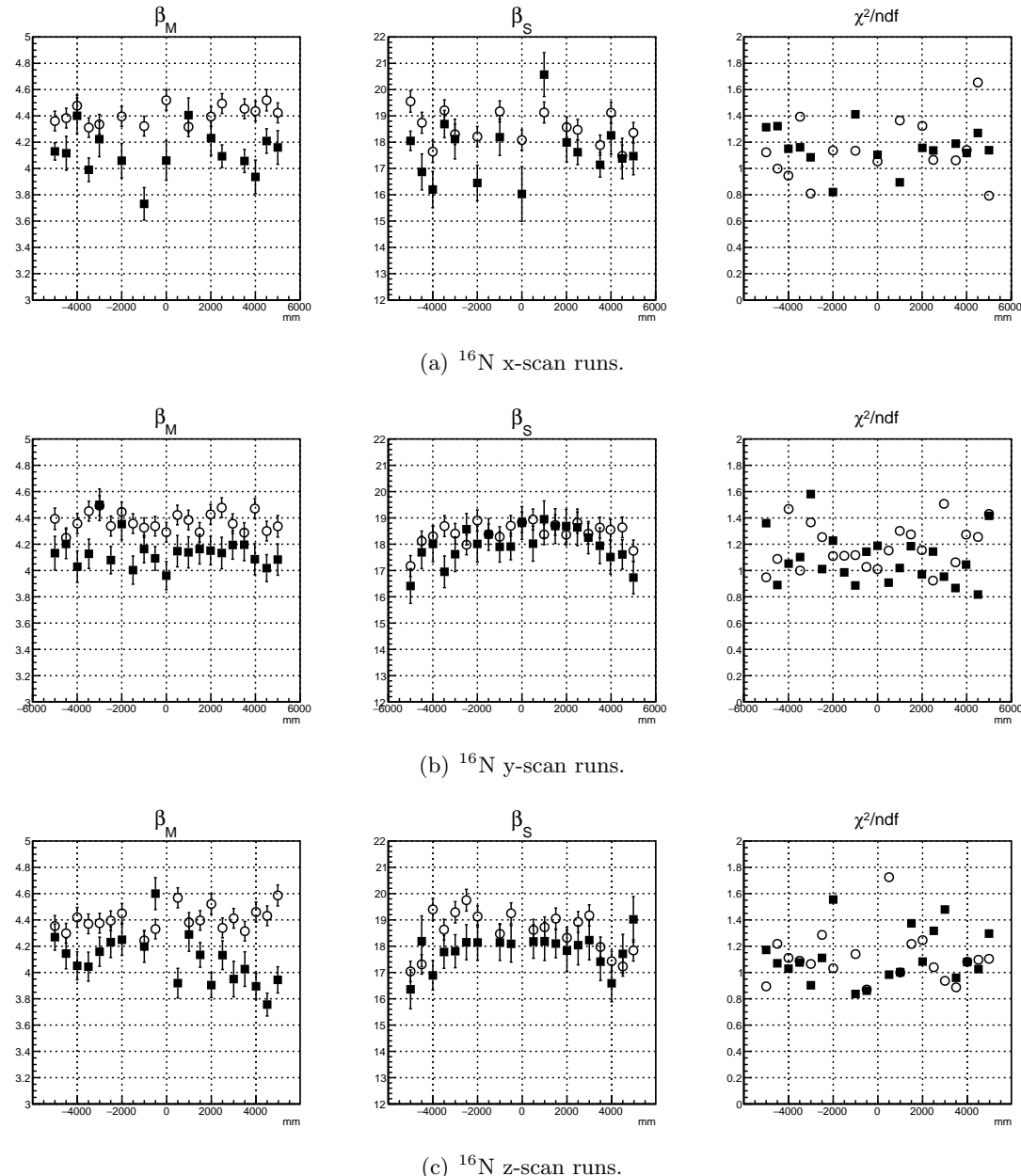


Figure 5.5: Fit direction resolutions ( $|\vec{X}_{fit} - \vec{X}_{MC}|$ ) vs FOM (scaled LogL) for the  $^{16}\text{N}$  central run-107055.

Table 5.1: Position resolution parameters for the MP Water Fitter.

MPW fitter	$\alpha_e$	$\sigma_P$ (mm)	$\tau_P$ (mm)	$\mu_P$ (mm)
data	$0.58 \pm 0.04$	$175.8 \pm 3.8$	$288.0 \pm 5.7$	$-28.8 \pm 1.0$
MC	$0.51 \pm 0.05$	$195.2 \pm 3.3$	$298.4 \pm 6.1$	$-10.9 \pm 1.0$

gives the reconstructed vertex: the fitted position is at (-211.958, 503.399, 275.990) mm and the fitted time at 217.03885 ns. This is shown in Fig. 5.6.

emit  $\gamma$ -rays. These  $\gamma$ -rays will Compton scatter off electrons and the electrons will emit Cherenkov light to be detected by the PMTs.

Table 5.2: Candidate events in the open dataset. Compared the fitted results of the candidate events with different fitters.

axis	linear fit (mm)	scaling
x scaling	0.006%	$(1 + 0.006/100) \cdot x_{MC}$
y scaling	-0.026 %	$(1 - 0.026/100) \cdot y_{MC}$
z scaling	-0.03%	$(1 - 0.03/100) \cdot z_{MC}$

Table 5.3: Candidate events in the open dataset. Compared the fitted results of the candidate events with different fitters.

	Data	MC
b (MPW)	0.006%	$(1 + 0.006/100) \cdot x_{MC}$
$\delta_E$ (MPW)	-0.026 %	$(1 - 0.026/100) \cdot y_{MC}$
b (Rat6.5.5)	0.006%	$(1 + 0.006/100) \cdot x_{MC}$
$\delta_E$ (Rat6.5.5)	-0.026 %	$(1 - 0.026/100) \cdot y_{MC}$

### 5.2.1 Angular Resolution

Here the 'true' direction is defined as the direction pointing from the source positions to the fitted position:  $\vec{u}_{true} = \vec{X}_{fit} - \vec{X}_{source}$ . The angle  $\theta$  is the displacement between the 'true' and the reconstructed directions and  $\cos \theta = \vec{u}_{true} \cdot \vec{u}_{fit}$ .

An angular resolution function was

It is defined as a combination of two exponential components:

$$P(\cos \theta) = \alpha_M \frac{\beta_M \exp[-\beta_M(1 - \cos \theta)]}{1 - \exp(-2\beta_M)} + (1 - \alpha_M) \frac{\beta_s \exp[-\beta_s(1 - \cos \theta)]}{1 - \exp(-2\beta_s)}, \quad (5.1)$$

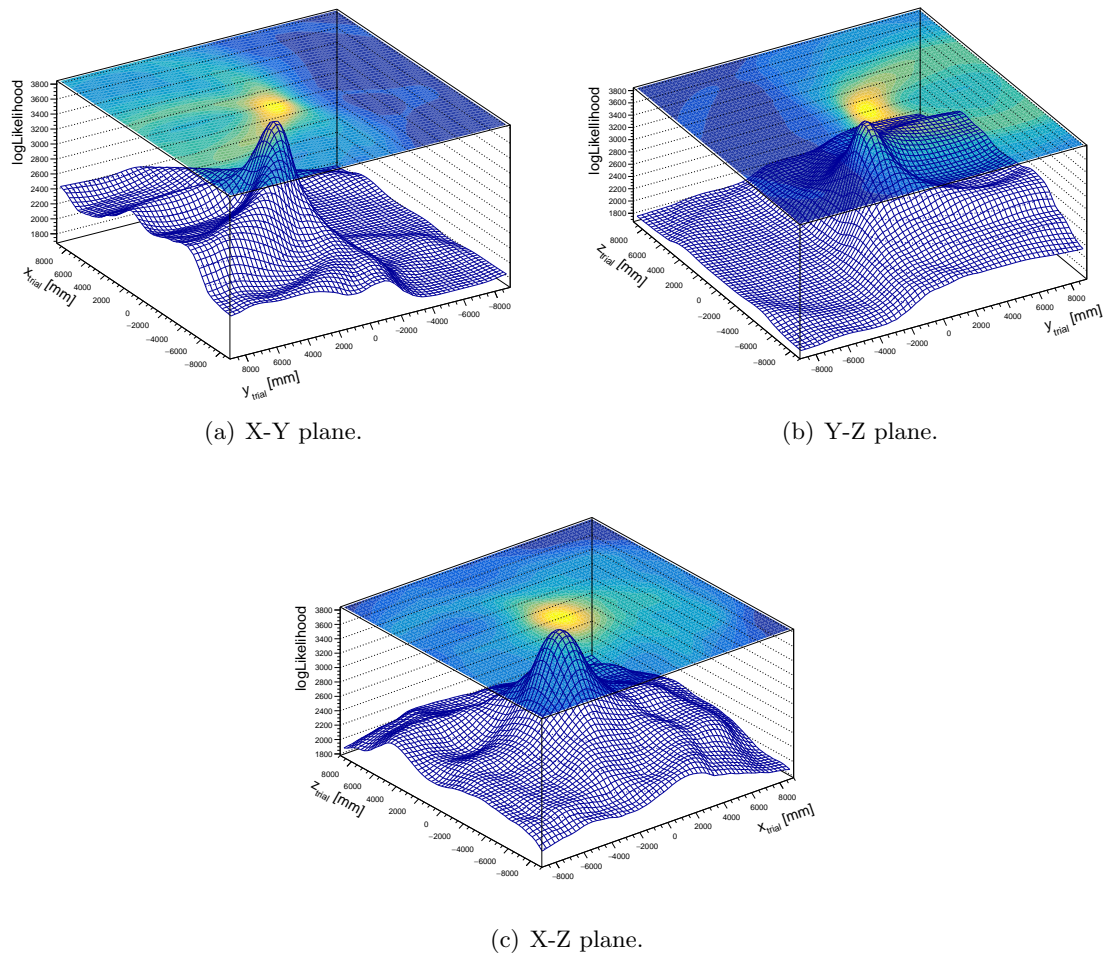


Figure 5.6: Likelihood surface of an  $^{16}\text{N}$  event projected on X-Y, Y-Z, X-Z planes. A clear global maxima is reached for the fitted vertex.

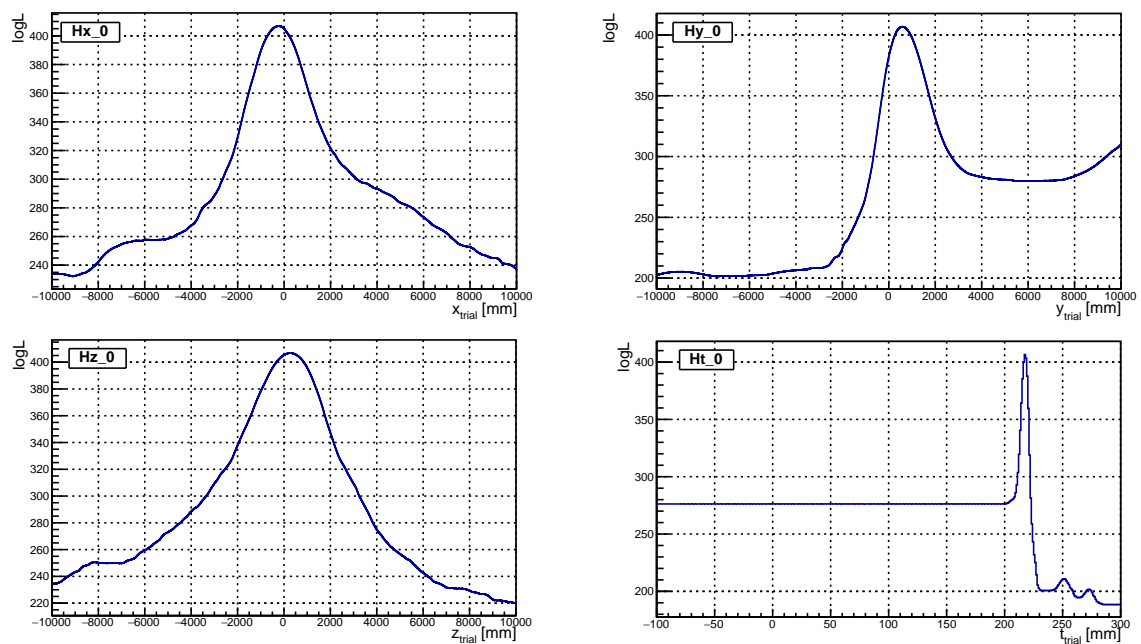


Figure 5.7: Likelihood surface of an  $^{16}\text{N}$  event projected on x, y, z, t axes.

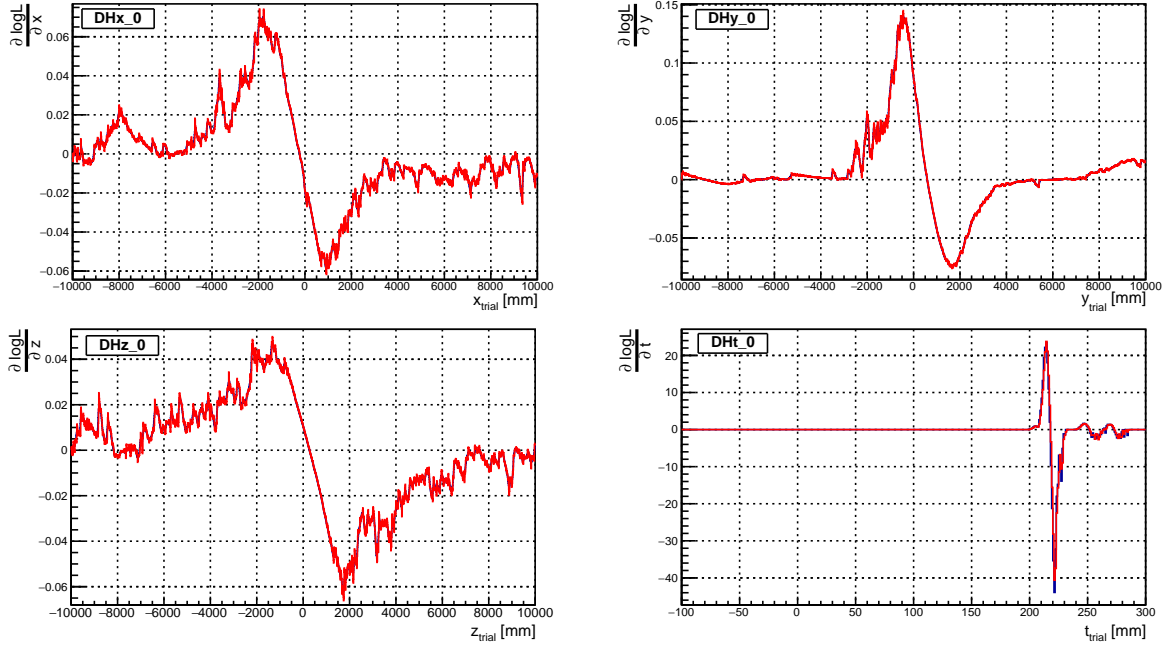


Figure 5.8: Derivatives of logLikelihood of an  $^{16}\text{N}$  event projected on x, y, z, t axes. The analytical derivatives (blue) are overlaid with numerical derivatives (red). They are well-matched.

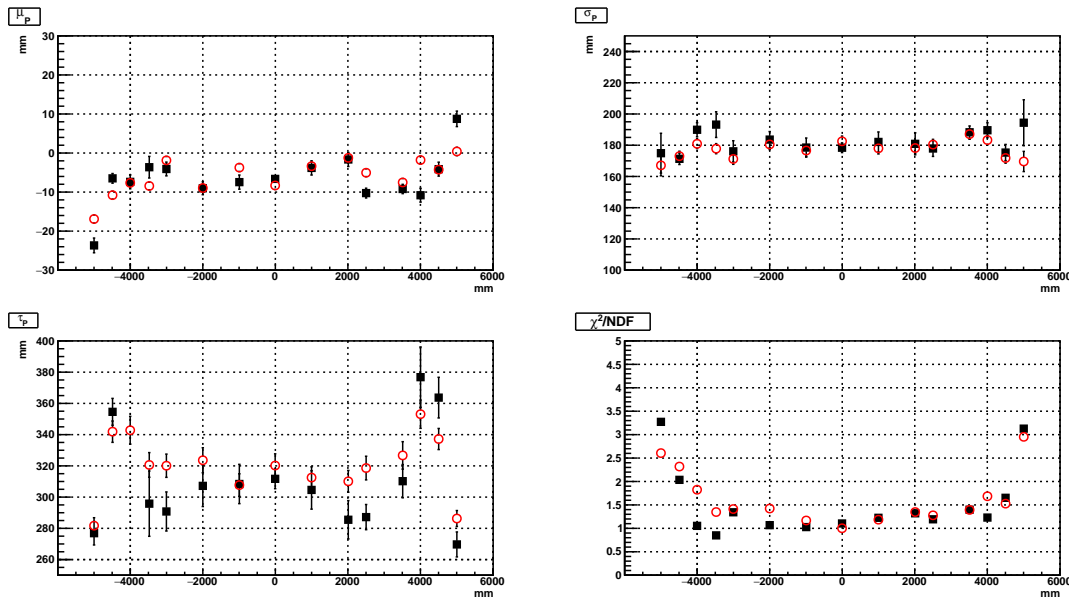


Figure 5.9: X scan.

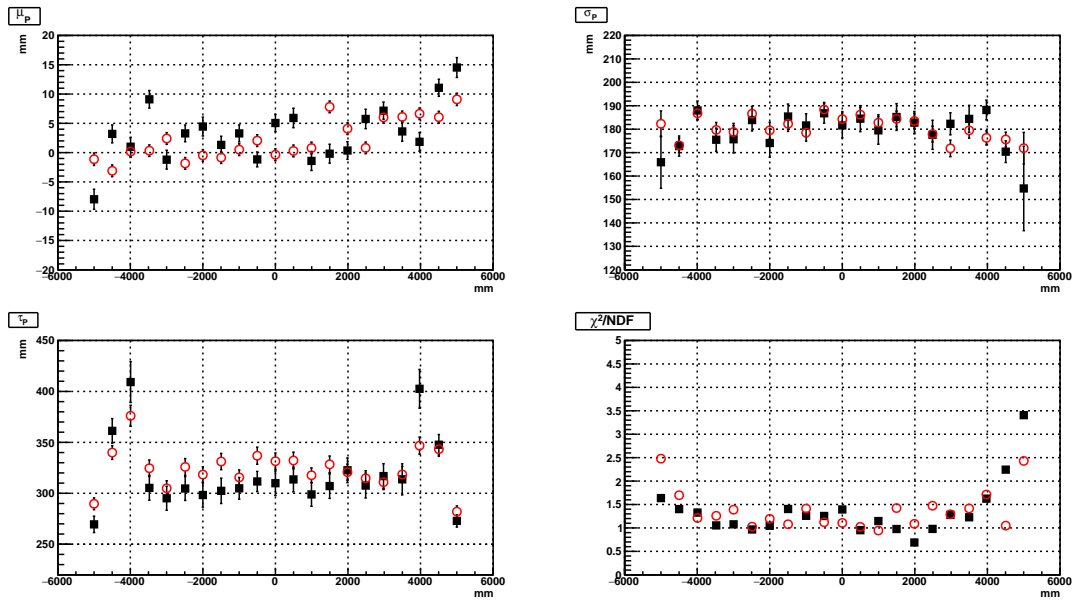


Figure 5.10: Y scan.

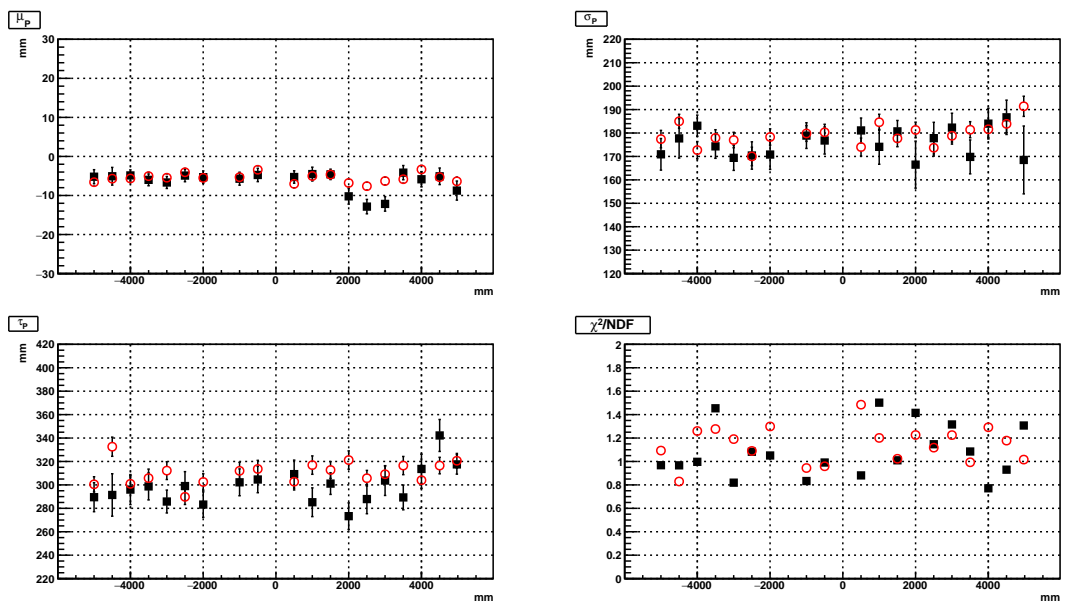


Figure 5.11: Z scan. The data (black boxes) is compared with MC (red circles).

Table 5.4: Candidate events in the open dataset. Compared the fitted results of the candidate events with different fitters.

axis	Gaussian fit (mm)
x shift	0.42±4.13
y shift	-1.05±3.79
z shift	-0.43±2.88

where the parameters:  $\beta_M$  and  $\beta_S$  are the “decay” constants or “slopes” of the two exponential components; the  $\alpha_M$  is the fraction between two exponential components. events following the exponential with slope  $\beta_M$ .

To extract the direction resolutions, a distance cut  $|\vec{X}_{fit} - \vec{X}_{src,manip}| > 1.5\text{ m}$  is applied.

To avoid the effects from the tails,  $[0.3,1] \text{ itr} > 0.55$  and  $-0.12 < \beta_{14} < 0.95$  radius cut for the FV:  $r < 5500\text{ mm}$ .

The resolution results are shown in Table. 5.2.1.

107055	$\beta_M$	$\beta_S$	$\alpha_M$	$\chi^2/\text{ndf}$	$\cos \theta_{0.5}$	$\cos \theta_{0.8}$	$\cos \theta_{0.9}$
Rat data	$3.50 \pm 0.11$	$18.48 \pm 0.82$	$0.51 \pm 0.02$	$127.8/140$	0.991	0.733	0.338
Rat MC	$3.74 \pm 0.15$	$19.58 \pm 0.92$	$0.48 \pm 0.02$	$137.1/138$	1	0.768	0.398
107055	$3.888 \pm 0.246$	$17.96 \pm 1.10$	$0.550 \pm 0.030$	$80.69/66$	0.974	0.740	0.384
107055	$4.487 \pm 0.223$	$22.23 \pm 1.41$	$0.590 \pm 0.027$	$74.01/66$	0.962	0.759	0.450

107055	$\beta_M$	$\beta_S$	$\alpha_M$	$\chi^2/\text{ndf}$	$\cos \theta_{0.5}$	$\cos \theta_{0.8}$	$\cos \theta_{0.9}$
MPW data	$4.15 \pm 0.18$	$19.08 \pm 0.94$	$0.58 \pm 0.02$	$77.1/66$	0.964	0.744	0.410
MPW MC	$4.42 \pm 0.19$	$20.41 \pm 1.01$	$0.56 \pm 0.02$	$83.8/66$	0.974	0.768	0.454
Rat data	$3.76 \pm 0.18$	$17.90 \pm 0.82$	$0.55 \pm 0.02$	$70.5/66$	0.974	0.731	0.364
Rat MC	$4.02 \pm 0.18$	$20.89 \pm 0.92$	$0.54 \pm 0.03$	$94.9/66$	0.979	0.753	0.409

Fig. 5.12 shows the fits of the angular distributions after the distance cuts.

To describe the  $\cos \theta_e$  distribution, the angles that contain 50%, 80% and 90% of the reconstructed events, the  $\cos \theta_{0.5}$ ,  $\cos \theta_{0.8}$  and  $\cos \theta_{0.9}$  can also be used. Their values are solved numerically by the equation 5.2 below (take  $\cos \theta_{0.5}$  as an example):

$$\frac{\int_{\cos \theta_{0.5}}^1 P(\cos \theta_e) d \cos \theta_e}{\int_{-1}^1 P(\cos \theta_e) d \cos \theta_e} = 50\%, \quad (5.2)$$

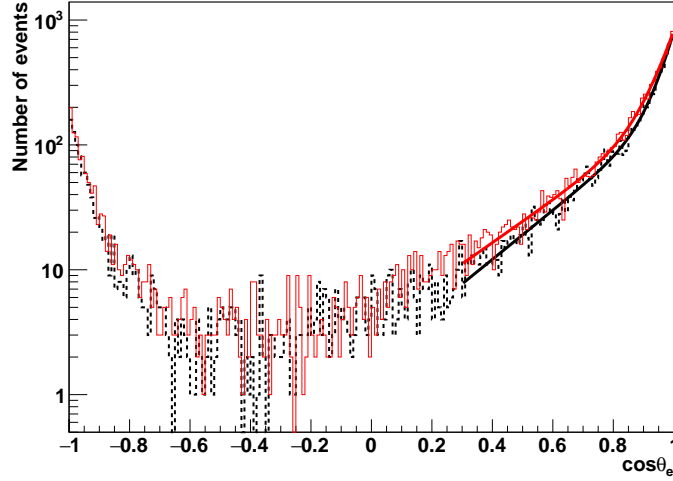


Figure 5.12: Angular distributions extracted from the data (red solid line) and the MC (black dashed line); both are reconstructed by the MPW fitter. These distributions are fitted with the angular resolution functions ranging from 0.3 to 1.

where  $P(\cos \theta_e)$  is the direction resolution function with the best fitted parameters. If these values are large, the  $\cos \theta_e$  distribution is sharper and more peaked around +1.

parameter	$\mu$ (%)	$\sigma$ (%)
$\Delta(\alpha_M)_{relative} \equiv (\alpha_{M,data} - \alpha_{M,MC})/\alpha_{M,MC}$	-5.7	3.4
$\Delta(\beta_M)_{relative} \equiv (\beta_{M,data} - \beta_{M,MC})/\beta_{M,MC}$	-3.8	2.3
$\Delta(\beta_S)_{relative} \equiv (\beta_{S,data} - \beta_{S,MC})/\beta_{M,MC}$	-6.9	3.5

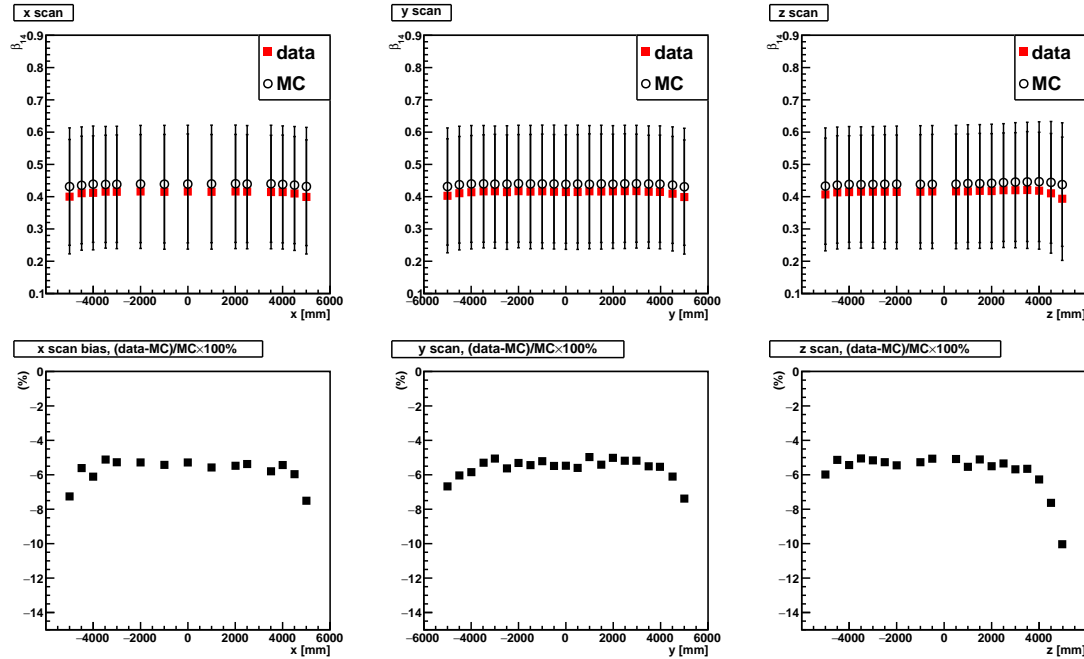
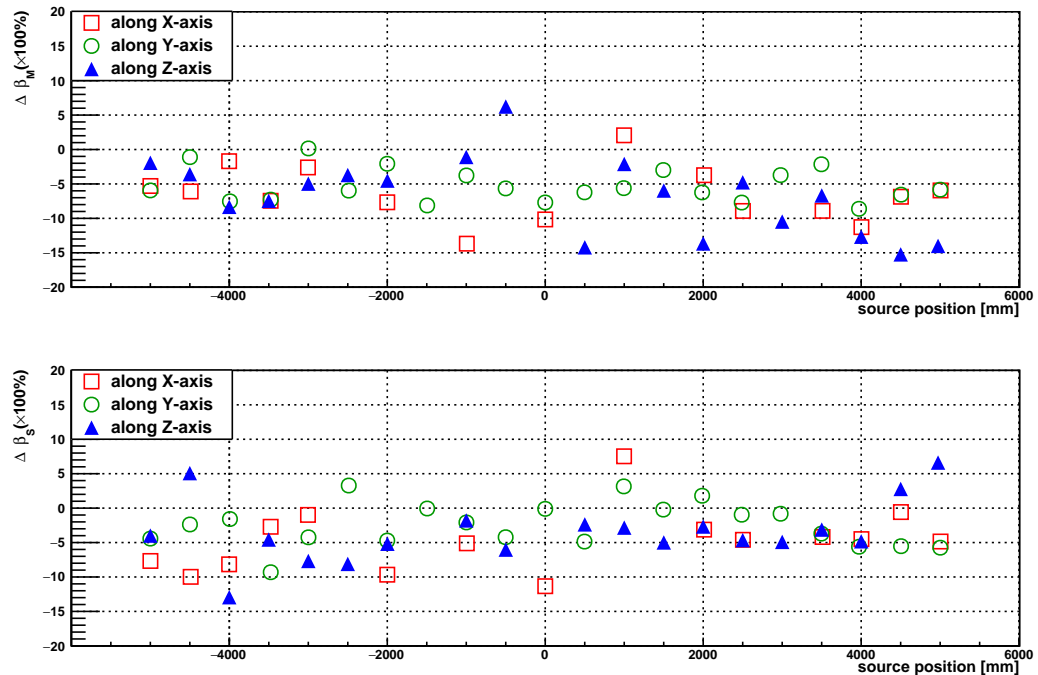
$\beta_{14}$  systematic

### 5.3 Energy

The reconstructed energy of the  $^{16}\text{N}$  events are shown in Fig. 5.18. The results from the MC and the data are compared.

$$\sigma = b\sqrt{T_{eff}}$$

$$P(T_{eff}) = N \int P_{source}(T_e) \frac{1}{\sqrt{2\pi}\sigma} \exp\left[-\frac{[(1+\delta_E)T_{eff} - T_e]^2}{2\sigma^2}\right] \quad (5.3)$$

Figure 5.13:  $\beta_{14}$  systematic for various  $^{16}\text{N}$  scans.Figure 5.14:  $\Delta \beta_M$  (top) and  $\Delta \beta_S$  (bottom) systematic for various  $^{16}\text{N}$  scans along three axes.

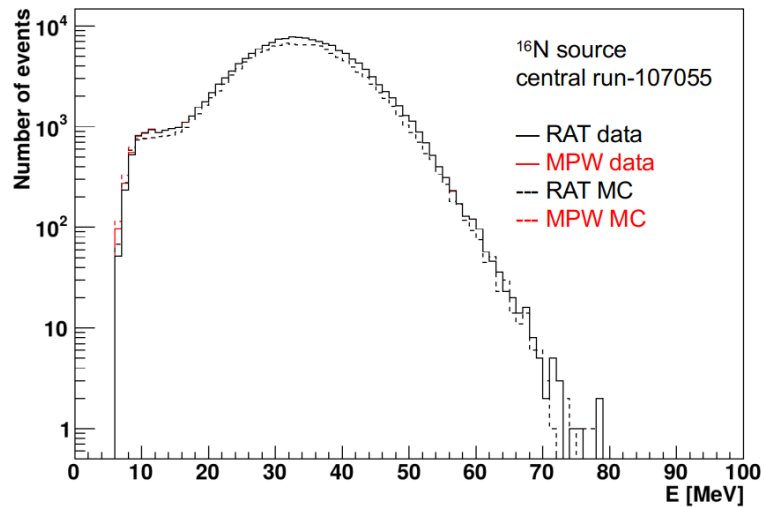


Figure 5.15: NHit spectrum for the  $^{16}\text{N}$  central run-107055. Dashed lines for the MC and solid lines for the data; red for the MPW fitter results and black for the Rat results.

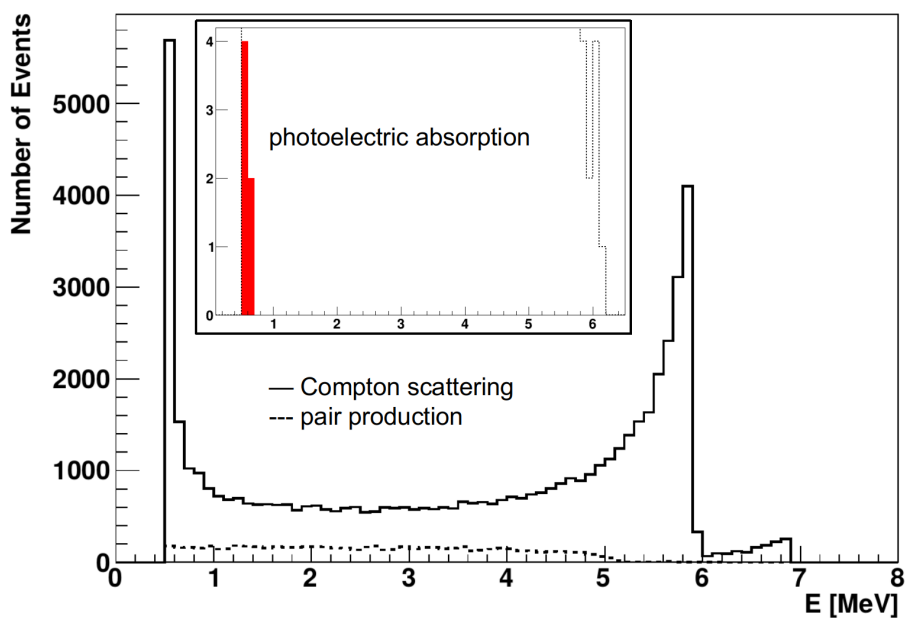


Figure 5.16: Energy spectrum, extracted from  $10^5$  MC simulation events.

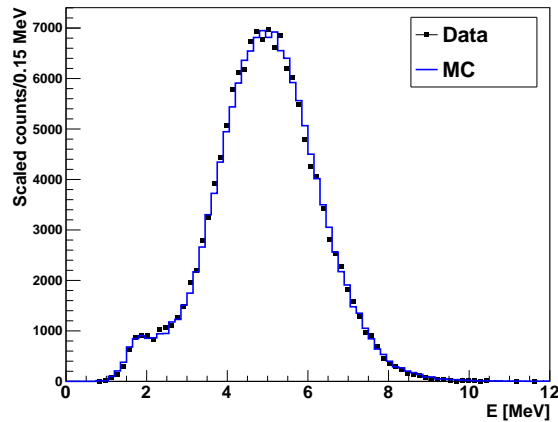


Figure 5.17: Reconstructed  $^{16}\text{N}$  energy spectrum for run-106925 ( $\vec{X}_{\text{source}} = (-186.0, 254.0, -4999.899)$  mm).

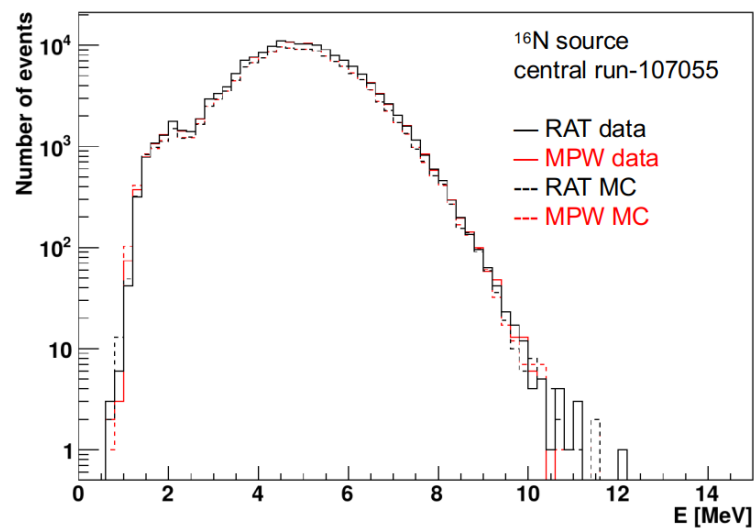


Figure 5.18: Reconstructed energy spectrum for the  $^{16}\text{N}$  central run-107055. Dashed lines for the MC and +solid lines for data; red for the MPW fitter results and black for the Rat results.

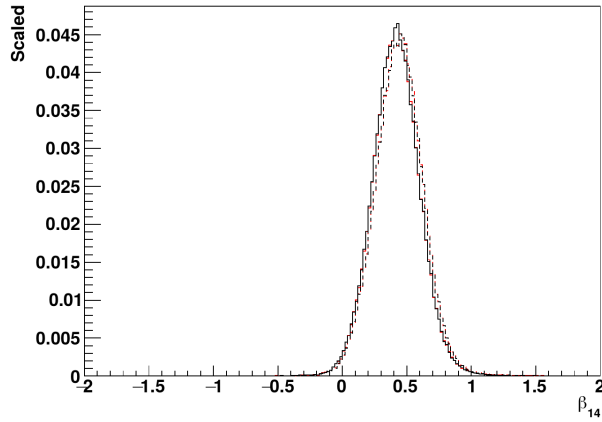


Figure 5.19: Distributions of  $\beta_{14}$  for the  $^{16}\text{N}$  central run-107055. Dashed lines for the MC and solid lines for data; red for the MPW fitter processed results and black for the Rat results.

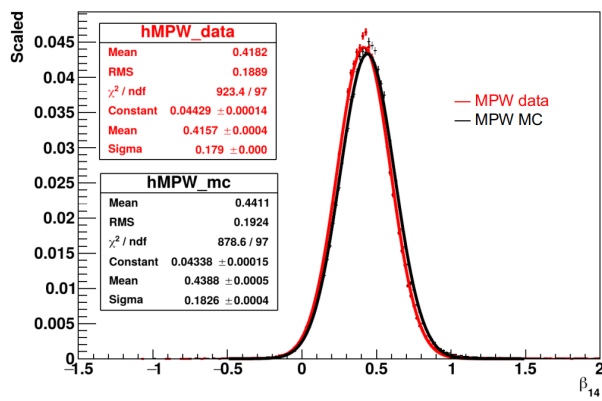


Figure 5.20: Comparisons of the  $\beta_{14}$  for the data and the MC. Both of the distributions are the MPW processed results and are fitted with Gaussian distributions in a region of  $[-0.5, 1.5]$ . The data shows a smaller mean value (0.4157) than the MC (0.4388).

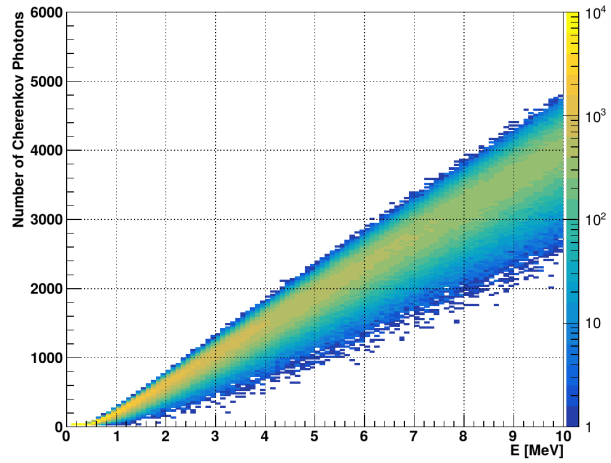


Figure 5.21: Electron energy vs number of Cherenkov photons.

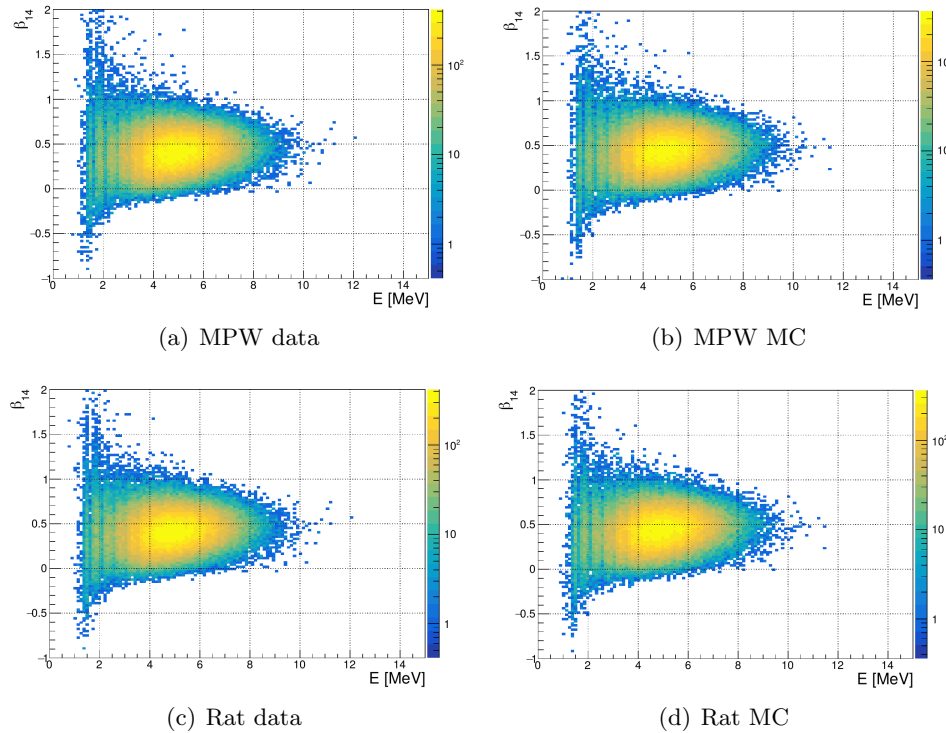


Figure 5.22: Energy vs  $\beta_{14}$  for the data and MC. Both the Rat and the MPW results are shown.

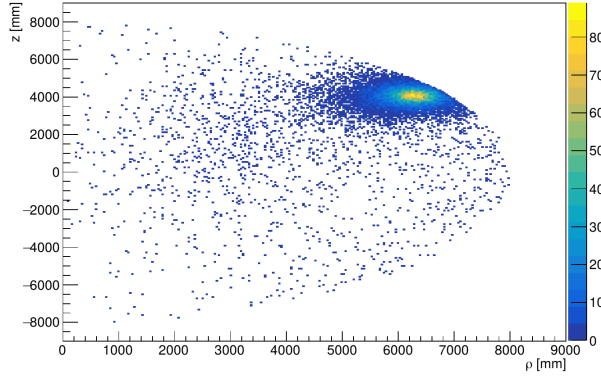


Figure 5.23:  $^{16}\text{N}$  external run-111230 with a nominal position at [-5861,-2524,4001] mm; MPW results.

## 5.4 Extracting $\gamma$ -rays from Neutron Capture

The AmBe calibration source is used for the calibrations of the SNO+ neutron capture process.

## 5.5 Solar $\nu_e$ Analysis and Background Separation in Water Phase

solar neutrino candidate events in the open dataset.

### Open Dataset Analysis

MPW fit results

fiducial volume cut

elastic scattering  $\nu_e + e^- \rightarrow \nu_e + e^-$  the maximum kinetic energy of the recoil electron is  $T_{max} = \frac{2E_\nu^2}{2E_\nu + m_e c^2}$  the cross section is  $\sigma(\nu_e + e^- \rightarrow \nu_e + e^-) = 9.52 \times 10^{-44} (E_\nu / 10 \text{ MeV}) \text{ cm}^2$  the expected solar neutrino rate is  $R = A \int_{T_{thresh}}^{T_{max}}$

A “solar angle”,  $\theta_{sun}$  is the direction of the event relative to the Sun’s location,  $\cos \theta_{sun} \equiv \vec{u}_{event} \cdot (\vec{X}_{event} - \vec{X}_{sun})$ , where  $\vec{X}_{event} - \vec{X}_{sun}$  can be replaced by the Sun’s location relative to the SNOLAB location since the whole lab can be treated as a point regarding the long distance to the Sun.

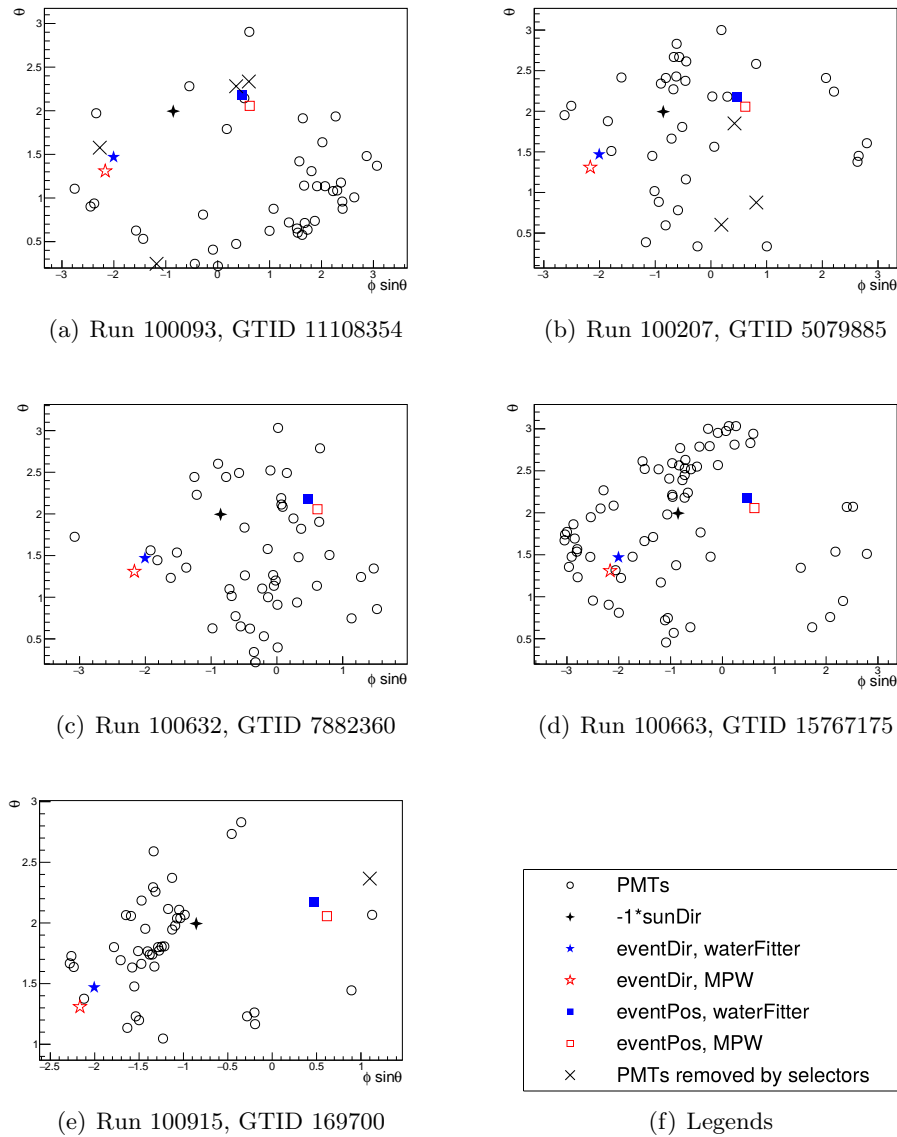


Figure 5.24: Fit results for the candidate events, projected onto PMT sinusoidal maps. Black circles stand for the hit PMTs used by the fitter; crosses stand for the hit PMTs removed by the selectors; blue full star stands for the event direction fitted by the waterFitter; red open star stands for the direction fitted by the MPW; full double diamond stands for the solar direction $^{\ast}-1$ ; blue full square stands for the event position fitted by the waterFitter; open square stands for the position fitted by the MPW.

Table 5.5: Candidate events in the open dataset. Compared the fitted results of the candidate events with different fitters.

Fitter	Run	GTID	$z - 0.108(\text{m})$	$R(\text{m})$	$(R/R_{av})^3$	$\cos \theta_{\text{sun}}$	SNO+ Day
Rat	100093	11108354	3.49	3.57	0.21	-0.954459	2683.92
MPW	–	–	3.43	3.52	0.20	-0.906388	–
Rat	100207	5079885	-2.61	4.60	0.45	0.816215	2687.04
MPW	–	–	-3.63	<b>7.61</b>	2.03	<b>0.656374</b>	–
Rat	100632	7882360	1.77	3.19	0.15	0.937212	2696.93
MPW	–	–	1.67	3.11	0.14	0.910527	–
Rat	100663	15767175	-4.33	4.96	0.56	0.977517	2698.18
MPW	–	–	-4.45	5.07	0.60	0.979943	–
Rat	100915	169700	-1.00	5.10	0.61	0.341287	2701.23
MPW	–	–	-1.08	5.08	0.61	0.336706	–

Table 5.6: Candidate events in the open dataset, searched by the MPW fitter.

Run	GTID	energy	$z - 0.108$	$R$	$(R/R_{av})^3$	$\cos \theta_{\text{sun}}$
100093	11108354	5.827	3.43	3.52	0.20	-0.907005
100632	7882360	6.183	1.67	3.11	0.14	0.9146124
100663	15767175	6.182	-4.45	5.07	0.60	0.9807349
100915	169700	5.684	-1.07	5.08	0.61	0.3385341
100984	8621621	5.701	0.76	4.75	0.502	-0.647735
101075	11673714	5.667	4.43	5.18	0.64	0.5873025

### TMVA analysis

The Toolkit for Multivariate Data Analysis with ROOT (TMVA) [150, 151]

Boosted Decision Tree (BDT) method is used for the multiple variable analysis (MVA).

Receiver Operating Characteristic (ROC) curve describes the signal/background binary classifier system as

from MC simulations for realistic runs

the simulated solar  $\nu_e$  events are tagged as signals and mixed with  $^{214}\text{Bi}$  background events. The total dataset was divided into training and testing sets.

with discrimination threshold values.

Area Under Curve (AUC) 0.92 energy cuts combining with NHit cuts

6 variables used as inputs

$\text{itr}$ ,  $\theta_{ij}$ ,  $\beta_{14}$ ,  $N\text{Hits}$ , energy and  $\hat{u} \cdot \hat{R}$ .

MC simulations  
 solar  $\nu_e$  and  $^{214}\text{Bi}$  backgrounds  
 The distribution of  $\cos \theta_{\text{sun}}$

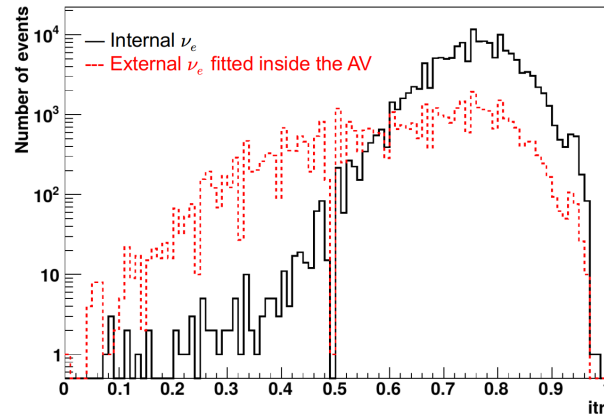


Figure 5.25: Comparison between solar  $\nu_e$  and external solar  $\nu_e$ ; MPW results.

other packages developed for high energy particle physics, such as StatPatternRecognition (SPR)[152], can be considered as an alternative tool or as a reference for results comparisons.

# Chapter 6

## Towards the SNO+ Future Phases

### 6.1 Partial-fill Phase Analysis

During the August to October 2019, the PPO is added into the LAB when the water level was at 5100 mm (in PSUP coordinate). This is one of the stages of the partial-fill phase.

As mentioned in Chapter 3, the main purpose of the partial-fill phase is to identify the background level of the liquid scintillator.  $^{16}\text{N}$  and *AmBe* calibration sources were also deployed in the external water to test the response of the detector.

During the filling, the LAB was first filled into the AV to replace the water. PPO was later mixed with LAB and added into the AV. At some stage, the PPO concentration was kept at 0.53 g/L, which was lower than the nominal 2 g/L. At the lower PPO concentration, the liquid scintillator has a slower timing profile. This also brings an opportunity to extract the Cherenkov signals from the liquid scintillator with low PPO concentration.

#### 6.1.1 High Level Cuts: Sky-shine Classifier

During the partial-fill phase, a Sky-shine classifier was suggested by Mark Chen and developed by Jeff Tseng to discriminate the noise events coming from the top of the detector, the so-called “sky shine” events, from other backgrounds events in the AV detection region[17]. These sky shine events are mostly the backgrounds from radioactive decays happening in

the neck region.

For an event happens in the neck region, it can trigger more PMTs in the bottom (or the lower hemisphere) of the PSUP sphere than in the higher hemisphere, as illustrated in Fig. 6.1. The classifier counts the number of the triggered PMTs with  $z_{PMT} < -1000 \text{ mm}$  (in PSUP coordinate) as  $nSignal$  and the number of the ones with  $-1000 < z_{PMT} < 8000 \text{ mm}$  as  $nSide$ . The ratio  $skyShine = nSide/nSignal$  is the output value of the classifier. Meanwhile, the classifier also saves the counts of the triggered neck PMTs ( $nNeck$ ) as well as the triggered outward looking (OWL) PMTs in high z positions with  $z_{OWL} > 8000 \text{ mm}$  ( $nOWL$ ).

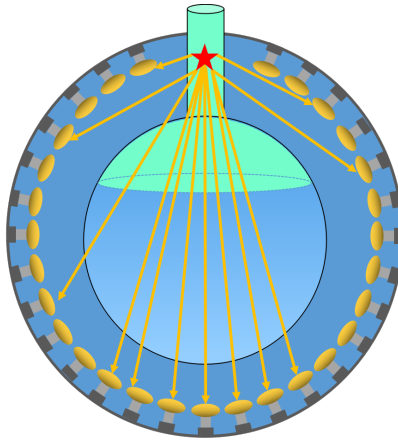


Figure 6.1: An illustration for the Sky-shine classifier, modified from [17].

In the following, I studied the performance of the Sky-shine classifier and attempted to obtain an optimized cut on the value of  $skyShine$  based on the MC simulations.

### Performance of the Sky-shine Classifier

The MC simulations of the  $^{208}\text{Tl}$  decay events were produced in a partial-fill geometry with the water level set at 4435 mm (in AV coordination) and 2 g/L PPO concentration. The  $^{208}\text{Tl}$  decay events were distributed uniformly in the scintillator region. 4067 events of  $^{208}\text{Tl}$  decays were simulated (about 16 times the expected number of events per year based on the SNO+ background evaluations[108]) and 3784 events were triggered. RAT version 6.16.9

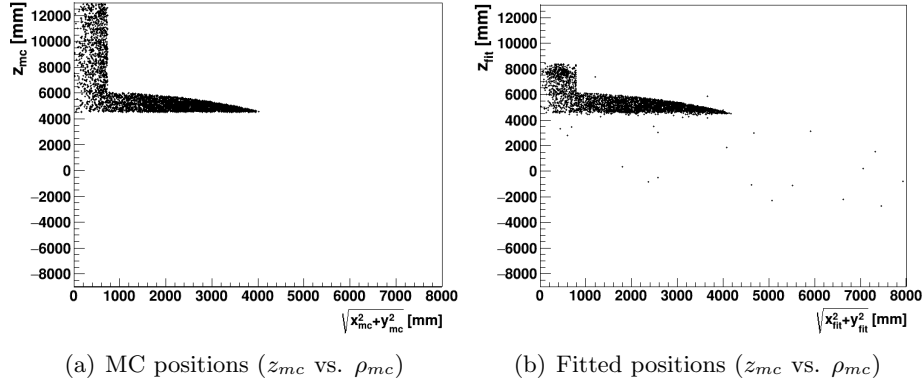


Figure 6.2: MC (left) and fitted positions (right) of  $^{208}\text{Tl}$  simulations.

was used.

Fig. 6.2 shows the positions of the simulated events and the fitted events. In the MC simulations, events are distributed in the AV as well as the whole region of the neck. Recall that the neck of the detector is 8-m tall, the MC simulated neck events from  $z_{neck, bottom} = 6108 \text{ mm}$  up to about  $z_{neck, top} = 13000 \text{ mm}$  in the PSUP coordinate. The valid reconstruction region is inside the PSUP sphere, thus only a small fraction of the neck events in the volume of the neck cylinder inside the PSUP sphere can be fitted or even be triggered.

The plots shows events with small values of Sky-shine calculations can be tagged as neck events.

By checking the MC events positions (“true” event positions), for all the triggered events, 16.8% of them are outside the AV. Apply skyShine<sub>>1.7</sub> can remove 98.6% of the events outside the AV (mostly in the neck) with a sacrifice of 0.2% of the events inside the AV.

### Optimize the Sky-shine Cuts

Since the Sky-shine classifier removes neck events (most of them are outside the PSUP) which are not properly fitted, a skyShine cut can reduce the fit biases and improve the fit resolution.

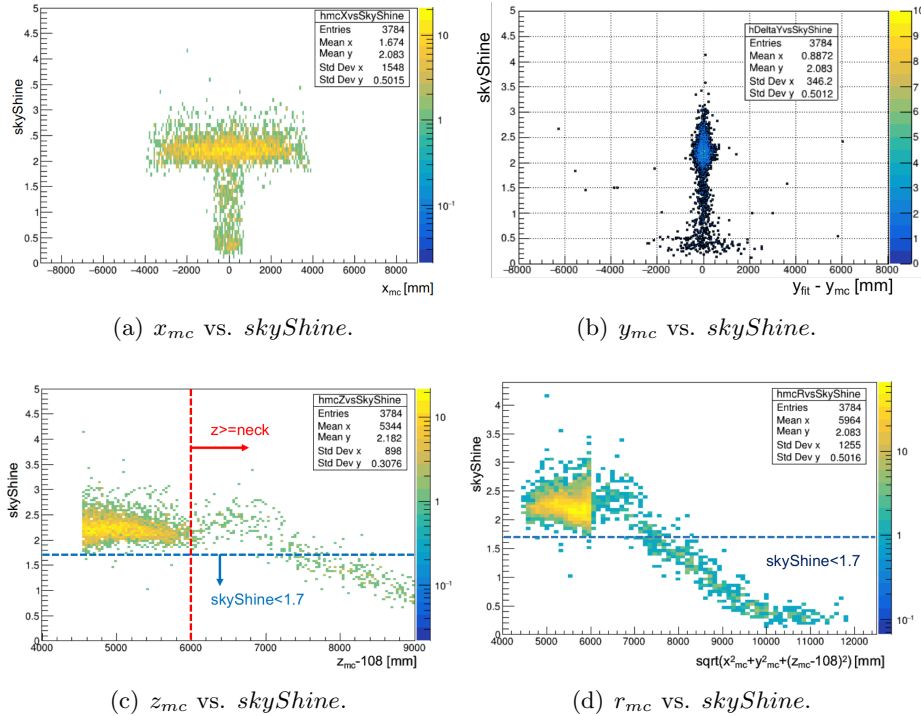


Figure 6.3: MC positions vs. skyShine values for simulated  $^{208}\text{Tl}$  events.

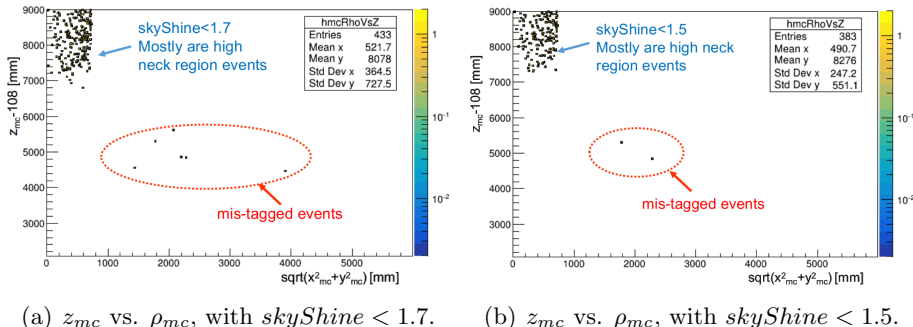


Figure 6.4: MC positions after Sky-shine cuts ( $skyShine < 1.7$  and  $skyShine < 1.5$ ) for simulated  $^{208}\text{Tl}$  events. It shows that most of the events with small  $skyShine$  values are located in the neck region while very few events in the FV region can be mis-tagged.

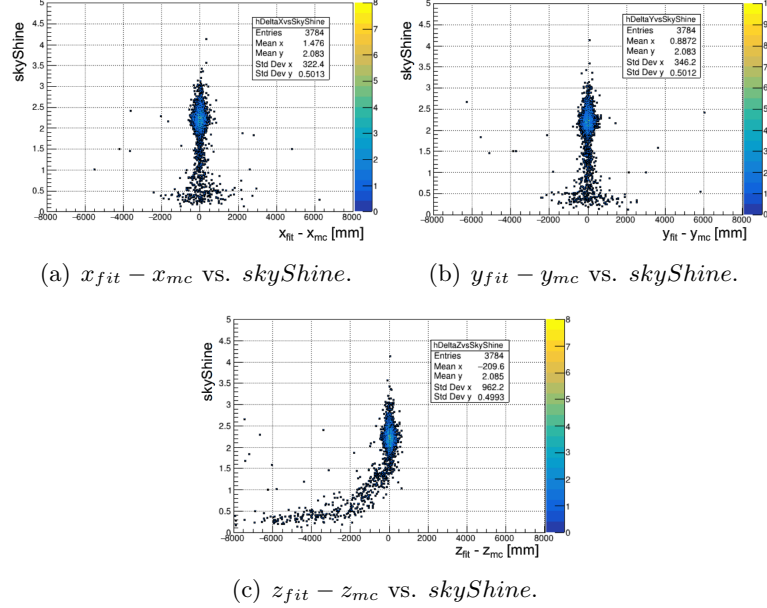


Figure 6.5: Fit biases vs.  $skyShine$  values for simulated  $^{208}\text{Tl}$  events.

$skyShine$  vs. fit biases ( $^{208}\text{Tl}$ )

An improvement of  $\sim 18$  mm in z resolution.

Apply different cuts of  $skyShine$ :  $skyShine > 1, 1.01, 2.0$ , begins from 1.0 with a 0.01 step until 2.0. Plot the x bias  $x_{fit} - x_{mc}$  versus the  $skyShine$  cut values.

Fit a gaussian to  $x_{fit} - x_{mc}$  and get  $\sigma_x$ , Do the same thing to the  $y_{fit} - y_{mc}$ ,  $z_{fit} - z_{mc}$  and obtain  $\sigma_x, \sigma_y, \sigma_z$  Fill a 1D histogram of Sky-shine cut and  $\Delta R = \sqrt{\sigma_x^2 + \sigma_y^2 + \sigma_z^2}$

Compare to the number of MC events inside the scintillator  $\sqrt{(x^2 + y^2 + (z - 108)^2)} < 6005$  mm &  $z - 108 < 6000$  mm, number of MC events/number fitted events after cut:  $skyShine > 1.6$ : 3149/3376  $skyShine > 1.7$ : 3149/3351 Can check with more productions/higher statistics.

### 6.1.2 Different PPO Concentrations during the Filling

Oxford group in the SNO+ collaboration has done a few bench-top measurements for the time constants and relative light yields of LAB mixed with different concentrations of PPO[18].

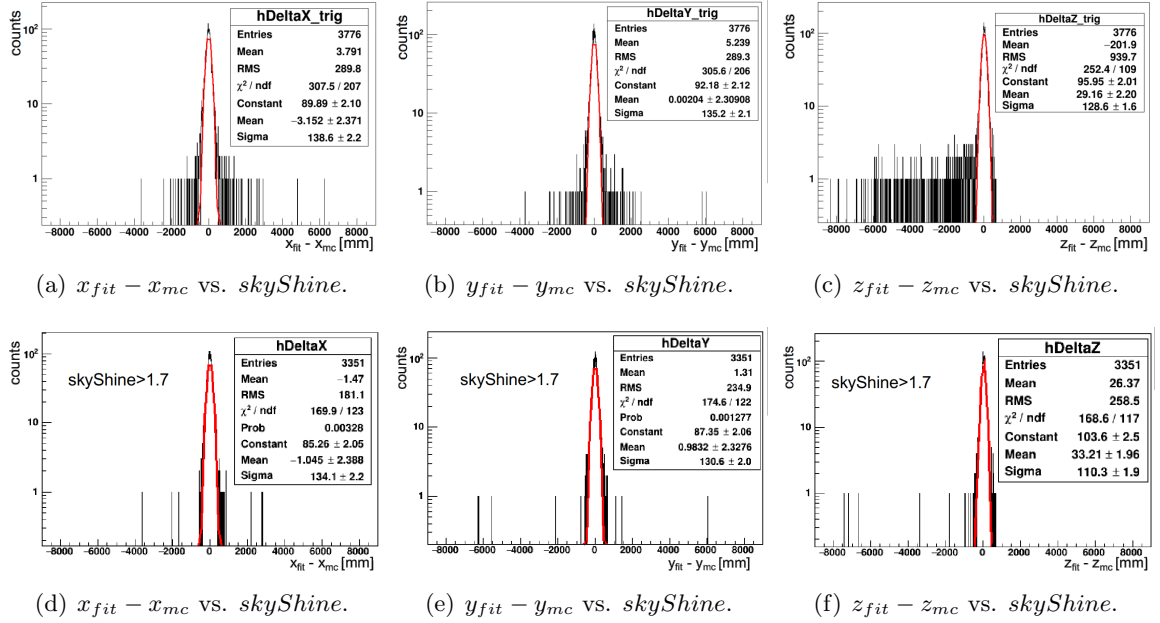
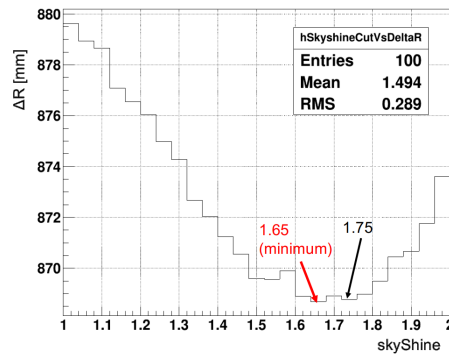
Figure 6.6: Fit biases vs. skyShine values for simulated  $^{208}\text{Tl}$  events.

Figure 6.7: Radial resolutions with different skyShine cuts.

The emission time profiles and relative light yields of PPO dissolved in LAB at the following concentrations: 0.25, 0.5, 1.0, 2.0 and 6.0 g/l.

The partial fitter is re-coordinated according to these measurements.

Table 6.1: time constants and amplitudes measured by Oxford group [18].

PPO [g/L]	$\tau_{rise}$ [ns]	$\tau_1$ [ns]	$\tau_2$ [ns]	$\tau_3$ [ns]	$A_1$ [%]	$A_2$ [%]	$A_3$ [%]	$A'$ [%]
0.25	1.25	8.1	25.0	68.2	29.2	53.1	13.9	3.8
0.5	1.12	7.2	18.7	49.1	43.5	40.4	12.6	3.5
1.0	1.18	5.5	13.3	40.9	45.6	37.5	13.3	3.6
2.0	1.06	4.2	11.7	48.9	57.9	27.8	8.9	5.4
6.0	0.94	2.5	9.3	46.0	63.7	17.0	8.6	10.7

$$\sum_{i=1}^3 \left( A_i \frac{e^{-\frac{t}{\tau_i}} - e^{-\frac{t}{\tau_{rise}}}}{\tau_i - \tau_{rise}} \right) + A' \frac{e^{-\frac{t}{\tau_{rise}}}}{\tau_{rise}}$$

based on these measured parameters, pdfs were built.

relative light yield (2g/L = 11900)

Table 6.2: Relative light yield (RLY) measured by [18].

PPO [g/L]	RLY
0.25	0.57
0.5	0.65
1.0	0.9
2.0	1.0
6.0	0.93

The partial fitter is robust with changes of time profile pdfs.

radial biases

Table 6.3: Tuned effective group velocities for different PPO concentrations.

PPO [g/L]	$V_{gr,scint}$ [mm/ns]	$n_{scint}$	$V_{gr,water}$ [mm/ns]	$n_{water,tuned}$
0.25	$184.068 \pm 5.153$	1.629	$211.871 \pm 5.731$	1.415
0.5	$183.467 \pm 5.159$	1.634	$211.587 \pm 5.773$	1.417
1.0	$182.93 \pm 5.193$	1.639	$211.393 \pm 5.805$	1.418
2.0	$183.045 \pm 5.184$	1.638	$211.629 \pm 5.767$	1.417
6.0	$184.218 \pm 5.135$	1.627	$211.173 \pm 5.843$	1.420

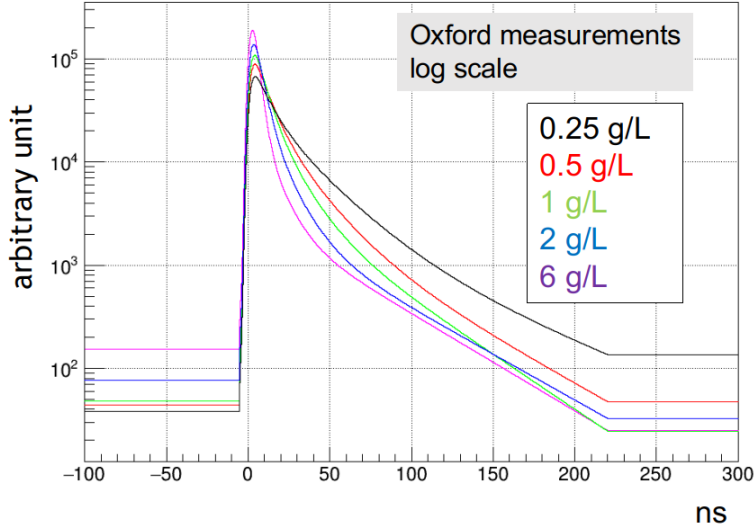


Figure 6.8: Timing spectrum for different PPO concentrations based on the Oxford bench-top measurements.

Simulate 5000 events for 3 MeV  $e^-$ ,

$$\Delta x = x_{fit} - x_{mc}$$

Table 6.4: Fit speeds and biases for various PPO concentrations.

PPO [g/L]	fit speed [s/event]	$\Delta x$ [mm]	$\Delta y$ [mm]	$\Delta z$ [mm]	$r_{bias}$ [mm]
0.25	0.190	6.65	2.64	-18.24	-7.22
0.5	0.144	-0.73	-1.69	-8.14	3.30
1.0	0.190	1.42	0.57	-5.65	10.67
2.0	0.194	0.34	1.78	-4.01	13.37
6.0	0.145	-0.11	-0.12	-25.97	-10.97

$z_{fit}$  resolution [mm]

fit with wrong PPO concentrations:

PPO in Fitter configuration

### 6.1.3 Bi-Po Analysis

### 6.1.4 $^{16}\text{N}$ Calibration Calibration in the Partial-fill Phase

water level was at 5100 mm from the center of the AV (in AV coordination). LAB with a PPO concentration of 0.53 g/L

Table 6.5: Fit speeds and biases for various PPO concentrations.

PPO [g/L]	$\Delta x$	$\Delta y$	$\Delta z$	$\sigma_z$	$r_{bias}$	$\sigma_r$	ratio in FV (%)
0.25	6.80	2.90	-14.61	121.6	-4.82	120.3	93.70%
0.5	5.15	2.82	-12.85	120.2	1.34	123.0	93.46%
1.0	2.32	1.95	-13.22	120.3	0.344	121.9	93.78%
2.0	5.76	3.03	-9.61	119.3	7.264	125.1	93.26%

Effect of the water level.

The  $^{16}\text{N}$  source was deployed in the external water region during the partial-fill phase. run 251748 2019/09/19 and

Source position was at  $(-1120.8, 1041.4, 6172.5) \text{ mm}$  for a 30-minute duration and at  $(-1120.8, 1041.4, 6108.0) \text{ mm}$  for a 7-hour duration (separated into 7 runs).

### 6.1.5 Extracting the Cherenkov Signals in Partial-fill Phase

For an event happens in liquid scintillator, the number of Cherenkov photons it created is only  $\sim 5\%$  of the total photon numbers, which is a very small fraction compared to the number of scintillation photons. This causes the directional Cherenkov signals are submerged in the isotropic lights.

Since the  $^{16}\text{N}$  source provides high energy events around 6 MeV,

a time cut window on the time residual was optimized for the searching based on MC. simulations in pure scintillator phase.

In the case that  $e^-$  are generated uniformly and isotropically in the detector, to enhance the Cherenkov ring pattern, a transformation is applied as following:

$$\phi = \arccos(\hat{\vec{u}}_e \cdot \hat{\vec{u}}_{assume})$$

$$\vec{n} = \hat{\vec{u}}_e \times \hat{\vec{u}}_{assume}$$

$$R = \begin{bmatrix} n_x^2(1 - \cos \phi) + \cos \phi & n_x n_y(1 - \cos \phi) - n_z \sin \phi & n_x n_z(1 - \cos \phi) + n_y \sin \phi \\ n_x n_y(1 - \cos \phi) + n_z \sin \phi & n_y^2(1 - \cos \phi) + \cos \phi & n_y n_z(1 - \cos \phi) - n_x \sin \phi \\ n_x n_z(1 - \cos \phi) - n_y \sin \phi & n_y n_z(1 - \cos \phi) + n_x \sin \phi & n_z^2(1 - \cos \phi) + \cos \phi \end{bmatrix}$$

$$\vec{u}'_e = R \vec{u}_e$$

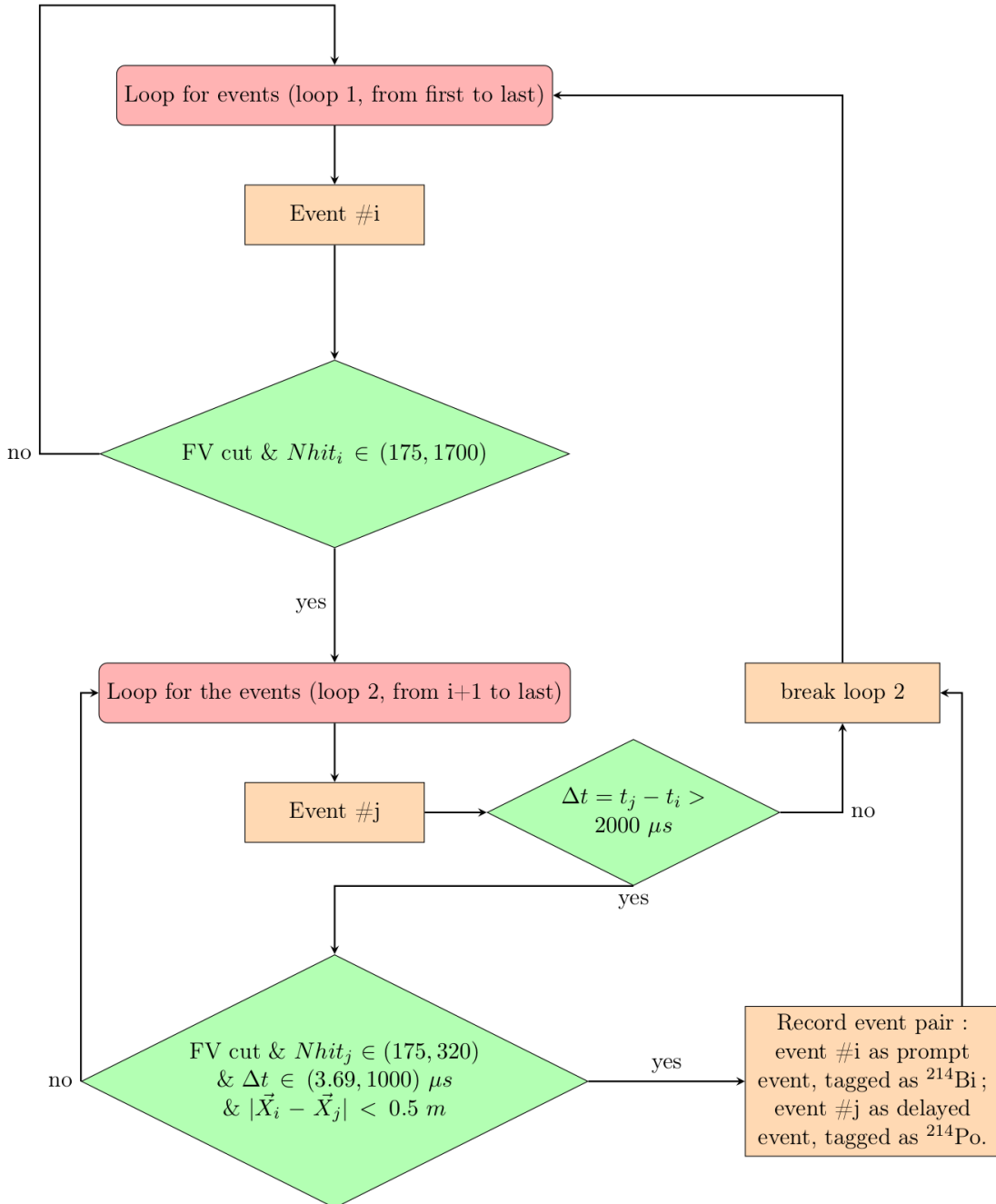


Figure 6.9: A flow chart for Bi-Po tagging.

$$\vec{X}'_{evt} = R\vec{X}_{evt}$$

Move  $\vec{X}'_{evt}$  to the origin,

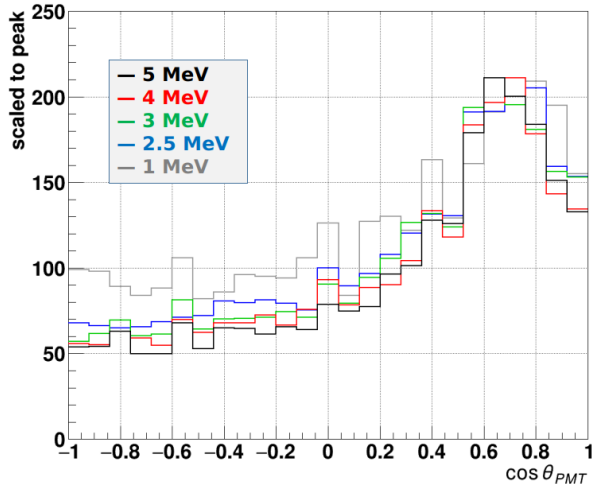


Figure 6.10: Distributions of  $\cos \theta_{PMT}$  after the prompt time cut for various  $e^-$  energies simulations.

$$\vec{X}'_{pmt} = R\vec{X}_{pmt} - \vec{X}'_{evt}$$

Turning off the Cherenkov process in the Monte Carlo simulations.

Breit-Wigner function

$$p(x) = \frac{c_0}{\pi} \frac{\frac{1}{2}\Gamma}{(x - m)^2 + (\frac{1}{2}\Gamma)^2} + c_1$$

### *AmBe* Source Analysis

The *AmBe* source

## 6.2 Towards the Te-loaded Phase

### 6.2.1 Muon Induced Backgrounds in the Te-loaded Phase

This analysis is

based on the work

\* These data are taken from [122].

\* These data are taken from [122].

To simulate these backgrounds, the optics for 0.3 % Te by weight and with *bisMSB* (*te\_0p3\_labppo\_scintillator\_bisMSB\_Feb2015*) and RAT-5.2.3 were used.

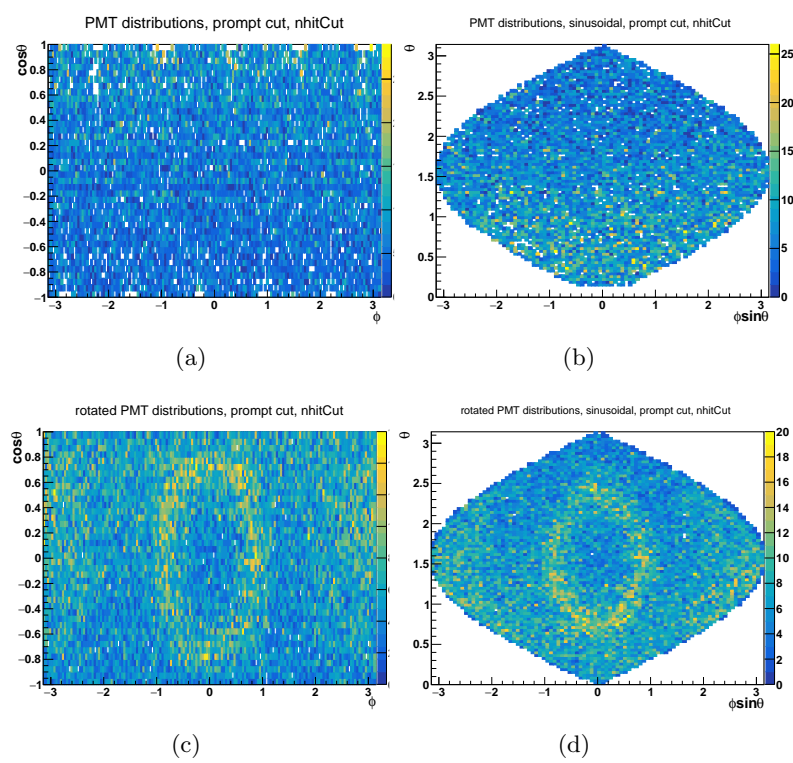


Figure 6.11: PMT hit patterns after the prompt time cut and NHit cut.

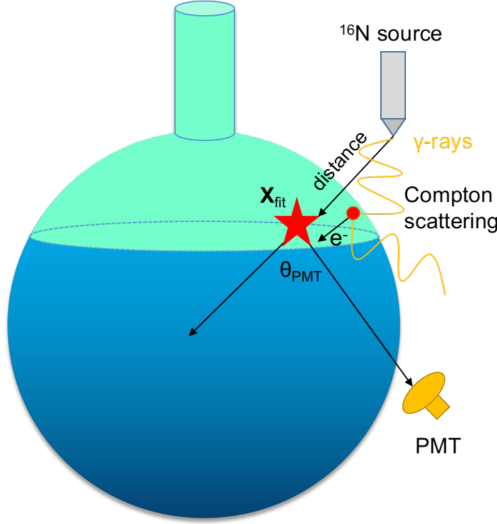


Figure 6.12:  $^{16}\text{N}$  source calibration in external water during the partial-fill phase.

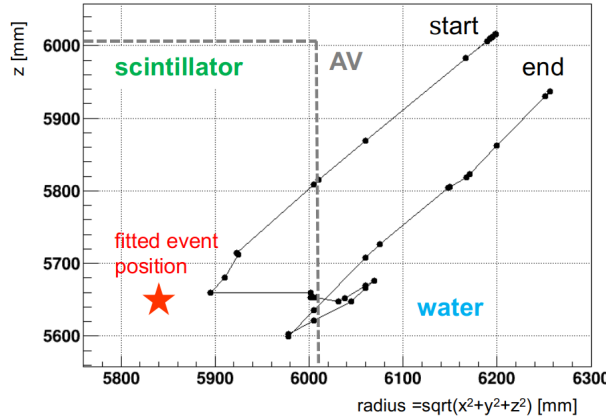


Figure 6.13: Simulated main track of 7.1 MeV  $\gamma$  for one event from  $^{16}\text{N}$  source in the external water during the partial-fill phase.

I looked into 10000 simulations of the cosmic muon induced  $^{11}\text{C}$ ,  $^{10}\text{C}$  and  $^{6}\text{He}$  backgrounds events. Each simulation runs for one year duration.

Fig. 6.14, Fig. 6.15 and Fig. 6.16 show the spectrum of the Monte Carlo energies (mc Edep quenched) scaled from 10000 simulations (left) and the scaled spectrum of the reconstructed energies (right) for one year duration and one kilo-tonne of the cocktail. The fiducial volume (FV) cuts of 5.5-m, 4.5-m, 3.5-m are applied.

The Monte Carlo results give a total  $^{11}\text{C}$  background rate of  $1063.55 \text{ kt}^{-1}\text{yr}^{-1}$  with-

Table 6.6: Cosmic muon induced isotopes production rates  $R_i [kt^{-1}yr^1]$ .

isotopes	NA54 mean		NA54 distr. solar	KamLAND		Borexino	
	solar	Te		solar	Te	solar	Te
<sup>11</sup> C	559.72±55.81	524.34±52.28	190±33	1135.1±206.21	1063.34±193.17	1048±121	981.75±113.35
<sup>12</sup> B	—	—	—	59.94±5.41	56.15±5.07	69±3	65±3
<sup>11</sup> Be	1.45±0.11	1.36±0.10	—	1.50±0.35	1.41±0.33	< 8.5	< 7.96
<sup>11</sup> Li	—	—	—	—	—	—	—
<sup>8</sup> Li	2.49±0.92	2.33±0.86	1±1	15.64±3.47	14.65±2.35	8±7	7±7
<sup>8</sup> He ( <sup>8</sup> He+ <sup>9</sup> Li)	1.31±0.24	1.23±0.22	—	1.13±0.57	1.05±0.53	< 1.9	< 1.8
<sup>9</sup> Li	—	—	—	3.04±0.34	2.85±0.32	3.6±0.3	3.4±0.3
<sup>6</sup> He	9.91±1.25	9.28±1.17	3±1	—	—	46±16	43±15
<sup>10</sup> C	71.37±10.55	66.86±9.88	24±6	22.63±2.73	21.20±2.56	22±5	21±5
<sup>9</sup> C	2.99±0.96	2.80±0.90	—	4.09±1.65	3.83±1.55	< 19.3	< 18.1
<sup>8</sup> B	4.41±0.96	4.13±0.90	2±1	10.05±2.86	9.41±2.68	16±6	15±6
<sup>7</sup> Be	142.25±17.90	133.26±16.77	55±15	—	—	—	—
<sup>12</sup> N	—	—	—	—	—	< 1.88	< 1.76

Table 6.7: Decay information of the isotopes.

isotope	half-life	Q-value	Decay mode
<sup>11</sup> C	20.334 min	0.96 MeV	<sup>11</sup> C→ <sup>11</sup> B+e <sup>+</sup> +ν <sub>e</sub>
<sup>10</sup> C	19.308 s	3.65 MeV	<sup>10</sup> C→ <sup>10</sup> B+e <sup>+</sup> +ν <sub>e</sub>
<sup>6</sup> He	806.7 ms	3.51 MeV	<sup>6</sup> He→ <sup>6</sup> Li+e <sup>-</sup> +ν <sub>e</sub>

out cuts,  $21.39 \text{ kt}^{-1}\text{yr}^{-1}$  for  $^{10}\text{C}$  and  $43.31 \text{ kt}^{-1}\text{yr}^{-1}$  for  $^6\text{He}$ . From results of the reconstructed energies, a total background rate of  $989.17 \text{ kt}^{-1}\text{yr}^{-1}$  for  $^{11}\text{C}$  is evaluated while  $20.06 \text{ kt}^{-1}\text{yr}^{-1}$  for  $^{10}\text{C}$  and  $40.07 \text{ kt}^{-1}\text{yr}^{-1}$  for  $^6\text{He}$ .

For the region of interest (ROI) of the  $^{130}\text{Te}$   $0\nu\beta\beta$  search, we defined the ROI windows by simulating 10000 events of  $0\nu\beta\beta$ , fitting the  $0\nu\beta\beta$  signal peak with Gaussian function and taking the  $-0.5\sigma$  to  $1.5\sigma$  region around the Gaussian signal peak. The ROI window of [2.47, 2.70] MeV taken from [89] is also checked. From both results of the Monte Carlo and reconstruction, after the 5.5-m FV cut, no events of  $^{11}\text{C}$  backgrounds in the ROI are expected; after the 3.5-m FV cut, the event rates of  $^{10}\text{C}$  and  $^6\text{He}$  are below  $1 \text{ kt}^{-1}\text{yr}^{-1}$  in the ROI. Among these three backgrounds, the  $^{10}\text{C}$  has the highest event rates in the ROIs. The event rates for these three isotopes backgrounds with different FV cuts and different ROI windows are summarized in Table 6.9. The values obtained from the Monte Carlo simulations are listed in the “MC” column and from the reconstruction are listed in the “Recon” column.

In addition, the muon-induced  $^{11}\text{C}$ ,  $^{10}\text{C}$  and  $^6\text{He}$  backgrounds in the solar phase are

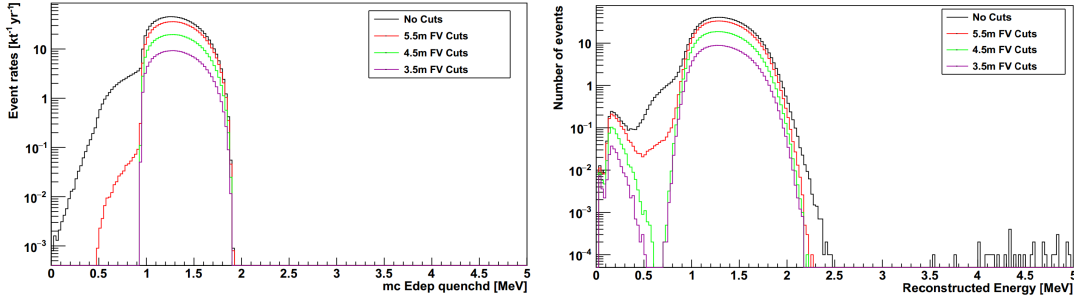


Figure 6.14: Energy spectrum of cosmic muon induced  $^{11}\text{C}$  backgrounds in SNO+ Te-loaded phase for one year duration. Left: Monte Carlo energy distributions. Right: Reconstructed energy distributions.

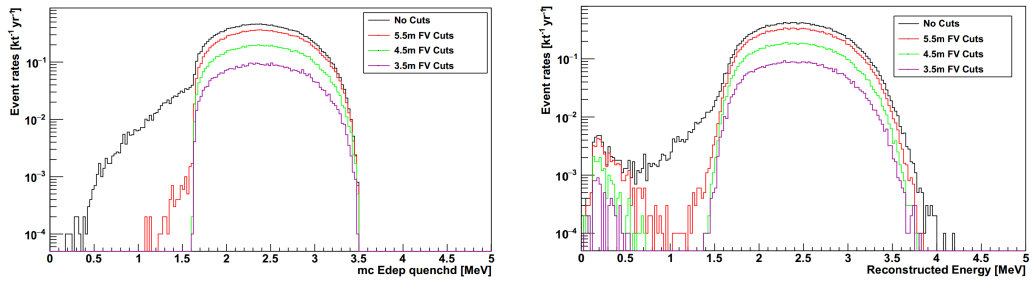


Figure 6.15: Energy spectrum of cosmic muon induced  $^{10}\text{C}$  backgrounds in SNO+ Te-loaded phase for one year duration. Left: Monte Carlo energy distributions. Right: Reconstructed energy distributions.

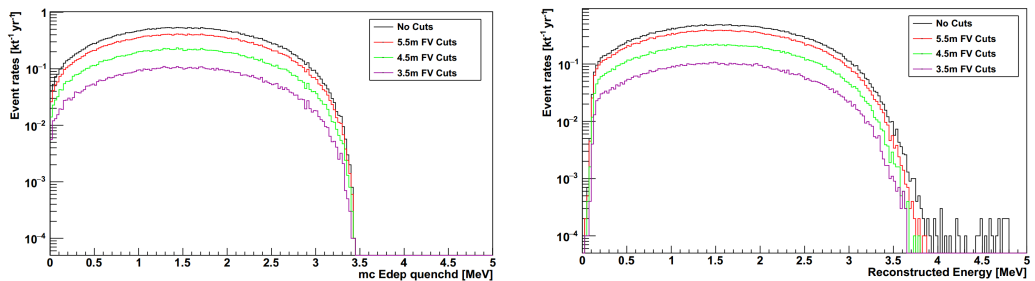


Figure 6.16: Energy spectrum of cosmic muon induced  $^6\text{He}$  backgrounds in SNO+ Te-loaded phase for one year duration. Left: Monte Carlo energy distributions. Right: Reconstructed energy distributions.

Table 6.8: Production rates for  $^{11}\text{C}$ ,  $^{10}\text{C}$  and  $^6\text{He}$  backgrounds in SNO+ Te-loaded Phase.

isotope	rates [ $kt^{-1} \cdot yr^{-1}$ ]	rates [Hz]
$^{11}\text{C}$	1063.34	0.00003372
$^{10}\text{C}$	21.20	0.0000006722
$^6\text{He}$	43.09	0.0000013663

Table 6.9: Event rates of cosmic muon induced  $^{11}\text{C}$ ,  $^{10}\text{C}$  and  $^6\text{He}$  backgrounds in SNO+ Te-loaded Phase (unit:  $kt^{-1} \cdot yr^{-1}$ ). Different fiducial volume (FV) cuts and ROI region cuts are applied. The “MC” Column presents the values obtained from the Monte Carlo and the “Recon.” column presents the values obtained from the reconstructed energies.

FV cuts	ROI [MeV]	$^{11}\text{C}$		$^{10}\text{C}$		$^6\text{He}$	
		MC	Recon.	MC	Recon.	MC	Recon.
No cuts	all regions	1063.55	989.17	21.39	20.06	43.31	40.07
	[2.47, 2.70]	0	1	4.52	4.31	2.78	2.88
	[2.492, 2.737]	0	0	4.44	4.25	2.67	2.79
5.5-m	all regions	807.06	786.81	16.24	15.72	32.92	32.04
	[2.47, 2.70]	0	0	3.63	3.45	2.13	2.25
	[2.487, 2.711]	0	0	3.28	3.12	1.90	2.00
4.5-m	all regions	442.00	437.00	8.87	8.72	18.04	17.83
	[2.47, 2.70]	0	0	2.00	1.92	1.16	1.23
	[2.477, 2.692]	0	0	1.64	1.57	0.95	1.01
3.5-m	all regions	207.84	206.34	4.20	4.16	8.47	8.42
	[2.47, 2.70]	0	0	0.95	0.92	0.54	0.57
	[2.477, 2.688]	0	0	0.78	0.76	0.44	0.46

also checked. Fig. 6.17 to Fig. 6.19 show the scaled spectrum from 10000 simulations of these background events in the solar phase for 1 year duration. The total event rates are summarized in Table. 6.10.

### 6.2.2 Relative Light Yield Measurements of the Te-loaded Liquid Scintillators

As described in Chapter 3, the energies of charged particles are converted into photons by the scintillator medium. By measuring the amount of the light, the energy of the particle from a certain process can be inferred. To measure the summed energy spectrum of the two electrons is the major task for a particle physics experiment searching for the possible

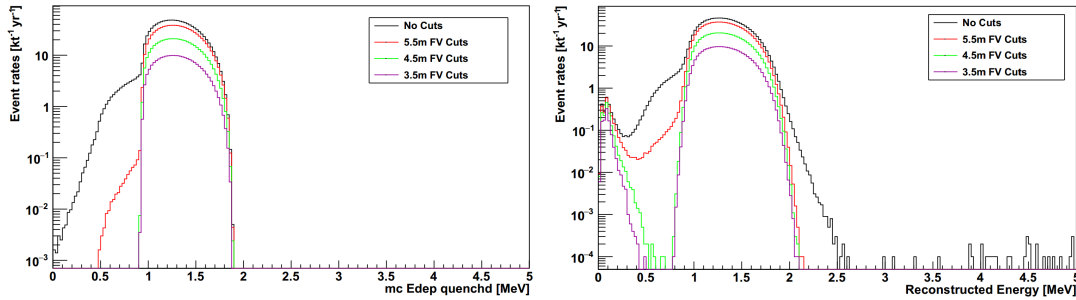


Figure 6.17: Energy spectrum of cosmic muon induced  $^{11}\text{C}$  backgrounds in SNO+ solar phase for one year duration. Left: Monte Carlo energy distributions. Right: Reconstructed energy distributions.

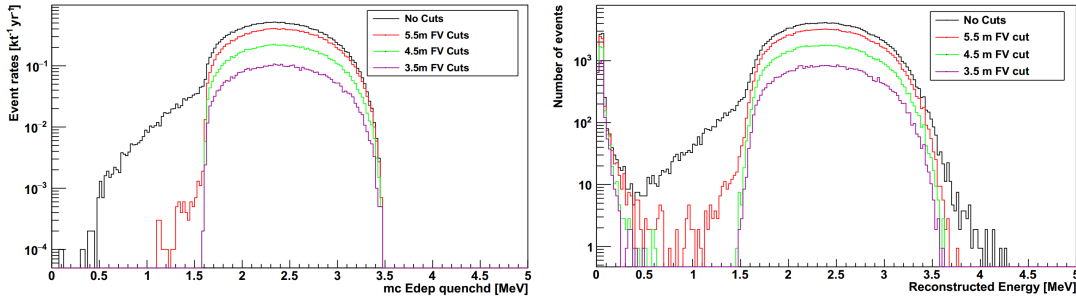


Figure 6.18: Energy spectrum of cosmic muon induced  $^{10}\text{C}$  backgrounds in SNO+ solar phase for one year duration. Left: Monte Carlo energy distributions. Right: Reconstructed energy distributions.

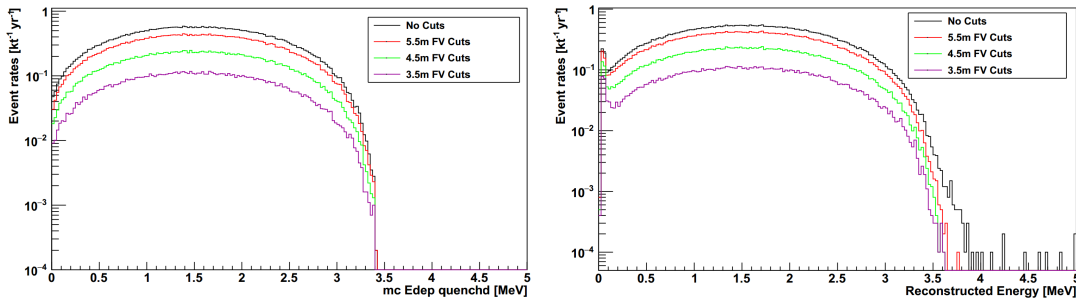


Figure 6.19: Energy spectrum of cosmic muon induced  $^{6}\text{He}$  backgrounds in SNO+ solar phase for one year duration. Left: Monte Carlo energy distributions. Right: Reconstructed energy distributions.

Table 6.10: Event rates of cosmic muon induced  $^{11}\text{C}$ ,  $^{10}\text{C}$  and  $^6\text{He}$  backgrounds in SNO+ solar phase (unit:  $\text{kt}^{-1} \cdot \text{yr}^{-1}$ ). FV Cuts ROI [MeV]  $^{11}\text{C}$  events  $^{10}\text{C}$  events  $^6\text{He}$  events

FV cuts	ROI [MeV]	$^{11}\text{C}$		$^{10}\text{C}$		$^6\text{He}$	
		MC	Recon.	MC	Recon.	MC	Recon.
No cuts	all regions	1136.32	1107.50	24.04	23.07	46.99	45.30
5.5-m	all regions	862.32	855.56	18.20	17.64	35.64	35.25
4.5-m	all regions	472.12	470.22	9.92	9.77	19.44	19.41
3.5-m	all regions	222.05	221.94	4.63	4.66	9.17	9.24

$0\nu\beta\beta$ -decay signal.

For the  $^{130}\text{Te}$   $0\nu\beta\beta$ -decay process, the signature energy peak is at  $2.5 \text{ MeV}$ [89]. This peak is relatively small and can be immersed in the ubiquitous radioactive decays from natural sources, such as the natural Uranium and thorium decay chains existing in the materials [cite whitepaper]. Therefore, the  $0\nu\beta\beta$ -decay experiments require a very high energy resolution to distinguish the signal from the backgrounds. For the liquid scintillator, it is expected to create as large amount of light caused by a particle interaction as possible. A quantity of light yield, defined as the number of photons for per MeV energy deposit (photons/MeV) by a particle interaction, is used for describing the detection property of the liquid scintillator.

Here we measured the light yield of 0.5% Tellurium loaded LAB (TeLS) samples relative to the LAB-PPO scintillator (relative light yield, RLT). With tellurium loading into the LAB, the light yield of the liquid scintillator will go down since the tellurium atoms can block the photon transmissions to the photosensors. The light yield of the TeLS is crucial for the  $0\nu\beta\beta$ -decay experiments since it determines the energy resolution. It is also crucial for the experiments that are aimed to develop high light yield Tellurium-loaded scintillators [153].

### 6.2.3 Measurement Setup and Data Acquisition

We first prepared LAB+2 g/L PPO by dissolving PPO into the pure LAB. The LAB-PPO mixture was distilled by heating and flowing with liquid nitrogen to remove humidity and

oxygen, which can affect the light yield, for 48 hours. The distilled LAB-PPO was added into the original 16.5% weight Te-butanediol samples to dilute into the 0.5% TeLS samples. Te-butanediol samples from both of the DDA and SOP synthesis procedures are prepared and are referred as TeDDA and TeSOP samples respectively. These samples are further transferred into scintillation vials for the measurement. These vials have PTFE caps sealed on the top of the glass cylinders. To avoid air bubbles created by squeezing the vial cap into the liquid, the liquid level for each sample is kept at 30 mm. The dimensions of the vial is shown in the left picture of Fig. 6.20.

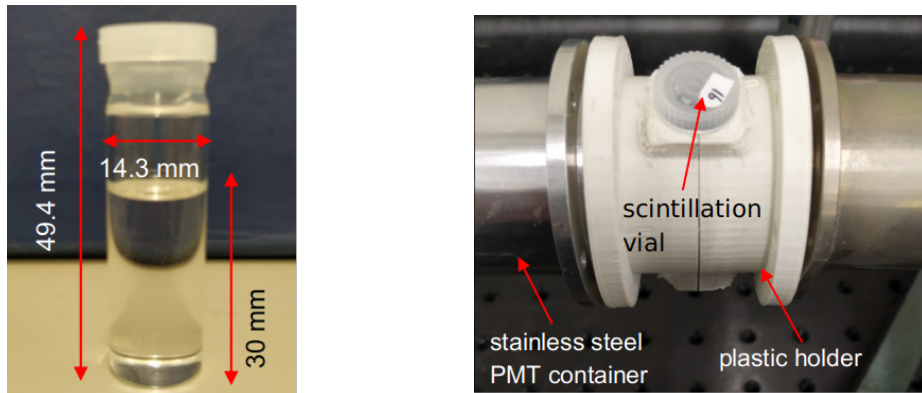


Figure 6.20: Test sample (left) and setup (right). Left: The samples were filled into scintillation vials. The dimensions are shown in the picture. Right: two PMTs are aligned to face to the scintillation vial from each side.

Two Hamamatsu R580 PMTs [cite PMT] were used for detecting the light. The diameter of the PMT round surface is 38.71 mm. These PMTs were housed in stainless steel cylinders (PMT holders), set face to face, looking at the scintillation vial from each side. The PMTs and the vial were aligned by a plastic piece, as shown in the right picture in Fig. 12. The plastic piece is in a cylindrical shape with a hole on the top to plug in the scintillation vial and a slot at the bottom to attach a radioactive source. Inside the cylinder, there is a button-shaped groove at the bottom to fix the vial plugged in and keep the vial upright. Also, a 2-mm-diameter hole was drilled at the bottom of the piece to allow the radiation rays to go inside from the bottom. The surface inside was polished to reduce the absorption of the material to the photons. The piece is made of plant-based and biodegradable PLA

filament and was machined by 3D-printing facility. The pictures of the piece are shown in Fig. 13.

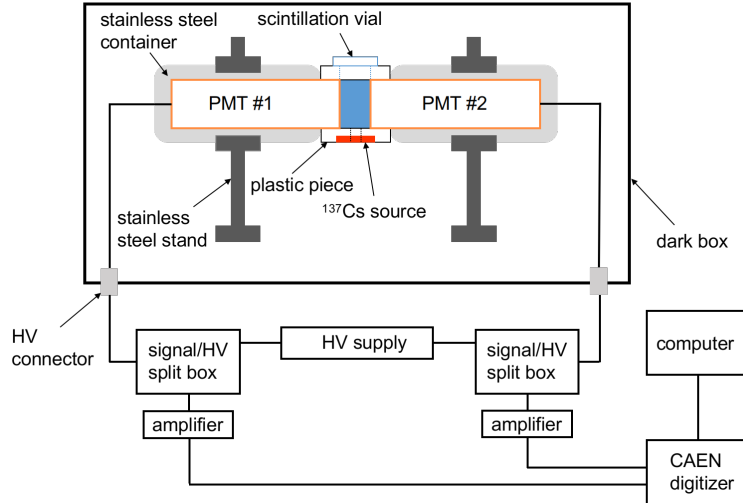


Figure 6.21: A diagram shows the light yield measurement setup. See the text for details.

Fig. 6.21 shows a diagram of the whole measurement setup. The plastic piece held the radioactive source and the scintillation vial. It also aligned two PMTs to face to the scintillation vial from each side. The piece can shield lights from outside as well. These setups were placed in a dark box to prevent the lights from lab. Two RG59/U type high voltage (HV) cables connected the PMTs to an HV supply outside the dark box. The HV cables were connected to two signal/HV split boxes to separate the HV current and electrical signals. Due to the resistor of the split box, the HV supply was set to 2200 Volts (V) for the PMT operation while the operation voltage suggested by the Hamamatsu is 1800 V.

The signal cables from the split box were connected to a two-channel Hewlett Packard (HP) amplifier. This amplifier inverted the signals and amplified them by 26 dB. The amplified signals were then input into a two-channel digitizer. The digitizer records the data and sent them to a desktop computer.

To obtain and analyze the data, we used a desktop Waveform Digitizer, the DT5751 module provided by the Costruzioni Apparecchiature Elettroniche Nucleari S.p.A (CAEN).

Running at a digital pulse processing mode, the module records the digitized PMT waveforms with a data-taking rate of 1 GHz for each channel [cite CAEN].

This module is controlled by the CoMPASS software, which is provided by CAEN. The software sets up the threshold and trigger parameters. For each triggered event which passes the threshold, the software records event time, trigger flag and waveform histograms from the two channels. By integrating the waveforms, it can also calculate the energy of a triggered event [cite compass].

Each channel recorded the signals from each PMT individually. With the two-PMT setup, we applied coincidence time mode measurements. In the coincidence mode, a coincidence time window between two channels were set to 48 ns. For a certain event, the CoMPASS software compares the event time difference between two channels and only records it if the event time differences is less than 48 ns. A smaller window of 10 ns was further applied for analysis.

Fig. 12: Test sample (left) and setup (right). Left: The samples were filled into scintillation vials. The dimensions are shown in the picture. Right: Two PMTs are aligned to face to the scintillation vial from each side.

Fig. 13. The plastic piece holds the radiation source and the scintillation vial. It also aligns the PMTs to face the vial from two sides. Fig. 14: Diagram for the light yield measurement setup. See the text for details.

#### Measurement

The liquid scintillator samples we have measured are: LAB-PPO, TeDDA, TeSOP. The unloaded LAB-PPO sample served as a standard candle.

A Cesium-137 ( $^{137}\text{Cs}$ ) radioactive source was always placed at the bottom of the scintillation vials. The source was made by Radiochemical Centre Amersham. The radioactivity measured on 1st April 1974 was 11.09 *microcurie*( $\mu\text{Ci}$ ), with an accuracy of 3.7%. The activity was expected to be in this thesis, considering a half-life of 30.08 years for the  $^{137}\text{Cs}$ [122].

has a 85.10% chance to emit 0.661 MeV  $\gamma$ -rays[122]. These  $\gamma$ -rays can travel into the

liquid scintillator samples in the vial, interact with the samples and create scintillation photon.

For each sample, measurements were taken for one-minute time duration. Waveforms from the PMT photo-current signals were digitized in a 252 ns time window. Shown in Fig. 6.22 is a typical waveform caused by  $\gamma$  rays interacted with the LAB-PPO sample. The p.e. signals triggered PMT pulses and the pulses were digitized as waveforms. For each waveform, the digitizer firmware dynamically calculated the baseline as the mean value of 256 data points inside a moving time window of 252 ns. A threshold was set as 100 units above the baseline. The data point on the 90% leading edge of the pulse was taken as the trigger time tag. From this trigger time tag, in the following 80 ns window the digitizer did not calculate another trigger to avoid introducing another pulse (trigger hold-off). Also from the trigger time tag, a pre-gate of 8 ns was set. The waveform was integrated in the time gate of [trigger time - 8, trigger time + 72] ns. This gives the integrated charge, which was calculated as a A/D converter (ADC) channel number. If the measurement system can be calibrated, the ADC channel number can be exactly converted into the energy of the particle interaction. Since here we only interested in the photon numbers, we simply used ADC channel as the energy. Once the pulse in the waveform passed the threshold and a triggered time tag can be found, the digitizer considered it as a triggered event. A time flow started when the measurement began. Time stamps were recorded as event time when the triggered event hapfpened. The waveform was recorded and the ADC channel number (energy) of this event was calculated.

In a coincidence time measurement, the event times of the events recorded by each of the two PMTs were compared. If the event time differences between two events from each PMTs were too long, these two events were considered as random noises rather than the physics events and were not recorded. We optimized a coincidence time cut as 40 ns and set that cut during the digitizer data-taking.

Fig. 6.23 shows the measured LAB-PPO energy spectrum with and without coincidence time cut (10 ns) on the ADC channel 0. Without the coincidence time cut, there exists a

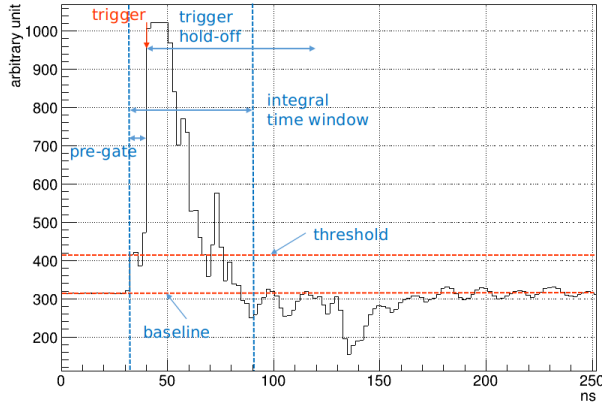


Figure 6.22: A typical waveform triggered by scintillation photons from  $^{137}\text{Cs}$   $\gamma$ -rays interaction with LAB-PPO sample.

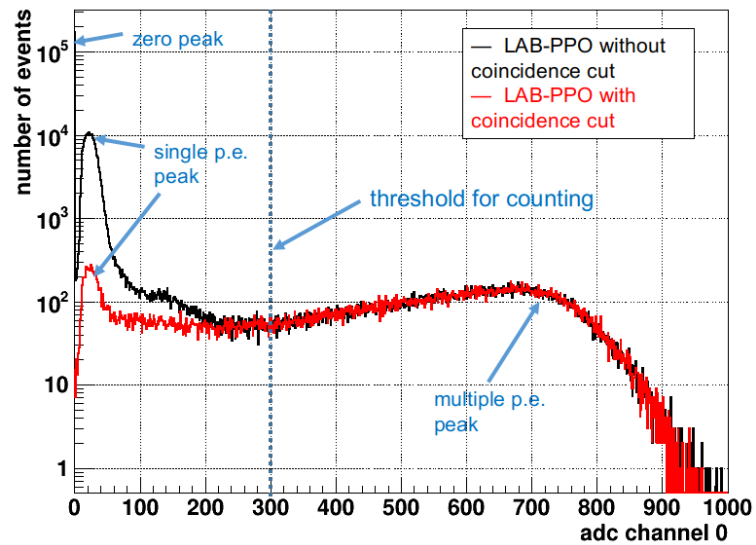


Figure 6.23: Measured LAB-PPO energy spectrum with and without coincidence cut on the ADC channel 0. A threshold for counting is set by comparing the two spectrum.

zero peak, which is caused by the pulses from random electronic noises or fluctuations of the digitized waveforms. The peak on the left is the single p.e. peak. It is mainly caused by some light sources which are weak enough that the photons only strike out at most one single p.e. inside the PMT [cite leo]. The peak on the right is the multiple p.e. peak, in our case is mainly caused by a number of scintillation photons produced by the  $\gamma$ -ray interacting with the LAB-PPO. In the coincidence time measurement mode, it only records the photons detected by the two PMTs almost simultaneously. Therefore, the zero peak is removed while the single p.e. peak is suppressed. The multiple p.e. peak is consistent with the non-coincidence measurement. A threshold in energy can be set to count only the scintillation photons emitted from LAB-PPO.

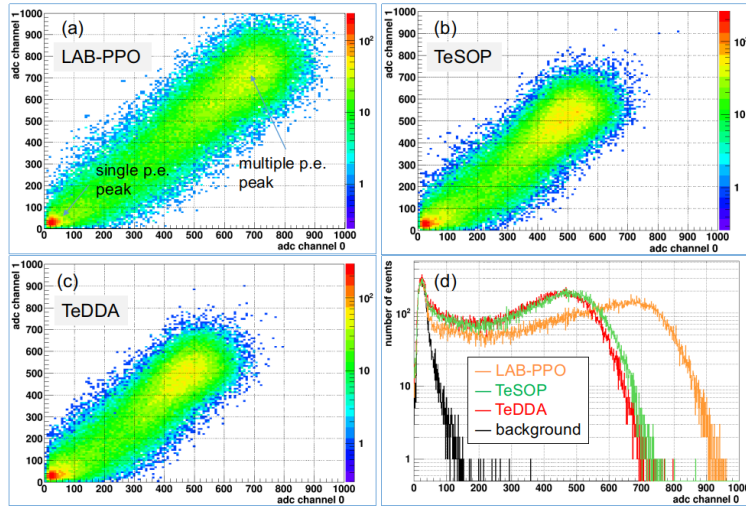


Figure 6.24: 2D energy spectrum of the counting measurements of LAB-PPO (a), TeSOP (b), and TeDDA (c) samples, projected the 2D plots into one channel (d). The single photo-electron (p.e.) peak is mainly caused by backgrounds while the multiple p.e. peak is from scintillation photons.

Fig. 6.24 shows the result of one-minute measurement for the LAB-PPO sample. The data points in the 2D plot represent the triggered event fall in certain ADC channel numbers in each channel. A 10 ns coincidence window cut was applied to cut down noise, single p.e. and background events. The events in the 0 ADC channel, which represent noises, were totally cut off after applying the coincidence. Fig. 18 shows the results of the TeSOP and

TeDDA samples. Compared to the LAB-PPO sample, a shift of the multiple p.e. peak due to the different light yields between the samples can be observed clearly.

In Fig. 18, the 2D plots in Fig. 6.24 are projected onto a single channel. We used an empty vial and let  $\gamma$ -rays from  $^{137}\text{Cs}$  source pass through it for a background run (without the coincidence cut). This is to verify the single p.e. peak and noise region, shown as the black background spectrum.

From this plot, the single p.e. peaks for all the samples as well as the background match together. The multiple p.e. peaks indicate the different light yields of the scintillator samples. Here we can clearly see the multiple p.e. peak of the LAB-PPO occupies the largest ADC channel number, while the channels of TeSOP is slightly larger than the TeDDA.

To quantify the light yield differences between different samples, an analysis method of charge weighted photon number has been applied as the following:

First, from the spectrum, fit the single p.e. peak with an asymmetric Gaussian function, as shown in Fig. 19. The mean value of the asymmetric Gaussian represents the ADC channel number corresponding to the single p.e. peak.

$$\xi = -\frac{\alpha(x-\mu)}{\sqrt{2}\sigma}, f_{asym} = c \cdot e^{-\frac{1}{2}(\frac{x-\mu}{\sigma})^2} \cdot \text{Erfc}(\xi)$$

$$p_0 = \mu, p_1 = \sigma, p_2 = \alpha, p_3 = c$$

Then for the multiple p.e. region, weighting (dividing) the counts of the event in each channel with the single p.e. ADC channel number to calculate the total number of the photons.

Fig. 19. Fit the single p.e. peak with an asymmetric Gaussian function (fasym) to obtain the adc channel for weighting. The mean value of  $p_0$  is used as the adc channel relative to a single p.e. peak.

To define the multiple p.e. region for the counting, the spectrum projected on each channel with and without coincidence cut are compared to define a threshold of the ADC channel for counting. By integrating from this threshold, the total numbers of events between two spectrum are close to each other. From two channels, we get two thresholds and then define a box cut in the 2D coincidence plot. We weights the events in the box to

obtain the total number of photons. Fig. 16 and Fig. 19 show the case of the LAB-PPO sample.

Fig. ?? 2D LABPPO spectrum with coincidence cut. A box cut is defined for multiple PE counting.

Once the total number of the photons for a certain sample is counted, we can calculate its ratio to the LAB-PPO sample to obtain the relative light yield.

## Results

Table 6.11: Number of photons calculated by Charge weighted photon number method.

Sample	Number of photons ( $\times 10^6$ )	RLY
LAB-PPO	2.0811	1
TeDDA	1.2652	0.61
TeSOP	1.3976	0.67

Table. 6.11 shows the number of photons calculated by Charge weighted photon number method.

Here we quantify the relative light yields of our samples. The light yield of the 0.5% Te by SOP synthesis procedure (TeSOP) is 0.61 and the one of the 0.5% Te by DDA procedure is 0.67. The light yield of TeSOP is slightly larger than the TeDDA. In [cite billerTe], a relative light yield of 0.65 was reported.

# **Chapter 7**

## **Conclusions**

In this thesis, a vertex/direction reconstruction algorithm framework is developed for multiple SNO+ physics phases.

## Appendix A

# Details for the MultiPath Fitter

### A.1 Create a Random Vertex

Four random seeds are generated from the uniform distribution function: *RandFlat* in Class Library for High Energy Physics (CLHEP) library.

One random seed is used for generating the time of the vertex:  $t$  is a random variable following a uniform distribution in a range of [100, 300] ns, say,  $t \sim U(100, 300)$ .

Three random seeds are used for generating the position of the trial vertex:  $ran0 \sim U(0, 1)$ ,  $ran1 \sim U(-1, 1)$  and  $ran2Pi \sim U(0, 2\pi)$ .

Let  $r = \sqrt[3]{ran0} * 10000$  mm,  $\phi = ran2Pi$ ,  $\cos \theta = ran1$  and  $\sin \theta = \sqrt{1 - \cos^2 \theta}$ , then the trial position can be built in Cartesian coordinate system:  $\vec{x}_{trial} = (r \sin \theta \cos \phi, r \sin \theta \sin \phi, r \cos \theta)$ . This procedure ensures that a proper random position is generated inside a sphere with a radius of 10 m.

### A.2 Levenberg-Marquardt (MRQ) Method for Minimization[1]

Levenberg-Marquardt method is a common routine for non-linear fitting. Let  $\mathbf{a} = [a_0, a_1, \dots, a_{M-1}]^T$  be an  $M$ -dimensional vector with  $M$  unknown parameters to be fit, for example,  $\mathbf{a}$  is an event vertex with 4 parameters:  $\mathbf{a} = [x, y, z, t]^T$ .

A  $\chi^2$  merit function with the unknown parameter vector  $\mathbf{a}$  can be built and by mini-

mizing the function, the best-fit  $\mathbf{a}$  can be found.

The  $\chi^2(\mathbf{a})$  can be approximately expanded into a quadratic form of Taylor-series:

$$\chi^2(\mathbf{a}) \simeq \gamma - \mathbf{d} \cdot \mathbf{a} + \frac{1}{2} \mathbf{a} \cdot \mathbf{D} \cdot \mathbf{a}, \quad (\text{A.1})$$

where  $\gamma$  is a  $M$ -dimension constant vector around  $\mathbf{a}$ ,  $\mathbf{d}$  is a  $M$ -dimension vector and  $\mathbf{D}$  is a  $M \times M$  Hessian matrix.

To find a  $\mathbf{a}_{min}$  so that a  $\min \chi^2(\mathbf{a}_{min})$  is reached, in computing science we usually use iteration steps:

$$\mathbf{a}_{min} = \mathbf{a}_{cur} + D^{-1}[-\nabla \chi^2(\mathbf{a}_{cur})], \quad (\text{A.2})$$

where  $\mathbf{a}_{cur}$  is the current trial value of  $\mathbf{a}$  and we assume matrix  $\mathbf{D}$  is invertible. The  $\mathbf{a}_{cur}$  thus jumps onto  $\mathbf{a}_{min}$ .

According to the definition of a  $\chi^2$  merit function, it can be written out explicitly as:  $\chi^2(\mathbf{a}) = \sum_{i=0}^{N-1} [\frac{y_i - y(x_i|\mathbf{a})}{\sigma_i}]^2$ , with the same Taylor expansion, the quadratic form is written as:

$$\chi^2(\mathbf{a}) \approx \chi^2(\mathbf{a}_{cur}) + \sum_k \frac{\partial \chi^2(\mathbf{a}_{cur})}{\partial a_k} \delta a_k + \frac{1}{2} \sum_{kl} \frac{\partial^2 \chi^2(\mathbf{a}_{cur})}{\partial a_k \partial a_l} \delta a_k \delta a_l, \quad (\text{A.3})$$

where the first derivatives are:

$$\frac{\partial \chi^2}{\partial a_k} = -2 \sum_{i=0}^{N-1} [\frac{y_i - y(x_i|\mathbf{a})}{\sigma_i}] \frac{\partial y(x_i|\mathbf{a})}{\partial a_k}, k = 0, 1, \dots, M-1, \quad (\text{A.4})$$

and the second derivatives are:

$$\frac{\partial^2 \chi^2}{\partial a_k \partial a_l} = 2 \sum_{i=0}^{N-1} \left\{ \frac{\partial y(x_i|\mathbf{a})}{\partial a_k} \frac{\partial y(x_i|\mathbf{a})}{\partial a_l} - [y_i - y(x_i|\mathbf{a})] \frac{\partial^2 y(x_i|\mathbf{a})}{\partial a_k \partial a_l} \right\}, k = 0, 1, \dots, M-1. \quad (\text{A.5})$$

Let  $\beta_k \equiv -\frac{1}{2} \frac{\partial \chi^2}{\partial a_k}$ ,  $\alpha_{kl} \equiv \frac{1}{2} \frac{\partial^2 \chi^2}{\partial a_k \partial a_l}$ , then the factor of 2 is removed. The  $\alpha_{kl}$  is defined as the curvature matrix and  $\alpha = \frac{1}{2} \mathbf{D}$ , which implies that it is the half of the Hessian matrix.

From A.2, we have:  $D(\mathbf{a}_{min} - \mathbf{a}_{cur}) = [-\nabla \chi^2(\mathbf{a}_{cur})] \implies 2\alpha \delta \mathbf{a} = 2\beta$ . The A.2 is now transformed into a systems of linear equations:

$$\sum_{l=0}^{M-1} \alpha_{kl} \delta a_l = \beta_k, \quad (\text{A.6})$$

where  $\delta a_l$  is a varying amount added to the current value of parameter for the next iteration.

The main task now is to calculate  $\alpha_{kl}$  and  $\beta_k$  and then solve for  $\delta a_l$  in A.6. Once  $\delta a_l$  is solved, we can vary the current trial or approximate values of  $\mathbf{a}_{cur}$  and let it go close to or reach the  $\mathbf{a}_{min}$ .

If we consider the method of steepest descent:  $\mathbf{a}_{next} = \mathbf{a}_{cur} - \text{const} \cdot \nabla \chi^2(\mathbf{a}_{cur})$ , where const is a constant, then the  $\delta a_l$  is solved by

$$\delta a_l = \text{const} \cdot \beta_l, \quad (\text{A.7})$$

where no Hessian matrix is needed.

In the Levenberg-Marquardt method, in order to solve for  $\delta a_l$ , the detailed calculation of  $\mathbf{D}^{-1}$  in A.2 and the simplified calculation of steepest descent in A.7 are combined and a smooth transition between A.2 and A.7 is considered.

In A.7, the const describes the distance or magnitude of how far the parameter should go along the gradient  $\beta_l$ . From dimensional analysis, since  $\beta_k \equiv -\frac{1}{2} \frac{\partial \chi^2}{\partial a_k}$  and  $\chi^2$  is a non-dimensional number,  $[\beta_l] = [1/a_l]$ . Then from A.7,  $[\text{const}] = [a_l^2]$ . The const has the same dimension to the term  $1/\alpha_{ll} = 1/(\frac{1}{2} \frac{\partial^2 \chi^2}{\partial a_l \partial a_l})$ , i.e., the diagonal elements in the curvature matrix. A bridge between A.2 and A.7 is thus built. The diagonal elements in the curvature matrix can control the magnitude of the const, tells how far the parameter should go along the gradient.

Then A.7 can be written as:

$$\delta a_l = \frac{1}{\lambda \alpha_{ll}} \beta_l \text{ or } \lambda \alpha_{ll} \delta a_l = \beta_l, \quad (\text{A.8})$$

where  $\alpha_{ll}$  is written in a form of  $\alpha_{ll} = \sum_{i=0}^{N-1} \frac{1}{\sigma_i^2} \left[ \frac{\partial y(x_i | \mathbf{a})}{\partial a_l} \frac{\partial y(x_i | \mathbf{a})}{\partial a_l} \right]$  to ensure that  $\alpha_{ll}$  is always positive; a fudge factor  $\lambda$  can be set to  $\lambda \gg 1$  to avoid the case when the value of const is taken too large.

Compare A.6 and A.8, if define a new curvature matrix  $\alpha'$  as  $\alpha'_{jj} \equiv (1 + \lambda) \alpha_{jj}$  (for diagonal elements) and  $\alpha'_{jk} \equiv \alpha_{jk}$  ( $j \neq k$ ) (for non-diagonal elements), these two equations can be combined into one:

$$\sum_{l=0}^{M-1} \alpha'_{kl} \delta a_l = \beta_k \quad (\text{A.9})$$

From the definition of  $\alpha'$ , if  $\lambda$  takes a large value,  $\alpha'$  is dominated by diagonal elements, then A.9 is close to A.8; while if  $\lambda \rightarrow 0$ , A.9 is close to A.6.

The algorithm of Levenberg-Marquardt method requires a reasonable start value (first guess) of the fitting parameter  $\mathbf{a}$  and a reasonable preset value of  $\lambda$  (usually take  $\lambda = 0.001$ ). The iteration loop of the algorithm is: calculate the value of  $\chi^2(\mathbf{a})$ , solve for  $\delta\mathbf{a}$  from A.9 and then calculate  $\chi^2(\mathbf{a} + \delta\mathbf{a})$ . During this loop, the algorithm checks whether  $\chi^2(\mathbf{a} + \delta\mathbf{a}) \geq \chi^2(\mathbf{a})$ , if it is,  $\lambda$  is increased by  $\lambda = 10 \cdot \lambda$ ; if not,  $\lambda$  is decreased by  $\lambda = 0.1 \cdot \lambda$ .

The iteration loop is terminated when the change amount of the  $\chi^2$  is negligible: if the loop calculates several  $\chi^2$  values which are close to each other (for example,  $|\chi^2_{current} - \chi^2_{previous}| < 0.001$ ), the algorithm will consider the  $\chi^2$  is minimized with a set of best-fit parameters. Here the termination condition of iterating the  $\chi^2$  value to convergence to machine accuracy or to the roundoff limit is not used, since  $\chi^2$  is a statistical quantity rather than a solution of an equation. It is not statistical meaningful to vary the value of  $\mathbf{a}$  to vary  $\chi^2$  by a small amount  $\ll 1$ .

Once the minimum is reached, set  $\lambda = 0$  and then the estimated covariance matrix of the standard errors in the fitted  $\mathbf{a}$  can be calculated as:  $C \equiv \alpha^{-1}$ .

### A.3 Detailed Light Path Calculations in the MultiPath Scintwater Fitter

The following algorithm shows the detailed calculations for evaluating the light path in the scintillator regions. Each check steps are marked by number and if-conditions are marked by latin letters (a, b or c).

First check the ray-sphere intersection (equation. 4.4):

If  $\Delta > 0$ ,

(step. 1a) if  $|\vec{x}_0| < r_{AV}$  (and  $a_+ > 0 > a_-$ ), check the ray-plane intersection:

(2a-a) if  $a_3 > 0$ , the ray-vector hits the interface plane:

(3a-a-a) if  $z_0 < Z_{split}$  and  $a_3 < a_+$ :  $d_{sp,AV} = a_+ - a_3$ , see Fig. A.1 (a).

(3a-a-b) if  $z_0 \geq Z_{split}$ :

(4a-a-b-a) if  $a_3 < a_+$ :  $d_{sp,AV} = a_3$ , see Fig. A.1 (b).

(4a-a-b-b) if  $a_3 \geq a_+$ :  $d_{sp,AV} = a_+$ , see Fig. A.1 (c).

(2a-b) if  $a_3 \leq 0$ :

(3a-b) if  $z_0 > Z_{split}$ :  $d_{sp,AV} = a_+$ , see Fig. A.1 (d).

(step. 1b) if  $|\vec{x}_0| \geq r_{AV}$  (and  $a_+ > a_- > 0$ ), calculate the z position of the intersection point:  $z_{\pm} = z_0 + a_{\pm} \cdot (z_{PMT} - z_0) / |\vec{X}_{PMT} - \vec{X}_0|$ :

(1-b-a) if  $z_- \geq Z_{split}$  and  $z_+ \geq Z_{split}$ :  $d_{sp,AV} = a_+ - a_-$ , see Fig. A.1 (e).

(1-b-b) if  $z_- < Z_{split}$  and  $z_+ > Z_{split}$  and  $a_3 > 0$ :  $d_{sp,AV} = a_+ - a_3$ , see Fig. A.1 (f).

(1-b-c) if  $z_- > Z_{split}$  and  $z_+ < Z_{split}$  and  $a_3 > 0$ :  $d_{sp,AV} = a_3 - a_-$ , see Fig. A.1 (g).

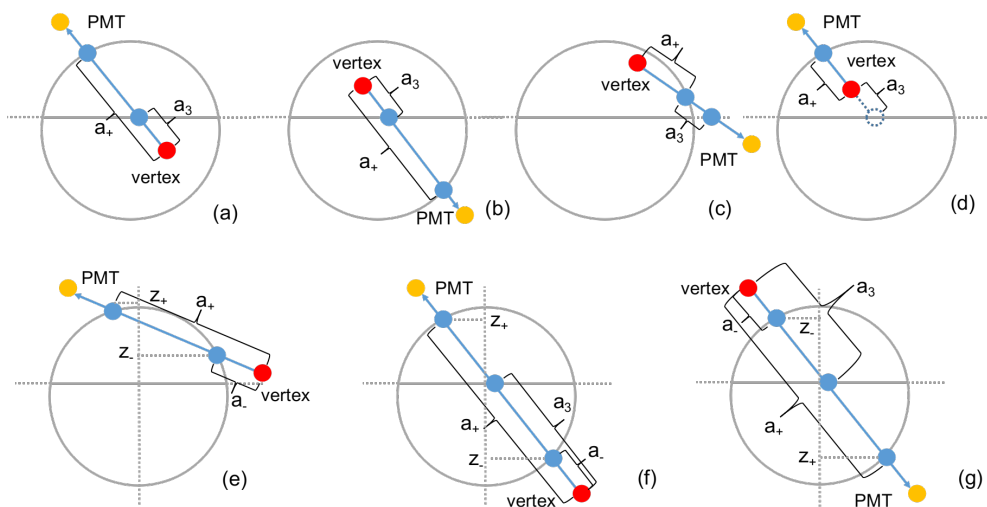


Figure A.1: Layouts for the scintillator light paths inside the AV sphere.

First check the ray-cylinder intersection (equation. 4.4):

If  $\Delta_{neck} > 0$ ,

(step. 1a) if  $a'_+ a'_- < 0$  (event position is inside the cylinder), check the z position of the intersection point on neck,  $z_+ = z_0 + a'_+ u_z$ :

(2a-a) if  $6108 < z_+ < 8390 \text{ mm}$  (in the valid neck region), then check the AV sphere:

(3a-a-a) if  $|\vec{X}_0| \geq r_{AV}$ :  $d_{sp,neck} = a'_+$ , see Fig. A.2 (a).

(3a-a-b) if  $|\vec{X}_0| < r_{AV}$  and  $a_+ a_- < 0$ :  $d_{sp,neck} = a'_+ - a_+$ , the light ray first hits the sphere inside the cylinder and then hits the cylinder, see Fig. A.2 (b).

(2a-b) if  $z_+ < 6108 \text{ mm}$ :

(3a-b) if  $|\vec{X}_0| \geq r_{AV}$  and  $6108 < z_0 < 8390 \text{ mm}$ :

(4a-b) if  $a_+ > a_- > 0$ :  $d_{sp,neck} = a_-$ , see Fig. A.2 (c).

(step. 1b) if  $a'_+ > a'_- > 0$  (event position is outside the cylinder), check the z position of the intersection point on neck,  $z'_\pm = z_0 + a'_\pm \cdot u_z$ :

(2b-a) if  $6108 < z'_\pm < 8390 \text{ mm}$ , check the AV intersection:

(3b-a-a) if  $a_\pm$  do not exit (never passes through AV),  $d_{sp,neck} = a'_+ - a'_-$ , see Fig. A.2 (d).

(3b-a-b) if  $a_+ > a_- > 0$ , evaluate the z positions of the ray-sphere intersection points  $z_\pm = z_0 + a_\pm \cdot u_z$ :

(4b-a-a) if  $z_\pm \geq 6108 \text{ mm}$ :  $d_{sp,neck} = a'_+ - a'_- - (a_+ - a_-)$ , see Fig. A.2 (e). The path inside the sphere is subtracted to avoid duplicated calculation.

(4b-a-b) if  $z_+ < 6108$  and  $6108 < z_- < 8390 \text{ mm}$ :

(5b-a-b-a) if  $a_+ > a_- > 0$ :  $d_{sp,neck} = a_- - a'_-$ , see Fig. A.2 (f).

(5b-a-b-b) if  $z_- < 6108$  and  $6108 < z_+ < 8390 \text{ mm}$ :

in this case, either the event position is inside the sphere ( $a_+ a_- < 0$ ), shown in Fig. A.2 (g), or outside the sphere ( $a_+ a_- < 0$ ), shown in Fig. A.2 (h)), the path in neck is same:  $d_{sp,neck} = a'_+ - a_+$ .

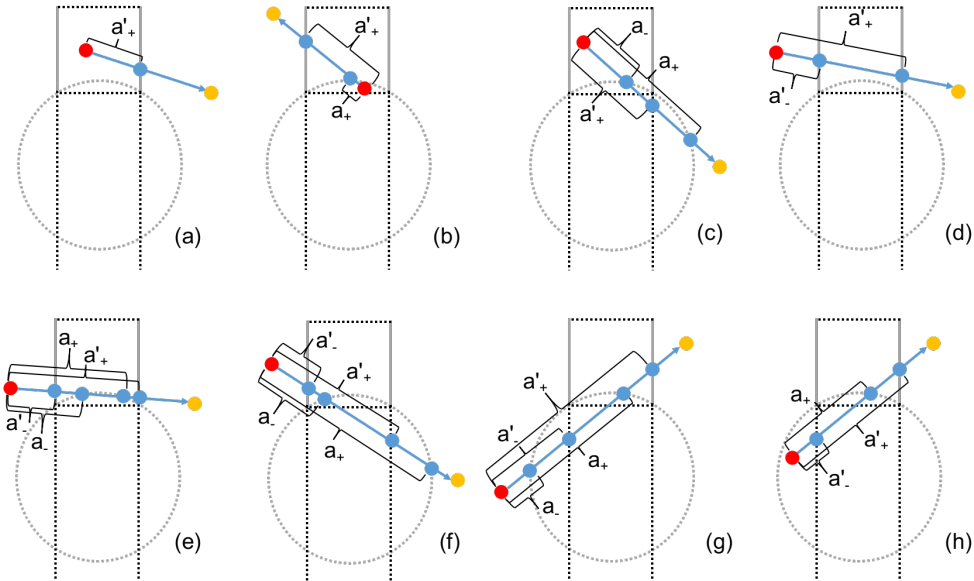


Figure A.2: Layouts of the scintillator light paths inside the neck cylinder.

## **Appendix B**

# **Information for $^{16}\text{N}$ Scan Runs**

### **B.1 Information for $^{16}\text{N}$ Scan Runs**

The tables below show the  $^{16}\text{N}$  runs used in this thesis. Table. B.1, Table. B.1 and Table. B.1 are the internal scans inside the AV along the detector z-axis, y-axis and x-axis respectively. Table. B.1 show the external scans.

Table B.1:  $^{16}\text{N}$  internal z-axis scan runs.

run number	nominal source position [mm]		
	x	y	z
100934	-186.0	256.0	1.0
106925	-186.0	254.0	-4999.899
106930	-186.0	254.0	-4500.2
106942	-186.0	254.0	-4001.0
106944	-186.0	254.0	-3501.399
106946	-186.0	254.0	-2999.7
106948	-186.0	254.0	-2500.399
106950	-186.0	254.0	-1998.499
106954	-186.0	254.0	-1000.099
106956	-186.0	254.0	-499.6
106960	-186.0	254.0	500.8
106962	-186.0	254.0	1000.3
106964	-186.0	254.0	1500.9
106967	-186.0	254.0	2000.001
106969	-186.0	254.0	2500.3
106971	-186.0	254.0	3000.3
106973	-186.0	254.0	3500.9
106975	-186.0	254.0	4000.5
106977	-186.0	254.0	4500.4
106979	-185.037	247.24	4973.567

Table B.2:  $^{16}\text{N}$  internal y-axis scan runs.

run number	nominal source position [mm]		
	x	y	z
106992	-5.995	-0.201	-1.107
106994	-7.761	-998.068	0.159
106996	-7.084	-2000.578	-0.716
106998	-5.491	-2998.017	-4.196
107000	-3.774	-3992.167	-7.374
107002	-1.624	-4999.882	-12.012
107004	-1.745	5002.057	-9.897
107006	-3.967	3973.021	-7.359
107008	-5.984	2980.035	-3.441
107010	-7.952	1986.669	-1.714
107012	-9.242	994.183	0.553
107014	-9.867	496.858	0.269
107016	-8.414	1494.71	0.634
107018	-6.835	2487.539	-1.126
107026	-4.949	3496.338	-5.971
107028	-2.539	4505.371	-7.453
107030	-7.711	-501.268	0.126
107033	-7.534	-1494.927	-0.096
107035	-6.349	-2487.912	-1.434
107043	-4.366	-3475.769	-6.019
107045	-2.799	-4498.62	-10.213

Table B.3:  $^{16}\text{N}$  internal x-axis scan runs.

run number	nominal source position [mm]		
	x	y	z
107055	-5.283	-0.209	-1.057
107075	-4999.043	2.46	-9.899
107077	-4002.525	5.269	-7.364
107079	-3004.229	8.101	-2.54
107081	-2000.155	10.637	-0.361
107083	-992.994	11.641	0.024
107085	998.133	10.897	-0.044
107087	2011.103	9.874	0.057
107091	4003.323	4.378	-5.974
107093	5004.868	2.262	-7.547
107095	4503.445	3.278	-7.0
107110	-4489.301	3.918	-10.545
107116	3511.147	5.742	-2.578
107118	2502.805	8.681	-2.803
107120	-3476.709	6.643	-4.886

Table B.4:  $^{16}\text{N}$  external scan runs.

run number	nominal source position [mm]		
	x	y	z
111211	-5861.0	-2524.0	-1.62
111213	-5861.0	-2524.0	-5000.525
111215	-5861.0	-2524.0	-4000.021
111217	-5861.0	-2524.0	-3000.151
111219	-5861.0	-2524.0	-1999.248
111221	-5861.0	-2524.0	-998.923
111223	-5861.0	-2524.0	1000.798
111225	-5861.0	-2524.0	2000.597
111228	-5861.0	-2524.0	3000.734
111230	-5861.0	-2524.0	4000.977
111232	-5861.0	-2524.0	5000.86
111234	-5861.0	-2524.0	4498.167
111236	-5861.0	-2524.0	3498.838
111238	-5861.0	-2524.0	2498.641
111240	-5861.0	-2524.0	1498.713
111242	-5861.0	-2524.0	-1501.717
111244	-5861.0	-2524.0	-2500.89
111246	-5861.0	-2524.0	-3500.764
111248	-5861.0	-2524.0	-4500.812

# References

- [1] W. H. Press, S. A. Teukolsky, W. T. Vetterling, and B. P. Flannery, *Numerical recipes 3rd edition: The art of scientific computing*. Cambridge university press, 2007.
- [2] L. Oberauer, A. Ianni, and A. Serenelli, *Solar Neutrino Physics: The Interplay Between Particle Physics and Astronomy*. John Wiley & Sons, 2020.
- [3] J. N. Bahcall, A. M. Serenelli, and S. Basu, “New solar opacities, abundances, helioseismology, and neutrino fluxes,” *The Astrophysical Journal Letters*, vol. 621, no. 1, p. L85, 2005.
- [4] J. W. F. Valle and J. Romao, *Neutrinos in high energy and astroparticle physics*. John Wiley & Sons, 2015.
- [5] the SNO+ collaboration, “The SNO+ experiment,” *To be published*.
- [6] P. G. Jones, *Background rejection for the neutrinoless double beta decay experiment SNO+*. PhD thesis, University of Oxford, 2011.
- [7] J. Birks and F. Firk, “The theory and practice of scintillation counting,” *Physics Today*, vol. 18, p. 60, 1965.
- [8] G. F. Knoll, *Radiation Detection and Measurement*. John Wiley & Sons, 2010.
- [9] M. Dragowsky, A. Hamer, Y. Chan, R. Deal, E. Earle, W. Frati, E. Gaudette, A. Hallin, C. Hearns, J. Hewett, *et al.*, “The  $^{16}\text{N}$  calibration source for the sudbury neutrino observatory,” *Nuclear Instruments and Methods in Physics Research Section*

- A: Accelerators, Spectrometers, Detectors and Associated Equipment*, vol. 481, no. 1-3, pp. 284–296, 2002.
- [10] R. F. MacLellan, *The energy calibration for the solar neutrino analysis of all three phases of the Sudbury Neutrino Observatory*. PhD thesis, Queen's University, 2009.
  - [11] M. Mottram, “N16 source update,” *SNO+ Internal Document, docDB-1769-v1*.
  - [12] Z. Barnard, “Update to N16 geometry,” *SNO+ Internal Document, docDB-4414-v1*.
  - [13] R. Bayes, “Analysis of N16 scan,” *SNO+ Internal Document, docDB-4482-v2*.
  - [14] E. Turner, “A water scattering scaling factor for rat,” *SNO+ Internal Document, docDB-5864-v2*.
  - [15] S. J. Brice, *Monte Carlo and Analysis Techniques for the Sudbury Neutrino Observatory*. PhD thesis, University of Oxford, 1996.
  - [16] P. Skensved and B. Robertson, “Miscellaneous effects,” *SNO Technical Report, SNO-STR-90-28*.
  - [17] J. Tseng, “Skyshine classifier,” *SNO+ Internal Document, docDB-5341-v1*.
  - [18] E. Leming, “Oxford LAB + PPO timing and light yield measurements,” *SNO+ Internal Document, docDB-6179-v1*.
  - [19] A. Hallin, “Fitting partial fill data from december 2014,” *SNO+ Internal Document, docDB-2888-v3*.
  - [20] D. Auty and A. Hallin, “Partial water fitter,” *SNO+ Internal Document, docDB-2965-v2*.
  - [21] K. Singh, “Wavelength shifter: Carbostyryl 124,” *SNO+ Internal Document, docDB-3351-v2*.
  - [22] K. Singh, “Wavelength shifter in water phase of sno+,” *SNO+ Internal Document, docDB-3869-v2*.

- [23] K. Singh, “Multipath fitter processor,” *SNO+ Internal Document, docDB-3849-v1*.
- [24] J. Hu and J. Tseng, “Updates on the multipath water fitter 2018,” *SNO+ Internal Document, docDB-4936-v2*.
- [25] J. Leite-Lopes, “Weak interaction physics: from its origin to the electroweak model,” tech. rep., SCAN-9607019, 1996.
- [26] H. Bethe and R. Peierls, “The “neutrino”,” *Nature*, vol. 133, no. 3362, pp. 532–532, 1934.
- [27] F. Reines, C. Cowan Jr, F. Harrison, A. McGuire, and H. Kruse, “Detection of the free antineutrino,” *Physical Review*, vol. 117, no. 1, p. 159, 1960.
- [28] M. Goldhaber, L. Grodzins, and A. Sunyar, “Helicity of neutrinos,” *Physical Review*, vol. 109, no. 3, p. 1015, 1958.
- [29] E. Akhmedov, “Quantum mechanics aspects and subtleties of neutrino oscillations,” *arXiv preprint arXiv:1901.05232*, 2019.
- [30] Y. Fukuda, T. Hayakawa, E. Ichihara, K. Inoue, K. Ishihara, H. Ishino, Y. Itow, T. Kajita, J. Kameda, S. Kasuga, *et al.*, “Evidence for oscillation of atmospheric neutrinos,” *Physical Review Letters*, vol. 81, no. 8, p. 1562, 1998.
- [31] M. Tanabashi, K. Hagiwara, K. Hikasa, K. Nakamura, Y. Sumino, F. Takahashi, J. Tanaka, K. Agashe, G. Aielli, C. Amsler, *et al.*, “Review of particle physics,” *Physical Review D*, vol. 98, no. 3, p. 030001, 2018.
- [32] Wikipedia, *CP violation*, 2020 (accessed Mar 15, 2020). <https://en.wikipedia.org/wiki/CPViolation>.
- [33] I. J. Aitchison and A. J. Hey, *Gauge theories in particle physics: A practical introduction, Volume 2: Non-Abelian Gauge theories: QCD and the electroweak theory*, vol. 2. CRC Press, 2012.

- [34] S. Abe, T. Ebihara, S. Enomoto, K. Furuno, Y. Gando, K. Ichimura, H. Ikeda, K. Inoue, Y. Kibe, Y. Kishimoto, *et al.*, “Precision measurement of neutrino oscillation parameters with kamland,” *Physical Review Letters*, vol. 100, no. 22, p. 221803, 2008.
- [35] K. Abe, C. Bronner, Y. Haga, Y. Hayato, M. Ikeda, K. Iyogi, J. Kameda, Y. Kato, Y. Kishimoto, L. Marti, *et al.*, “Atmospheric neutrino oscillation analysis with external constraints in super-kamiokande i-iv,” *Physical Review D*, vol. 97, no. 7, p. 072001, 2018.
- [36] F. P. An, A. Balantekin, H. Band, M. Bishai, S. Blyth, D. Cao, G. Cao, J. Cao, W. Cen, Y. Chan, *et al.*, “Measurement of electron antineutrino oscillation based on 1230 days of operation of the daya bay experiment,” *Physical Review D*, vol. 95, no. 7, p. 072006, 2017.
- [37] X. Qian and J.-C. Peng, “Physics with reactor neutrinos,” *Reports on Progress in Physics*, vol. 82, no. 3, p. 036201, 2019.
- [38] E. Antonio, *State Of The Art Of Neutrino Physics, The: A Tutorial For Graduate Students And Young Researchers*, vol. 28. World Scientific, 2018.
- [39] Z. Xing and S. Zhou, *Neutrinos in particle physics, astronomy and cosmology*. Springer Science & Business Media, 2011.
- [40] K. Abe, J. Amey, C. Andreopoulos, M. Antonova, S. Aoki, A. Ariga, Y. Ashida, S. Ban, M. Barbi, G. Barker, *et al.*, “Measurement of neutrino and antineutrino oscillations by the t2k experiment including a new additional sample of  $\nu_e$  interactions at the far detector,” *Physical Review D*, vol. 96, no. 9, p. 092006, 2017.
- [41] K. Abe, R. Akutsu, A. Ali, C. Alt, C. Andreopoulos, L. Anthony, M. Antonova, S. Aoki, A. Ariga, Y. Asada, *et al.*, “Constraint on the matter-antimatter symmetry-violating phase in neutrinooscillations,” *arXiv preprint arXiv:1910.03887*, 2019.
- [42] A. Y. Smirnov, “Solar neutrinos: Oscillations or no-oscillations?,” *arXiv preprint arXiv:1609.02386*, 2016.

- [43] A. Y. Smirnov, “The msw effect and matter effects in neutrino oscillations,” *Physica Scripta*, vol. 2005, no. T121, p. 57, 2005.
- [44] M. Fukugita and T. Yanagida, *Physics of Neutrinos: and Application to Astrophysics*. Springer Science & Business Media, 2013.
- [45] K. Kimura, A. Takamura, and H. Yokomakura, “Exact formula of probability and cp violation for neutrino oscillations in matter,” *Physics Letters B*, vol. 537, no. 1-2, pp. 86–94, 2002.
- [46] J. N. Bahcall, “Solar neutrinos. i. theoretical,” *Physical Review Letters*, vol. 12, no. 11, p. 300, 1964.
- [47] R. Davis Jr, “Solar neutrinos. ii. experimental,” *Physical Review Letters*, vol. 12, no. 11, p. 303, 1964.
- [48] R. Becker-Szendy, C. Bratton, D. Casper, S. Dye, W. Gajewski, M. Goldhaber, T. Haines, P. Halverson, D. Kielczewska, W. Kropp, *et al.*, “Electron-and muon-neutrino content of the atmospheric flux,” *Physical Review D*, vol. 46, no. 9, p. 3720, 1992.
- [49] W. Allison, G. Alner, D. Ayres, W. Barrett, C. Bode, P. Border, C. Brooks, J. Cobb, D. Cockerill, R. Cotton, *et al.*, “Measurement of the atmospheric neutrino flavour composition in soudan 2,” *Physics Letters B*, vol. 391, no. 3-4, pp. 491–500, 1997.
- [50] T. Kajita, “Atmospheric neutrinos,” *Advances in High Energy Physics*, vol. 2012, 2012.
- [51] A. Giaz, “Status and perspectives of the JUNO experiment,” *arXiv preprint arXiv:1804.03575*, 2018.
- [52] H. A. Bethe, “Energy production in stars,” *Physical Review*, vol. 55, no. 5, p. 434, 1939.

- [53] F. Suekane, *Neutrino oscillations: a practical guide to basics and applications*, vol. 898. Springer, 2015.
- [54] W. C. Haxton, R. Hamish Robertson, and A. M. Serenelli, “Solar neutrinos: status and prospects,” *Annual Review of Astronomy and Astrophysics*, vol. 51, pp. 21–61, 2013.
- [55] E. Ahmedov, “Majorana neutrinos and other majorana particles: Theory and experiment,” *arXiv preprint arXiv:1412.3320*, 2014.
- [56] A. Zee, *Quantum field theory in a nutshell, 2nd edn.*, vol. 7. Princeton university press, 2011.
- [57] E. Majorana and L. Maiani, *A symmetric theory of electrons and positrons*. Springer, 2006.
- [58] C.-S. Wu, E. Ambler, R. Hayward, D. Hopps, and R. P. Hudson, “Experimental test of parity conservation in beta decay,” *Physical review*, vol. 105, no. 4, p. 1413, 1957.
- [59] W. Greiner and B. Müller, *Theoretical Physics Text and Exercise Books: Volume 5: Gauge Theory of Weak Interactions*. Springer Science & Business Media, 2012.
- [60] R. Z. Funchal, B. Schmauch, and G. Giesen, “The physics of neutrinos,” *arXiv preprint arXiv:1308.1029*, 2013.
- [61] C. Giunti and C. W. Kim, *Fundamentals of neutrino physics and astrophysics*. Oxford university press, 2007.
- [62] J. Lesgourgues, G. Mangano, G. Miele, and S. Pastor, *Neutrino cosmology*. Cambridge University Press, 2013.
- [63] K. Zuber, “On the physics of massive neutrinos,” *Physics Reports*, vol. 305, no. 6, pp. 295–364, 1998.
- [64] V. Barger, D. Marfatia, and K. Whisnant, *The physics of neutrinos*. Princeton University Press, 2012.

- [65] C. Dvorkin, M. Gerbino, D. Alonso, N. Battaglia, S. Bird, A. D. Rivero, A. Font-Ribera, G. Fuller, M. Lattanzi, M. Loverde, *et al.*, “Neutrino mass from cosmology: Probing physics beyond the standard model,” *arXiv preprint arXiv:1903.03689*, 2019.
- [66] M. Gerbino and M. Lattanzi, “Status of neutrino properties and future prospectscosmological and astrophysical constraints,” *Frontiers in Physics*, vol. 5, p. 70, 2018.
- [67] N. Aghanim, Y. Akrami, M. Ashdown, J. Aumont, C. Baccigalupi, M. Ballardini, A. Banday, R. Barreiro, N. Bartolo, S. Basak, *et al.*, “Planck 2018 results-vi. cosmological parameters,” *Astronomy & Astrophysics*, vol. 641, p. A6, 2020.
- [68] C. Rötteler, “Tritium suppression factor of the katrin transport section,” 2019.
- [69] M. Aker, K. Altenmüller, M. Arenz, M. Babutzka, J. Barrett, S. Bauer, M. Beck, A. Beglarian, J. Behrens, T. Bergmann, *et al.*, “Improved upper limit on the neutrino mass from a direct kinematic method by katrin,” *Physical review letters*, vol. 123, no. 22, p. 221802, 2019.
- [70] B. Povh, K. Rith, and F. Zetsche, *Particles and nuclei*, vol. 1. Springer, 2008.
- [71] B. R. Martin and G. Shaw, *Nuclear and particle physics: an introduction*. John Wiley & Sons, 2019.
- [72] S. Bilenky, *Introduction to the physics of massive and mixed neutrinos*, vol. 947. Springer, 2018.
- [73] M. J. Dolinski, A. W. Poon, and W. Rodejohann, “Neutrinoless double-beta decay: status and prospects,” *Annual Review of Nuclear and Particle Science*, vol. 69, pp. 219–251, 2019.
- [74] K. Zuber, *Neutrino physics*. CRC press, 2020.
- [75] O. Cremonesi and M. Pavan, “Challenges in double beta decay,” *Advances in High Energy Physics*, vol. 2014, 2014.

- [76] I. Shimizu and M. Chen, “Double beta decay experiments with loaded liquid scintillator,” *Frontiers in Physics*, vol. 7, p. 33, 2019.
- [77] M. Agostini, M. Allardt, A. Bakalyarov, M. Balata, I. Barabanov, L. Baudis, C. Bauer, N. Becerici-Schmidt, E. Bellotti, S. Belogurov, *et al.*, “Search of neutrinoless double beta decay with the gerda experiment,” *Nuclear and particle physics proceedings*, vol. 273, pp. 1876–1882, 2016.
- [78] M. Agostini, A. Bakalyarov, M. Balata, I. Barabanov, L. Baudis, C. Bauer, E. Bellotti, S. Belogurov, A. Bettini, L. Bezrukov, *et al.*, “Probing majorana neutrinos with double- $\beta$  decay,” *Science*, vol. 365, no. 6460, pp. 1445–1448, 2019.
- [79] J. Albert, D. Auty, P. Barbeau, E. Beauchamp, D. Beck, V. Belov, C. Benitez-Medina, J. Bonatt, M. Breidenbach, T. Brunner, *et al.*, “Search for majorana neutrinos with the first two years of exo-200 data,” *Nature*, vol. 510, no. 7504, pp. 229–234, 2014.
- [80] J. Albert, G. Anton, I. Arnquist, I. Badhrees, P. Barbeau, D. Beck, V. Belov, F. Bourque, J. Brodsky, E. Brown, *et al.*, “Sensitivity and discovery potential of the proposed nexo experiment to neutrinoless double- $\beta$  decay,” *Physical Review C*, vol. 97, no. 6, p. 065503, 2018.
- [81] A. Gando, Y. Gando, T. Hachiya, A. Hayashi, S. Hayashida, H. Ikeda, K. Inoue, K. Ishidoshiro, Y. Karino, M. Koga, *et al.*, “Search for majorana neutrinos near the inverted mass hierarchy region with kamland-zen,” *Physical Review Letters*, vol. 117, no. 8, p. 082503, 2016.
- [82] C. Alduino, F. Alessandria, K. Alfonso, E. Andreotti, C. Arnaboldi, F. Avignone III, O. Azzolini, M. Balata, I. Bandac, T. Banks, *et al.*, “First results from cuore: A search for lepton number violation via  $0\nu\beta\beta$  decay of te-130,” *Physical review letters*, vol. 120, no. 13, p. 132501, 2018.
- [83] G. Piperno, “Dark matter search with the cuore-0 experiment,” 2015.

- [84] M. Agostini, G. Benato, and J. A. Detwiler, “Discovery probability of next-generation neutrinoless double- $\beta$  decay experiments,” *Physical Review D*, vol. 96, no. 5, p. 053001, 2017.
- [85] “Muons,” 2001 (accessed 19-July-2019). [https://cosmic.lbl.gov/SKliewer/Cosmic\\_Rays/Muons.htm](https://cosmic.lbl.gov/SKliewer/Cosmic_Rays/Muons.htm).
- [86] J. F. Beacom, S. Chen, J. Cheng, S. N. Dousttimotlagh, Y. Gao, G. Gong, H. Gong, L. Guo, R. Han, H.-J. He, *et al.*, “Physics prospects of the jinping neutrino experiment,” *Chinese physics C*, vol. 41, no. 2, p. 023002, 2017.
- [87] J. Waterfield, *Optical calibration system for SNO+ and sensitivity to neutrinoless double-beta decay*. PhD thesis, University of Sussex, 2017.
- [88] M. Stringer, *Sensitivity of SNO+ to supernova neutrinos*. PhD thesis, University of Sussex, 2019.
- [89] S. Andringa, E. Arushanova, S. Asahi, M. Askins, D. Auty, A. Back, Z. Barnard, N. Barros, E. Beier, A. Bialek, *et al.*, “Current status and future prospects of the sno+,” *Advances in High Energy Physics*, vol. 2016, 2016.
- [90] M. Anderson, S. Andringa, E. Arushanova, S. Asahi, M. Askins, D. Auty, A. Back, Z. Barnard, N. Barros, D. Bartlett, *et al.*, “Search for invisible modes of nucleon decay in water with the SNO+ detector,” *Physical Review D*, vol. 99, no. 3, p. 032008, 2019.
- [91] M. Anderson, S. Andringa, S. Asahi, M. Askins, D. Auty, N. Barros, D. Bartlett, F. Barão, R. Bayes, E. Beier, *et al.*, “Measurement of the  $^8\text{B}$  solar neutrino flux in SNO+ with very low backgrounds,” *Physical Review D*, vol. 99, no. 1, p. 012012, 2019.
- [92] M. Anderson, S. Andringa, M. Askins, D. Auty, N. Barros, F. Barão, R. Bayes, E. Beier, A. Bialek, S. Biller, *et al.*, “Measurement of neutron-proton capture in the sno+ water phase,” *Physical Review C*, vol. 102, no. 1, p. 014002, 2020.

- [93] S. Davini, M. Agostini, S. Appel, G. Bellini, J. Benziger, D. Bick, G. Bonfini, D. Bravo, B. Caccianiga, F. Calaprice, *et al.*, “CNO and pep solar neutrino measurements and perspectives in borexino,” vol. 675, no. 1, p. 012040, 2016.
- [94] D. G. Cerdeno, J. H. Davis, M. Fairbairn, and A. C. Vincent, “Cno neutrino grand prix: The race to solve the solar metallicity problem,” *Journal of Cosmology and Astroparticle Physics*, vol. 2018, no. 04, p. 037, 2018.
- [95] J. Paton, “Neutrinoless Double Beta Decay in the SNO+ Experiment,” 2019.
- [96] J. D. Jackson, *Classical Electrodynamics*. John Wiley & Sons, 2007.
- [97] L. D. Landau, J. Bell, M. Kearsley, L. Pitaevskii, E. Lifshitz, and J. Sykes, *Electrodynamics of Continuous Media*, vol. 8. elsevier, 2013.
- [98] H. W. C. Tseung and N. Tolich, “Ellipsometric measurements of the refractive indices of linear alkylbenzene and ej-301 scintillators from 210 to 1000 nm,” *Physica Scripta*, vol. 84, no. 3, p. 035701, 2011.
- [99] W. R. Leo, *Techniques for Nuclear and Particle Physics Experiments: a How-to Approach*. Springer Science & Business Media, 2012.
- [100] B. Von Krosigk, *Measurement of Proton and  $\alpha$  Particle Quenching in LAB Based Scintillators and Determination of Spectral Sensitivities to Supernova Neutrinos in the SNO+ Detector*. PhD thesis, Technische Universitaet Dresden, 2015.
- [101] A. Sørensen, *Temperature quenching in LAB based liquid scintillator and muon-induced backgrounds in the SNO+ experiment*. PhD thesis, Technische Universitaet Dresden, 2016.
- [102] J. Dunger, *Topological and time based event classification for neutrinoless double beta decay in liquid scintillator*. PhD thesis, University of Oxford, 2018.
- [103] D. A. McQuarrie and J. D. Simon, *Physical chemistry: a molecular approach*, vol. 1. University science books Sausalito, CA, 1997.

- [104] S. Collaboration, “Development and characterisation of a linear alkylbenzene-based scintillator for the SNO+ experiment (draft),” *Not submitted yet*.
- [105] J. B. Birks, “Scintillations from organic crystals: specific fluorescence and relative response to different radiations,” *Proceedings of the Physical Society. Section A*, vol. 64, no. 10, p. 874, 1951.
- [106] PerkinElmer, “Liquid scintillation cocktails,” 1998-2021 (accessed 20-Dec-2019). <https://www.perkinelmer.com/en-ca/lab-products-and-services/application-support-knowledgebase/radiometric/liquid-scintillation-cocktails.html>.
- [107] Wikipedia, “Linear alkylbenzene,” 2020 (accessed 1-Jan-2020). [https://en.wikipedia.org/wiki/Linear\\_alkylbenzene](https://en.wikipedia.org/wiki/Linear_alkylbenzene).
- [108] M. C. Helen O’Keeffe, Valentina Lozza, “Lab backgrounds expected numbers,” *SNO+ Internal Document, docDB-507-v42*.
- [109] S. W. Wunderly and J. M. Kauffman, “New quench-resistant fluors for liquid scintillation counting,” *International Journal of Radiation Applications and Instrumentation. Part A. Applied Radiation and Isotopes*, vol. 41, no. 9, pp. 809–815, 1990.
- [110] Y. Xing-Chen, Y. Bo-Xiang, Z. Xiang, Z. Li, D. Ya-Yun, L. Meng-Chao, D. Xue-Feng, Z. Xuan, J. Quan-Lin, Z. Li, *et al.*, “Preliminary study of light yield dependence on lab liquid scintillator composition,” *Chinese Physics C*, vol. 39, no. 9, p. 096003, 2015.
- [111] T. Kaptanoglu, “Measurements of light yield and timing of 0.5 g/l lab+ppo,” *SNO+ Internal Document, docDB-5997-v1*.
- [112] J.-S. Wang, “Bipo analysis using partial fill data,” *SNO+ Internal Document, docDB-5950-v3*.
- [113] J. Boger, R. Hahn, J. Rowley, A. Carter, B. Hollebone, D. Kessler, I. Blevis, F. Dalnoki-Veress, A. DeKok, J. Farine, *et al.*, “The sudbury neutrino observatory,”

*Nuclear Instruments and Methods in Physics Research Section A: Accelerators, Spectrometers, Detectors and Associated Equipment*, vol. 449, no. 1-2, pp. 172–207, 2000.

- [114] K. Hamamatsu Photonics, “Photomultiplier tubes: Basics and applications, 2007,” 2018.
- [115] R. Bonventre, *Neutron multiplicity in atmospheric neutrino events at the Sudbury Neutrino Observatory*. PhD thesis, University of Pennsylvania, 2014.
- [116] “Triggering options for sno+ water fill,” *SNO+ Internal Document, docDB-4323-v1*.
- [117] “Sno+ detector operator manual,” *SNO+ Internal Document*.
- [118] G. O. Gann, “Dealing with time in rat,” *SNO+ Internal Document, docDB-480-v1*.
- [119] J. M. Walker, *Study of Invisible Mode Nucleon Decay in the SNO+ Detector*. PhD thesis, University of Liverpool, 2016.
- [120] M. R. Dragowsky, *Sudbury Neutrino Observatory energy calibration using gamma-ray sources*. PhD thesis, Oregon State University, 1999.
- [121] A. S. Hamer, *Energy calibration of SNO for measurement of the charged-current neutrino reaction*. PhD thesis, Queen’s University, 2001.
- [122] National Nuclear Data Center, 2019 (accessed Oct 30, 2019). <https://www.nndc.bnl.gov/>.
- [123] *RAT Overview*, 2020 (accessed Mar 15, 2020). <https://rat.readthedocs.io/en/latest/overview.html>.
- [124] “Overview - rat 1.0 documentation,” 2014 (accessed 20-Dec-2019). <https://rat.readthedocs.io/en/latest/overview.html#goals>.
- [125] M. Anderson, “Status and updates on neural network fitter,” *SNO+ Internal Document, docDB-6298-v1*.

- [126] M. Anderson, “Deep learning to reconstruct particle interaction properties for the SNO+ neutrino physics experiment,” *Canadian AI Conference 2020 - Talk*.
- [127] P. Gregory, *Bayesian Logical Data Analysis for the Physical Sciences: A Comparative Approach with Mathematica® Support*. Cambridge University Press, 2005.
- [128] F. Barao and J. Maneira, “Group velocity measurement, plot for approval,” *SNO+ Internal Document, docDB-5071-v1*.
- [129] I. T. Coulter, *Modelling and Reconstruction of Events in SNO+ related to Future Searches for Lepton and Baryon Number Violation*. PhD thesis, University of Oxford, 2013.
- [130] Wikipedia, *JSON*, 2020 (accessed Mar 15, 2020). <https://en.wikipedia.org/wiki/JSON>.
- [131] ROOT, *TDecompQRH Class Reference*, 2020 (accessed Mar 15, 2020). <https://root.cern.ch/doc/master/classTDecompQRH.html>.
- [132] W. P. Group, “Water physics unidoc,” *SNO+ Internal Document*.
- [133] X. Dai, E. Rollin, A. Bellerive, C. Hargrove, D. Sinclair, C. Mifflin, and F. Zhang, “Wavelength shifters for water cherenkov detectors,” *Nuclear Instruments and Methods in Physics Research Section A: Accelerators, Spectrometers, Detectors and Associated Equipment*, vol. 589, no. 2, pp. 290–295, 2008.
- [134] J. Alonso, N. Barros, M. Bergevin, A. Bernstein, L. Bignell, E. Blucher, F. Calaprice, J. Conrad, F. Descamps, M. Diwan, *et al.*, “Advanced scintillator detector concept (asdc): a concept paper on the physics potential of water-based liquid scintillator,” *arXiv preprint arXiv:1409.5864*, 2014.
- [135] M. Askins, M. Bergevin, A. Bernstein, S. Dazeley, S. Dye, T. Handler, A. Hatzikoutelis, D. Hellfeld, P. Jaffke, Y. Kamyshkov, *et al.*, “The physics and nuclear non-

- proliferation goals of watchman: A water cherenkov monitor for antineutrinos,” *arXiv preprint arXiv:1502.01132*, 2015.
- [136] M. G. Boulay, *Direct Evidence for Weak Flavour Mixing with the Sudbury Neutrino Observatory*. PhD thesis, Queens University, 2004.
- [137] P. Mekarski, *Electron Antineutrinos in the Water Phase of the SNO+ Experiment*. PhD thesis, University of Alberta, 2018.
- [138] S. D. Biller, E. J. Leming, and J. L. Paton, “Slow fluors for highly effective separation of cherenkov light in liquid scintillators,” *arXiv preprint arXiv:2001.10825*, 2020.
- [139] A. LaTorre, “New measurements for the timing spectrum of electrons and alphas in lab+ppo,” *SNO+ Internal Document, docDB-4081-v1*.
- [140] L. Lebanowski, “Improved mode cut,” *SNO+ Internal Document, docDB-5488-v1*.
- [141] B. A. Moffat, *The optical calibration of the Sudbury Neutrino Observatory*. PhD thesis, Queens University, 2001.
- [142] M. Mottram, “Note on RSP fitter,” *SNO+ Internal Document, docDB-3939-v1*.
- [143] M. Mottram, “Energy reconstruction in partial scintillator fill,” *SNO+ Internal Document, docDB-3133-v1*.
- [144] Y. Zhang, “Performance of qenergy based on q,” *SNO+ Internal Document, docDB-6065-v1*.
- [145] E. Davies, “Machine vision: Theory, algorithms, practicalities. academic press., 2-nd edition,” 1997.
- [146] Wikipedia, *Hough Transform*, 2019 (accessed Nov 3, 2019). [https://en.wikipedia.org/wiki/Hough\\_transform](https://en.wikipedia.org/wiki/Hough_transform).
- [147] M. Shiozawa, “Reconstruction algorithms in the super-kamiokande large water cherenkov detector,” *Nuclear Instruments and Methods in Physics Research Section*

- A: Accelerators, Spectrometers, Detectors and Associated Equipment*, vol. 433, no. 1-2, pp. 240–246, 1999.
- [148] G. Beier, “Study of direction reconstruction in scintillator,” *SNO+ Internal Document, docDB-3503-v4*.
- [149] J. Klein, “Leta high level cuts (including qpdt and itr),” *SNO+ Internal Document, docDB-2512-v1*.
- [150] TMVA, 2020 (accessed Mar 30, 2020). <https://root.cern.ch/tmva>.
- [151] K. Albertsson, S. Gleyzer, A. Hoecker, L. Moneta, P. Speckmayer, J. Stelzer, J. Therhaag, E. von Toerne, H. Voss, and S. Wunsch, “Tmva 4,” *arXiv preprint physics/0703039*, 2007.
- [152] *StatPatternRecognition and Machine Learning in HEP*, 2020 (accessed Mar 30, 2020). <http://www.hep.caltech.edu/~narsky/spr.html>.
- [153] S. Biller, S. Manecki, S. collaboration, *et al.*, “A new technique to load 130te in liquid scintillator for neutrinoless double beta decay experiments,” in *Journal of Physics: Conference Series*, vol. 888, p. 012084, IOP Publishing, 2017.
- [154] J. Bramante, B. Broerman, J. Kumar, R. F. Lang, M. Pospelov, and N. Raj, “Foraging for dark matter in large volume liquid scintillator neutrino detectors with multiscatter events,” *Physical Review D*, vol. 99, no. 8, p. 083010, 2019.
- [155] H. H. Chen, “Direct approach to resolve the solar-neutrino problem,” *Physical Review Letters*, vol. 55, no. 14, p. 1534, 1985.
- [156] Q. R. Ahmad, R. Allen, T. Andersen, J. Anglin, J. Barton, E. Beier, M. Bercovitch, J. Bigu, S. Biller, R. Black, *et al.*, “Direct evidence for neutrino flavor transformation from neutral-current interactions in the sudbury neutrino observatory,” *Physical review letters*, vol. 89, no. 1, p. 011301, 2002.

- [157] B. Aharmim, S. Ahmed, A. Anthony, N. Barros, E. Beier, A. Bellerive, B. Beltran, M. Bergevin, S. Biller, K. Boudjemline, *et al.*, “Combined analysis of all three phases of solar neutrino data from the sudbury neutrino observatory,” *Physical Review C*, vol. 88, no. 2, p. 025501, 2013.
- [158] H. W. Zaglauer and K. H. Schwarzer, “The mixing angles in matter for three generations of neutrinos and the msw mechanism,” *Zeitschrift für Physik C Particles and Fields*, vol. 40, no. 2, pp. 273–282, 1988.
- [159] P. B. Denton, S. J. Parke, and X. Zhang, “Eigenvalues: The rosetta stone for neutrino oscillations in matter,” *arXiv preprint arXiv:1907.02534*, 2019.
- [160] J. Schechter and J. W. Valle, “Neutrinoless double- $\beta$  decay in  $\text{su}(2) \times \text{u}(1)$  theories,” *Physical Review D*, vol. 25, no. 11, p. 2951, 1982.
- [161] M. Duerr, M. Lindner, and A. Merle, “On the quantitative impact of the schechter-valle theorem,” *Journal of High Energy Physics*, vol. 2011, no. 6, p. 91, 2011.
- [162] E. Takasugi, “Can the neutrinoless double beta decay take place in the case of dirac neutrinos?,” *Physics Letters B*, vol. 149, no. 4-5, pp. 372–376, 1984.
- [163] M. Agostini, M. Allardt, A. Bakalyarov, M. Balata, I. Barabanov, L. Baudis, C. Bauer, E. Bellotti, S. Belogurov, S. Belyaev, *et al.*, “Background-free search for neutrinoless double- $\beta$  decay of  $^{76}\text{ge}$  with gerda,” *Nature*, vol. 544, no. 7648, pp. 47–52, 2017.
- [164] M. Spurio, Spurio, and Bellantone, *Probes of Multimessenger Astrophysics*. Springer, 2018.
- [165] D. H. Perkins, *Particle astrophysics*. No. 10, Oxford University Press, 2009.
- [166] G. Kane, *Modern elementary particle physics: explaining and extending the standard model*. Cambridge University Press, 2017.
- [167] I. Esteban, M. Gonzalez-Garcia, A. Hernandez-Cabezudo, M. Maltoni, and T. Schwetz, “Global analysis of three-flavour neutrino oscillations: synergies and ten-

- sions in the determination of  $\theta_{23}$ ,  $\delta_{CP}$ , and the mass ordering,” *Journal of High Energy Physics*, vol. 2019, no. 1, p. 106, 2019.
- [168] C. Weinheimer, “Neutrino mass from triton decay,” *Progress in Particle and Nuclear Physics*, vol. 57, no. 1, pp. 22–37, 2006.
- [169] A. Bialek, M. Chen, B. Cleveland, P. Gorel, A. Hallin, P. Harvey, J. Heise, C. Kraus, C. Krauss, I. Lawson, *et al.*, “A rope-net support system for the liquid scintillator detector for the sno+ experiment,” *Nuclear Instruments and Methods in Physics Research Section A: Accelerators, Spectrometers, Detectors and Associated Equipment*, vol. 827, pp. 152–160, 2016.
- [170] A. M. Richie Bonventre, “Everything a detector operator ever wanted to know about electronics and much more you didnt want to know.”
- [171] T. Kaptanoglu, “Characterization of the hamamatsu 8 r5912-mod photomultiplier tube,” *Nuclear Instruments and Methods in Physics Research Section A: Accelerators, Spectrometers, Detectors and Associated Equipment*, vol. 889, pp. 69–77, 2018.
- [172] M. Anderson, “Neural network fitter updates,” *SNO+ Internal Document, docDB-6298-v1*.
- [173] R. Brun, F. Rademakers, P. Canal, *et al.*, “Root: An object oriented data analysis framework, 2007,” *See Also <http://root.cern.ch>.*
- [174] S. Agostinelli, J. Allison, K. a. Amako, J. Apostolakis, H. Araujo, P. Arce, M. Asai, D. Axen, S. Banerjee, G. . Barrand, *et al.*, “Geant4a simulation toolkit,” *Nuclear instruments and methods in physics research section A: Accelerators, Spectrometers, Detectors and Associated Equipment*, vol. 506, no. 3, pp. 250–303, 2003.
- [175] G. Horton-Smith *et al.*, “Introduction to glg4sim,” 2006.
- [176] M. Dunford, *Measurement of the  $^8B$  solar neutrino energy spectrum at the Sudbury Neutrino Observatory*. PhD thesis, University of Pennsylvania, 2006.